Title: Designed sensors reveal normal and oncogenic Ras signaling in endomembranes and condensates

Jason Z. Zhang[1-3,7], William H. Nguyen[1], John C. Rose[4], Shao-En Ong[5], Dustin J. Maly[1,6,8], David Baker[1-3,8]

[1]Department of Biochemistry, University of Washington, Seattle, Washington 98195, United States

[2]Institute for Protein Design, University of Washington, Seattle, Washington 98195, United States

[3]Howard Hughes Medical Institute, University of Washington, Seattle, Washington 98195, United States

[4]Department of Dermatology, Stanford University School of Medicine, Stanford, California 94305, United States

[5]Department of Pharmacology, University of Washington, Seattle, Washington 98195, United States

[6]Department of Chemistry, University of Washington, Seattle, Washington 98195, United States

[7]Lead contact

[8]These authors contributed equally

Abstract:

While the ability of Ras to dynamically shuttle around the cell is well characterized, the activity, mechanism of activation, and function of non-plasma membrane-localized Ras is less well understood due to lack of suitable tools. Here, we describe the use of the Latching Orthogonal Cage-Key pRotein (LOCKR) switch platform to generate first-in-class intracellular sensors of endogenous Ras activity (Ras-LOCKR-S) and signaling environment (Ras-LOCKR-PL). By targeting these tools to endomembranes and oncogenic condensates, we defined subcellular Ras activity and identified upstream Ras effectors (guanine exchange factors and SAM68) responsible for signaling in these locations. We also found that Major Vault Protein drives Ras^{G12C} inhibitor resistance by enhancing wild type Ras-mediated signaling at the golgi and mutant Ras signaling at mitochondria. Together, these results highlight the importance of non-plasma membrane Ras signaling (endomembranes and condensates), and our new sensors should accelerate the discovery of new therapeutic targets.

Introduction:

The signaling enzyme Ras (Rat sarcoma virus) regulates many key cellular processes. Balancing its activity is critical for normal cell function as the Ras protein family is one of the most frequently mutated in cancers (Cox and Der, 2010). Ras GTPases have intrinsic GTP hydrolysis activity and switch between GDP-bound (inactive) and GTP-bound (active, typically increased in cancer). Biochemical regulation of Ras is mediated through guanine exchange factors (GEFs) such as Son of Sevenless (Sos), which activate Ras by swapping GDP with GTP, while GTPase activating proteins (GAPs) inactivate Ras by promoting GTP hydrolysis. Spatiotemporal organization of Ras and its associated

Mitogen-Activated Protein Kinase (MAPK) pathway (Raf/Mek/Erk) components is required for homeostasis. Post-translational modifications of the C-terminal hypervariable regions (HVR or CAAX) of Ras mediates isoform selective membrane partitioning (Lynch et al., 2015; Schmick et al., 2015) with HRas and NRas isoforms dynamically shuttling between the plasma membrane (PM) and endomembranes such as the endoplasmic reticulum (ER), golgi, and mitochondria (Lynch et al., 2015; Rocks et al., 2005).

Ras activity is well understood at the PM, but Ras signaling and function at endomembranes is less clear (Augsten et al., 2006; Bivona et al., 2006; Chiu et al., 2002) and the contributions of endomembrane-localized Ras towards oncogenesis and drug resistance are unknown (Ryan et al., 2020). Furthermore, while it is generally thought that Ras requires membranes for activation, granules formed by oncoprotein fusions containing receptor tyrosine kinases (RTK) such as EML4-Alk lead to membrane-independent cytosolic Ras activity (Tulpule et al., 2021). Deciphering the sources, mechanisms, and roles of these distinct Ras signaling microdomains is important to understand how this central signaling node encodes functional specificity and could shed light on how cancer cells hijack this Ras signaling organization (Muñoz-Maldonado et al., 2019; Posch et al., 2016; Santra et al., 2019; Tulpule et al., 2021). Addressing these open questions requires perturbators and sensors that modulate and detect physiologically relevant Ras activity. For example, the Chemically Inducible Activator of Ras (CIAR) (Mohan et al., 2019; Rose et al., 2017a) enables direct activation of endogenous Ras at specific subcellular locations. There are currently no sensors that allow real-time, sub-cellular sensing of endogenous Ras activity or environment despite decades of effort.

To understand the spatiotemporal regulation of Ras signaling, new tools are needed that 1) sense the activity and environment of Ras, 2) are sensitive enough to detect endogenous levels of active Ras, 3) can be used for live-cell imaging, 4) specifically report events within subcellular regions, 5) and have single cell resolution. We set out to develop Ras sensors with these properties and reasoned that the *de novo* designed LOCKR switch proteins (Langan et al., 2019, Quijano-Rubio et al., 2021) would be well suited to sense active Ras with a variety of readouts such as fluorescence and proximity labeling (**Figure S1A**). The LOCKR system switches based on target binding and has 2 protein components: 1) “Cage” protein composed of a “cage” and “latch” domain, the latter of which has affinity for the cage and contains a target-binding domain and a readout domain (e.g. fluorescent protein (FP)), 2) “Key” protein that also has affinity to cage and contains another readout domain. Without target, the switch protein is closed with latch bound to cage, thus hiding the readout domain. Target binding onto latch shifts the equilibrium such that key preferentially binds to cage and allows the 2 readout portions to interact (Langan et al., 2019; Ng et al., 2019), resulting in detectable changes (**Figure 1A**).

Results:

Design of LOCKR-based Ras activity sensors.

We sought to design an intracellular Ras activity sensor that avoids the need for Ras overexpression and allows for subcellular localization (**Figure 1A**). Previous LOCKR

sensors have been based on reconstitution of split luciferase, which is not optimal for subcellular reporting. For readout, ratiometric Förster Resonance Energy Transfer (FRET) emission, which is dependent on the distance between a fluorescent protein (FP) pair, is a powerful modality for intracellular activity reporters (Greenwald et al., 2018). To test if LOCKR is amenable to FRET readouts, which can be localized with much higher resolution than luminescence, we converted the readout of a LOCKR-based sensor for the receptor binding domain (RBD) of SARS-CoV-2 (Quijano-Rubio et al., 2021; Zhang et al., 2022a) to FRET by placing CFP or YFP at the termini of Key or Cage (**Figure S1A-F**). Regardless of the FP placement, RBD addition increased FRET emission ratios YFP/CFP (Y/C) by up to 40% (**Figure S1E**).

Capturing the range of endogenous Ras activities is difficult as the concentration change in active Ras (Ras-GTP) after upstream activation is nanomolar (Li et al., 2020), and hence sensors must be sensitive and quantitative. We adapted the LOCKR scaffold to sense endogenous Ras-GTP levels (Ras activity, LOCKR-based Sensor: Ras-LOCKR-S) by grafting the Ras binding domain from Raf (RasBD) in the LOCKR latch. In our Ras-LOCKR-S designs, the embedded RasBD interacts with the cage domain in the closed state (**Figure 1A, left)**, and binding of Ras-GTP to RasBD shifts the equilibrium from the closed state with latch bound to cage and FPs apart, to the open state (**Figure 1A, right**) allowing the key to bind to the cage and bringing the two FPs in close proximity for FRET. In generating Ras-LOCKR-S candidates (all Ras-LOCKR-S candidates are listed in **Table S1**), several aspects of the LOCKR switch were tuned to improve Ras-GTP-dependent changes in emission ratio (**Figure 1A and S1A**): placement of FPs and the RasBD, lengths of linkers between FPs and Cage/Key, and interaction strength between latch:cage or key:cage.

To test whether the Ras-LOCKR-S designs are capable of reporting endogenous Ras temporal dynamics, we activated endogenous Ras either through Epidermal growth factor (EGF) activation of its receptor (EGFR) (induces rapid and transient Ras activity) or A115-induced activation of a CIAR switch localized to the PM (CIAR-PM) (Mohan et al., 2019; Rose et al., 2017a) (induces direct and sustained Ras activity). For our first set of designs, we used the Rosetta-based GraftSwitchMover (Langan et al., 2019) program to graft the RasBD onto the C-terminal section of latch at different registers (placements differ by a couple of amino acids) (**Figure S1G**). The highest dynamic range candidate from RasBD placement testing was further optimized by ensuring roughly equimolar expression (**Figure S1H**) and using structure prediction models to identify mutations that alter LOCKR switchability (see Methods). Mutating hydrophobic residues that contribute to latch:cage and key:cage interaction to serines (**Figure S1I-J**) led to Ras-LOCKR-S_P2A2_L3K2 (3 mutations in latch and 2 mutations in key), which showed consistent emission ratio increases (~10%) upon stimulation (**Figure S1I**); this is the Ras-LOCKR-S construct used throughout the rest of the paper.

We characterized Ras activity dynamics using the untargeted version of Ras-LOCKR-S and observed transient emission ratio changes from EGF stimulation but sustained emission ratio changes after treating CIAR-PM-expressing cells with A115 (**Figure 1B**), reflecting previously observed dynamics of downstream active Erk levels (Rose et al.,

2017a). Under the same conditions, there were no observed changes in emission ratios for a Ras-LOCKR-S construct (Ras-LOCKR-S NC) that contains a mutation ($RasBD^{R89L}$) that abrogates Ras-GTP binding (Tran et al., 2021). Consistent with Ras-LOCKR-S demonstrating specificity for Ras-GTP, we observed that co-expression of a dominant negative mutant of Ras ($HRas^{S17N}$) eliminated emission ratio changes after EGF stimulation or A115 activation of CIAR-PM (**Figure 1C and S1K**) and emission ratios were unaffected by co-expression of a GAP for Rap (structurally similar to Ras) in response to EGF stimulation (**Figure S1L-M**). Thus, Ras-LOCKR-S enables readout of endogenous Ras activity at a single cell resolution with minute-to-minute dynamics.

Identification of cell-type specific differences in endomembrane Ras activity using Ras-LOCKR-S

To map out the endogenous Ras signaling landscape at a subcellular resolution, we generated Ras-LOCKR-S that are localized to the golgi, ER, PM lipid raft regions (PM LR), or PM non lipid raft regions (PM nonLR) using localization tags (**Figure 2A and S2A-E**). Subcellularly-targeted Ras-LOCKR-S primarily reported local Ras signaling as CIAR constructs localized to PM, ER, or golgi (**Figure 2A and S2F-J**) induced selective and rapid emission ratio increases from Ras-LOCKR-S localized to the same area in response to A115 treatment (**Figure 2B and S2H**). Despite localization to PM (**Figure S5D**), CIAR-PM induced Ras signaling also at ER and golgi (**Figure 2B and S2K**), suggesting that active Ras shuttles from PM to endomembranes. Ras activation through CIAR-PM also led to downstream Erk activity (Keyes et al., 2020) at PM and golgi, but not in the ER – where Ras activation may be too limited, suggesting a possible filtering mechanism in translating Ras activation to Erk signaling (**Figure S2K**). Further supporting this notion, in CIAR-PM cells treated with a range of A115 concentrations, PM LR and golgi-localized Ras-LOCKR-S showed lower 50% activation (AC50) values than EKAR4 localized to the same areas (**Figure S2L**). Thus, localized Ras-LOCKR-S can detect subcellular Ras activation levels and provide insight into subcellular Ras signaling networks.

Whether endogenous Ras signaling (such as from receptor tyrosine activation) occurs at endomembranes is still under debate (Augsten et al., 2006; Bivona et al., 2006; Chiu et al., 2002). To address this controversy, we employed our subcellularly-targeted Ras-LOCKR-S to examine the spatiotemporal dynamics of endogenous Ras signaling resulting from physiological stimulation such as EGF stimulation of EGFR. In 293T cells expressing PM, ER, or golgi-localized Ras-LOCKR-S, EGF induced emission ratio increases in all subcellular regions tested (**Figure 2C**), demonstrating that RTK stimulation can indeed lead to endogenous Ras signaling at endomembranes.

Compared to 293T cells, Ras in Jukat T-cells is highly enriched at the golgi (**Figure S3A**), and this pool of Ras is activated during T-cell receptor (TCR) stimulation when NRas is ectopically overexpressed (Quatela et al., 2006) but the endogenous Ras activity landscape during TCR activation is unknown. We found that Ras-LOCKR-S can also report endogenous Ras signaling in response to localized CIAR activation in Jurkat T-cells (**Figure 2D and S3B-F**) and that TCR-activated Jurkats displayed emission ratio increases for the golgi and PM LR (but not PM nonLR)-localized Ras-LOCKR-S (**Figure**

2E and S3G). In contrast to CIAR-golgi in 293T cells (**Figure S2H**), activation of CIAR-golgi in Jurkats led to sustained golgi-Ras activity **(Figure S3F)**, showcasing cell-to-cell differences in the subcellular Ras signaling landscape. Furthermore, golgi-localized Ras activation in Jurkats appears to be functionally relevant as activation of CIAR-golgi led to levels of increased CD69 surface expression, IL-2 secretion, and cell growth that are comparable to Ras activation at the PM and low level stimulation of the TCR (**Figure 2F and S3H-I**).

Taken together, these results demonstrate that EGFR and TCR activation leads to endogenous Ras signaling at endomembranes and that endomembrane Ras signaling is functionally relevant in TCR signaling.

Design of LOCKR-based Ras activity-dependent proximity labelers.

To enable identification of upstream Ras activators and downstream effectors in different celular compartments, we developed a LOCKR-based system that carries out proximity labeling in response to Ras-GTP (Ras-activity dependent, LOCKR-based proximity labeler: Ras-LOCKR-PL) (**Figure 3A and Table S2**) by replacing the FPs in LOCKR-S with split biotin ligases. Binding of Ras-GTP to RasBD shifts the relative affinities between the LOCKR components to promote key binding to cage, leading to assembly of a functional proximity labeler (**Figure 3A**). We tested split versions of the biotin ligases ContactID (Kwak et al., 2020) and TurboID (Cho et al., 2020) using the lucCageRBD as the starting point and measured biotinylation of cellular proteins induced by RBD expression. In 293T cells, the split ContactID-contaning Ras-LOCKR-PL (**Figure S4A-B**) showed no increase in biotinylation with RBD expression, while the split TurboID-contaning Ras-LOCKR-PL (**Figure S4C-D**) showed RBD-induced biotinylation. As Ras-LOCKR-PL activation is modulated by the residual affinity between the two halves of split TurboID (unlike Ras-LOCKR-S where the FPs have no basal interaction affinity), different RasBD register placements were again tested. SwitchGraftMover identified possible RasBD placements on latch and these candidates were tested for selective labeling in CIAR-PM-expressing 293T cells treated with A115 (**Figure S4E-F**). We found that the placement of RasBD in the Ras-LOCKR-PL construct with the highest dynamic range was offset by five amino acids relative to the RBD within Ras-LOCKR-S. Guided by structure prediction models, the latch and key were mutated or truncated to weaken cage interactions in the hopes of maximizing the dynamic range in A115-inducible biotinylation (**Figure S4G-H**). Mutating the key consistently decreased background biotinylation, leading to an overall increased dynamic range (**Figure S4H**). The highest dynamic range Ras-LOCKR-PL candidates were then tested at shorter biotinylation times (1 and 3 hrs) (**Figure S4I**) and the design that showed the highest and most selective labeling of Ras (**Figure S4J**) was selected, which we refer to as Ras-LOCKR-PL for the remainder of the paper.

Co-expression of Ras-LOCKR-PL with constitutively active Ras ($HRas^{G12V}$) or the catalytic domain of Sos (Sos_{cat}) led to increased levels of biotinylation, while co-expression of dominant negative Ras ($HRas^{S17N}$) or the RasGAP Gap1m blunted biotinylation in CIAR-PM-expressing 293Ts treated with A115 (**Figure S4K**). Deletion of

the RasBD in Ras-LOCKR-PL eliminated A115-induced biotinylation in CIAR-PM-expressing 293Ts (**Figure 3B**). Ras-LOCKR-PL was Ras specific: co-expression of a RapGEF CalDAG-GEFI to increase Rap-GTP levels did not affect A115-induced biotinylation (**Figure S4K**). We sought to subcellularly target Ras-LOCKR-PL using the same localization sequences as Ras-LOCKR-S (**Figure 3C and S4L-M**) and observed that each construct colocalized with the expected subcellular marker by immunofluorescence. Visualizing the patterns of biotinylation by localized Ras-LOCKR-PLs in response to A115 treatment of CIAR-PM-expresssing 293Ts showed these were localized as expected in fixed cells (**Figure 3D**). Mass spectrometry analysis showed that subcellularly localized Ras-LOCKR-PL biotinylated local components including known Ras effectors and MAPK pathway interactors (**Table S3**). Overall, Ras-LOCKR-PL is a first-in-class Ras signaling-dependent proximity labeler that accurately profiles subcellular signalosomes.

Sos1 is required for maintaining Ras activity at the golgi.

Following up on our observation of Ras signaling at endomembranes, we used subcellularly targetable Ras-LOCKR-PL to understand the mechanisms by which endogenous Ras is activated at these regions. Sos1 RasGEF, which is best characterized for its role in PM-localized Ras activity in response to RTK activation (Christensen et al., 2016), surprisingly showed a significant increase in labeling using golgi-localized Ras-LOCKR-PL when Ras was activated at the PM with CIAR-PM (**Figure 4A**). We investigated possible SOs localization in the Golgi by tagging with mCherry. mCherry-tagged Sos1 colocalized with golgi-localized GFP in 293T cells, and golgi-proximal Sos1 was present both before and after EGF stimulation (**Figure 4B**). Immunostaining of endogenous Sos1 and giantin as a golgi marker (Satoh et al., 2019) showed similar patterns (**Figure S5A-D**). Golgi-proximal Sos1 was consistently observed across multiple cell lines and with different Sos1 antibodies (**Figure S5B-C**), and was dependent on Sos1 lipid binding domains but independent of EGFR stimulation (**Figure S5E-F**).

To probe whether the golgi pool of Sos1 is required for golgi Ras signaling, we targeted Ras-LOCKR-S and the Ras^{S17N} dominant negative mutant which sequesters Sos1 and other RasGEFs (Cox and Der, 2010) to the golgi in CIAR 293T stable lines. Both EGF and activation of CIAR-PM elicited golgi-Ras signaling that was abrogated by golgi-localized Ras^{S17N} (**Figure 4C and S5G**), suggesting that golgi-localized Sos1 is necessary for golgi-Ras signaling. Golgi-localized Ras^{S17N} specifically inhibits local Ras activity as golgi-Ras^{S17N} did not affect EGF or CIAR-PM-elicited PM-Ras signaling (**Figure 4D and S5H**). With the same stimulation, PM-localized Ras^{S17N} also eliminated golgi-Ras signaling (**Figure 4C and S5G**), suggesting shuttling of activated Ras from the PM to the golgi. In contrast, PM-localized Ras activity is solely dependent on PM-localized Ras activation and RasGEFs (**Figure S5I-J**).

Golgi-localized Sos1 GEF activity is necessary for Ras activity at the golgi (**Figure 4C**), but why does distal PM-Ras stimulation (CIAR-PM) lead to more golgi-Ras activity than local golgi-Ras activation (CIAR-golgi) (**Figure 2B**)? The golgi pool of Ras is influenced by the PM pool (**Figure 4C**) and we wondered if PM-localized Ras-GTP influences

(possibly by trafficking (**Figure 2B and S2K**)) the allosteric site of golgi-localized Sos, which increases nucleotide exchange ~50-fold when Ras-GTP binds there (Christensen et al., 2016). To manipulate Sos1, we used Sos1 knockout (KO) A549 cells. During EGFR stimulation, rescue with WT Sos1 led to golgi-Ras activity whereas expression of Sos1 mutant (W729E) that eliminates allosteric site binding led to no EGF-induced golgi-Ras activity (**Figure S5K**) but does not affect EGF-elicited PM-Ras activity (**Figure S5L**), suggesting the Ras-GTP allosteric site of Sos plays an important role in permissing Ras signaling at the golgi. Altogether, these results suggest that Sos1 at the golgi is necessary to maintain golgi-Ras signaling possibly by the following model: Ras activated at PM relays down to golgi to bind to the allosteric site of golgi-localized Sos1, which *in situ* loads GTP onto local Ras (**Figure 4E**). Thus, this model answers why PM-Ras stimulation leads to substantial golgi-Ras signaling as there is a large pool of Ras-GTP trafficked from PM (**Figure S3A**) that can activate golgi-localized Sos1 through Sos1's allosteric site. Moreover, these biological findings showcase the utility of these Ras tools to reveal mechanistic insights into Ras signaling.

Designed tools identify components inside Ras-active EML4-Alk granules that drive aberrant cytosolic Ras signaling.

In addition to membranes, Ras signaling can also occur in membrane-less oncogenic condensates such as EML4-Alk granules which are found in 2-9% of non-small-cell lung cancers (Sampson et al., 2021; Tulpule et al., 2021). EML4-Alk variant 1 (v1) and variant 3 (v3), which represent the majority of observed oncogenic domain truncations, form cytosolic granules that can recruit upstream effectors of Ras via the Alk kinase domain (Sampson et al., 2021; Tulpule et al., 2021), resulting in elevated Ras signaling inside this microdomain. Ras activity inside the granules was measured by fusing Ras-LOCKR-S to EML4-Alk in Beas2B WT lung cells, which still allowed granule formation and displayed increased raw emission ratios compared to those in the diffuse regions (**Figure S6A-B**), consistent with previous reports showing increased Ras activity in these granules (Tulpule et al., 2021). In contrast, Ras-LOCKR-S NC showed no difference in raw emission ratios between punctate and diffuse regions. Ras-LOCKR-S recruited to EML4-Alk mutants that do not form granules (∆ Trimerization Domain (TD)) (Sampson et al., 2021; Tulpule et al., 2021) showed lower raw emission ratios compared to EML4-Alk WT puncta (**Figure S6A-B**). These experiments demonstrate the ability of Ras-LOCKR-S to measure signaling in a variety of subcellular microdomains.

Several Ras effectors have been identified to be inside EML4-Alk granules (Tulpule et al., 2021), but an unbiased investigation of the components inside EML4-ALk condensates has not been performed. To do this, we applied Ras-LOCKR-PL to these condensates (**Figure 5A and S6C-E**). Direct fusion caused EML4-Alk to lose granule formation (**Figure S6C**), but targeting a Ras-LOCKR-PL Key-GFP nanobody (GFPnb) fusion to EML4-Alk-YFP enabled granule formation (**Figure 5A and S6D-E**). Consistent with increased Ras signaling inside EML4-Alk granules, Ras-LOCKR-PL recruitment to granules resulted in more biotinylation inside versus outside the granules as seen in streptavidin

immunostaining (**Figure 5A and S6E**). Using the same GFPnb targeting strategy, this increased biotinylation inside granules was not observed when full length TurboID is targeted to EML4-Alk (**Figure 5A and S6E**).

To determine the proteins in proximity to Ras-GTP inside the EML4-Alk granules, we quantified labeled proteins in Beas2B cells containing EML4-Alk + GFPnb-Ras-LOCKR-PL versus GFPnb-Ras-LOCKR-PL alone (**Figure S6D-I and Table S4**). Labeling of tubulin is enhanced in cells expressing EML4-Alk, which is expected as EML4 binds to microtubules (Sampson et al., 2021). Several additional proteins previously shown to be enriched (blue arrows in **Figure S6I**) inside the EML4-Alk granules (Tulpule et al., 2021) were also identified, such as known Ras effectors like Grb2, demonstrating that Ras-LOCKR-PL can label components involved in Ras signaling. We also compared the composition of v1 versus v3 granules (**Figure S6F**), and observed that a regulator for Rho GTPase (RhoGDI) and the 14-3-3 protein YWHAG were more enriched in v1 versus v3 granules (**Figure S7A**). These components were indeed enriched in v1 granules as seen in immunostaining (**Figure S7A**) and lost their binding to the ΔTD mutant of EML4-Alk (**Figure S7B**). Thus, these proximity labeling tools can identify Ras signaling components inside these oncogenic granules.

We further probed two hits associated with cancers (Bielli et al., 2011; Iyer et al., 2021) (**Figure 5B, S6I, and S7A-C**): Src-Associated in Mitosis 68 kDa protein (SAM68/KHDRBS1) (Najib et al., 2005) and Myristoylated Alanine Rich Protein Kinase C Substrate (MARCKS) (Li et al., 2001). We explored if inhibition of these targets prevented aberrant cytosolic Ras signaling and co-inhibition of Alk improved killing of EML4-Alk v1 and v3-containing lung adenocarcinoma cells H3122 and H2228, respectively. MARCKS or SAM68 inhibition (**Figure S7D-E**) alone decreased Ras signaling inside puncta using condensate-localized Ras-LOCKR-S (**Figure 5C and S7F**). Co-inhibition of MARCKS/SAM68 and Alk led to several changes specific to EML4-Alk-addicted cells but not WT Beas2B cells: 1) leftward IC50 shifts (compared to Alk inhibitor alone) for pErk and pStat3 levels (**Figure S7G-I**), 2) leftward IC50 shifts (compared to Alk inhibitor alone) for cell growth (**Figure S7J**), 3) and decreased colony formation (**Figure S7K**). Both MARCKS and SAM68 inhibition disrupted their enrichment in granules but did not dissolve the granules themselves (**Figure 5B and S7A**), suggesting that MARCKS and SAM68 play a signaling role upstream of Ras in EML4-Alk-mediated oncogenic signaling but not in granule formation. Overall, our designed Ras tools enabled the discovery of key components inside Ras-active EML4-Alk granules that drive proliferation and targeting of these components may be therapeutically beneficial (**Figure 5D**).

Major Vault Protein (MVP) scaffolds MAPK pathway components to drive oncogenic golgi-localized Ras signaling during Ras^{G12C} inhibitor resistance.

Recently developed covalent inhibitors against GDP-bound Ras^{G12C} (Sotorasib/ AMG-510) (Lanman et al., 2019; Ostrem et al., 2013) have demonstrated promising efficacy, however ~50% of patients acquire drug resistance (Awad et al., 2021). How this resistance against Ras^{G12C} inhibitors achieved (**Figure 6A**) is an important outstanding

question. Our designed Ras tools are well positioned to uncover the mechanisms of this heterogeneous adaptive signaling (Xue et al., 2020) due to their ability to sense active Ras at single cell resolution. Ras-LOCKR-S was introduced into two Ras G12C-driven cancer cell lines with different kinetics of rebound signaling upon AMG-510 addition: H358 with rapid and MIA PaCa-2 with slow rebound Erk signaling (**Figure 6B**). Using subcellularly targeted Ras-LOCKR-S expressed in these two cell lines, we tracked subcellular Ras activity over 72 hrs upon AMG-510 addition (**Figure 6C and S8A**). H358 cells conferred heterogeneous responses with resurgent but overall reduced Ras activity at PM, large increases in Ras activity at golgi, and no statistically significant changes in Ras signaling at ER, demonstrating that drug resistant Ras signaling in cancer cells can emanate from endomembranes.

The emergence of golgi-localized Ras signaling in rebound-prone H358 cells after AMG-510 treatment made us wonder whether this compartment functionally contributed to drug resistance. We expressed dominant negative Ras (Ras^{S17N}) at different subcellular regions and observed sustained decreases in pErk levels and Ras activity (**Figure S8B-C**). Furthermore, golgi-localized Ras^{S17N} expression with AMG-510 treatment abrogated H358 and MIA PaCa-2 cell growth (**Figure 6D and S8D**), suggesting that Ras signaling at the golgi fuels growth in Ras^{G12C}-driven cancer cells.

To investigate what is responsible for this shift in the spatial organization of Ras signaling from AMG-510 treatment, we used subcellularly targeted Ras-LOCKR-PL. Golgi-localized Ras-LOCKR-PL after 24 hr drug treatment labeled more protein species (**Figure S8E-F**), consistent with Ras-LOCKR-S data demonstrating golgi-Ras activity increases after drug treatment (**Figure 6C and S8A**). We compared the enrichment values of labeled proteins between 4 and 24 hr AMG-510 treatment (**Figure 6E, S8E-G, and Table S5**) as hits more enriched after 24 hr treatment represent proteins that contribute to the adaptive signaling against AMG-510 according to pErk immunoblots (**Figure 6B**). The top enriched proteins following AMG-510 treatment in rebound-prone H358 cells (labeled "Difference" in **Figure 6E**), PAPOLG, MVP, and VDAC1, were verified for their in cell biotinylation via proximity ligation assay (PLA) in both H358 and MIA PaCa-2 cells. The PLA data matched well with the mass spectrometry data (**Figure 6E and S8G-H**). However, siRNA knockdown (KD) of the PAPOLG and VDAC1 did not eliminate AMG-510-induced golgi-Ras activity increases (**Figure S8I**), so these hits were not pursued further. In contrast, MVP KD led to complete abrogation of AMG-510-induced adaptive Ras signaling at the golgi in H358 cells (**Figure 6F and S8J-L**). Both golgi-Ras-LOCKR-PL-mediated biotinylation (indicative of presence in golgi-Ras signalosome) of MVP and golgi-Ras-LOCKR-S responses to drug (**Figure 6G-H and S8L**) varied from cell to cell. This labeling heterogeneity likely reflects the strength of golgi-Ras signaling as evidenced by the positive correlation between golgi-localized Ras activity and golgi-Ras-LOCKR-PL-mediated MVP biotinylation in both $KRas^{G12C}$ cells (R^2=0.66) (**Figure 6H**), suggesting that MVP enrichment in the golgi-localized Ras signalosome (possibly due to MVP shifting to golgi (**Figure S8M**)) is involved in local Ras activity. Functionally, MVP KD with AMG-510 treatment prevented cell growth in both cell lines (**Figure S8N**), with even less cell growth than co-treatment with a previously identified molecule (SHP099) that prevents Ras^{G12C}

inhibitor-resistant tumors (Ryan et al., 2020). Thus, these results reveal MVP as an upstream driver for golgi-localized Ras activity to enable Ras^{G12C} inhibitor resistance.

MVP expression increases during drug resistance and regulates several signaling branches downstream of Ras by interacting with Shp2 and Erk, nuclearly sequestering negative regulators of PI3K/Akt signaling and thus activating Akt, and promoting RTK-mediated MAPK signaling (Berger et al., 2009). We thus investigated MVP's scaffolding activities after AMG-510 treatment by probing its interaction with Shp2, Erk, and RTKs EGFR and fibroblast growth factor receptor (FGFR3) via PLA (**Figure S9A-C**). In both $KRas^{G12C}$ lines, AMG-510 treatment for 24 hrs increased MVP interactions with all of the aforementioned MAPK pathway components. Per cell, the number of MVP interactions positively correlated with pErk levels (R^2=0.86) (**Figure S9C**). Moreover, MVP KD in both $KRas^{G12C}$ lines decreased Shp2:Erk and Shp2:EGFR interactions and the amount of Shp2 interactions positively correlated with golgi-localized Ras activity (R^2=0.826) (**Figure 6I and S9D-E**). These results suggest MVP scaffolds MAPK signaling components to drive MAPK signaling.

While the subcellular distribution of Ras activities from Ras^{G12C} inhibition has functional implications, whether this re-distribution is due to WT Ras or from drug-resistant Ras^{G12C} is not clear (Xue et al., 2020). We observed that MVP interactions with WT HRas and NRas increased while interactions with mutant KRas decreased upon AMG-510 treatment (**Figure S9F-I**), suggesting that WT Ras in conjunction with MVP plays a compensatory signaling role after $KRas^{G12C}$ inhibition. Furthermore, these interactome changes for MVP correlate well with the golgi-Ras-LOCKR-S emission ratio (KRas: negative correlation presumably due to low golgi localization of KRas, R^2=0.85; HRas: positive correlation, R^2=0.76; NRas: positive correlation, R^2=0.779) (**Figure S9H**). To test whether Ras WT plays a role in re-distributed Ras signaling during Ras^{G12C} inhibition, rebound-prone H358 cells transfected with localized Ras-LOCKR-S were treated with AMG-510 over 72 hr and then subsequently treated for 2 hr with an inhibitor which targets GTP-bound Ras^{G12C} (RasON) (**Figure S9J**). RasON treatment significantly decreased PM-Ras-LOCKR-S raw emission ratio but not the golgi-localized sensor, indicating that WT Ras is the major contributor for adaptive signaling at the golgi and GTP-bound Ras^{G12C} plays a role for PM-localized rebound signaling.

Immunoblotting revealed that MVP levels rapidly (~4-24 hrs) increased in both $KRas^{G12C}$ lines treated with AMG-510 (**Figure S9K**). MVP KD led to decreased Shp2 phosphorylation (a marker of Shp2 activation), eliminated rebound pErk signaling, and overall decreased pAkt levels (**Figure S9K**). Overall, these data identify the MVP scaffold as a master regulator in driving drug resistant Ras signaling at the golgi.

MVP scaffolding fuels adaptive mitochondrial Ras activity and shifts to pro-Warburg metabolism during Ras^{G12C} inhibitor resistance.

Ras^{G12C} inhibition leads to initial (24 hr) downregulation but then reactivation (72 hr) of glycolysis (Santana-Codina et al., 2020), consistent with the "Warburg effect" where cancer cells typically increase glycolytic flux (Camara et al., 2017). Several glycolysis-

regulating mitochondrial proteins such as voltage-dependent anion channels (VDAC) showed increased labeling by golgi-Ras-LOCKR-PL after AMG-510 treatment (**Figure 6E**), possibly due to regions where golgi and mitochondria are in proximity (**Figure S10A**). VDACs regulate cytosolic/mitochondrial levels of ATP to affect glycolysis rates and interacts with the first enzyme in the glycolysis pathway, hexokinase, which binds to and is activated by GTP-loaded KRas4A (Amendola et al., 2019). Following up on the observation that KRas associates with MVP (**Figure S9F-I**), we probed the connection between MVP and VDAC and found using PLA that both $KRas^{G12C}$ lines displayed increased MVP:VDAC interactions after AMG-510 addition (**Figure 7A**), possibly due to AMG-510-dependent increases in MVP localization at mitochondria (**Figure S10B**). In $KRas^{G12C}$ lines expressing the cytosolic ATP sensor Cyto-PercevalHR (Tantama et al., 2013; Werley et al., 2020), MVP:VDAC interactions correlated with decreased cytosolic ATP levels (R^2=0.81) (**Figure S10C**), and low cytosolic ATP/ADP ratios relieves inhibition of glycolysis pathway enzymes thus leading to increased glycolytic flux (Heslop et al., 2021). We further found that MVP KD decreased Ras:VDAC interactions and reduced cytosolic ATP levels (R^2=0.787) (**Figure 7B and S10D**). These data suggest that metabolic changes during Ras^{G12C} inhibitor resistance may be due in part to MVP regulating the Ras interactome at the mitochondria.

With the changes in Ras, MVP, and VDAC interactions during AMG-510 treatment, we examined the adaptations of Ras activity at the mitochondria by localizing Ras-LOCKR-S to this region (Mito-Ras-LOCKR-S) (**Figure S10E-F**). We observed that AMG-510 treatment initially slightly decreased but then significantly increased Mito-Ras-LOCKR-S response over 72 hrs while the control Ras-LOCKR-S NC showed no emission ratio changes (**Figure 7C and S10G**). In parallel, AMG-510 treatment over 72 hrs decreased cytosolic ATP levels in both $KRas^{G12C}$ lines expressing cyto-PercevalHR (**Figure 7D and S10H**). MVP KD abolished the emergence of mitochondrial Ras activity (**Figure 7C and S10G**) and eliminated AMG-510-induced cytosolic ATP changes (**Figure 7D and S10H**), possibly through MVP modulating hexokinase through KRas4A. Co-treatment of AMG-510 with erastin, a small molecule VDAC activator that increases cytosolic ATP and thus lowers glycolysis, eliminated cell growth in both $KRas^{G12C}$ lines (**Figure S10I**), suggesting that manipulating VDAC function can prevent $KRas^{G12C}$ inhibitor resistance.

To test if these adaptive signaling and metabolic changes at the mitochondria are due to WT or mutant Ras, H358 cells were transfected with mito-Ras-LOCKR-S or Cyto-PercevalHR and their response to AMG-510 over 72 hrs and then subsequent 2 hr RasON treatment were monitored. RasON addition decreased mitochondrial Ras activity and increased cytosolic ATP levels (**Figure S10J-K**), suggesting that Ras^{G12C} plays a role in these rewired signaling and metabolic changes at the mitochondria (Xue et al., 2020).

Overall, our results suggest that in response to Ras^{G12C} inhibitors, cancer cells express and relocalize MVP, which scaffolds MAPK pathway components. MVP-mediated adaptations drive Ras activation at endomembranes (golgi and mitochondria), which increases downstream signaling and enables “pro-Warburg” metabolism (**Figure 7E**).

Discussion:

Despite decades of intensive study, it is still unclear how Ras signaling is organized to maintain functional specificity. Ras at the plasma membrane has a key functional role, but it is not currently clear whether Ras is active at other compartments such as endomembranes, and if so, how it is activated at these different compartments. The roles of different Ras microdomains in signaling, cellular, and pathological roles are also unclear. Answering these long-standing questions requires tools to measure, track, and perturb endogenous Ras signaling with spatiotemporal and single cell resolution, but current sensors lack these capabilities. Current live-cell imaging sensors tether GFP to RasBD, which can measure only overexpressed Ras activity dynamics and cannot measure compartment-specific signaling (Augsten et al., 2006; Bivona et al., 2003; Chiu et al., 2002). The FRET-based Ras-Raichu sensor, can only measure GEF and GAP activity and also inherently overexpresses Ras (Komatsu et al., 2011; Mochizuki et al., 2001). There are also no tools available to profile the components in the Ras signalosome.

Here we describe critically needed sensors, proximity labelers, and perturbators based on the de novo designed LOCKR switch. Due to the generalizability and orthogonality to the signaling pathway of the LOCKR system, these LOCKR-based activity sensors and proximity labelers are well suited for characterizing the subcellular landscape of not only signaling molecules but more broadly any state-dependent process such as post-translational modified molecules and protein conformational changes. The activity-dependent proximity labeler reveals distinct subcellular “signalosomes”, which mediate functional specificity of central molecules. Application of Ras-LOCKR-PL to EML4-Alk condensates highlights this tool’s potential in understanding the filtering mechanisms for signaling condensates. Overall, these results illustrate the power of the LOCKR platform for intracellular mapping of the activities, mechanisms, and functions for state-dependent molecules such as Ras, knowledge of which is broadly useful for understanding homeostatic and diseased states.

Deployment of our tools demonstrated that endogenous Ras signals not only at the PM but also at endomembranes (golgi and mitochondria) and in cytosolic condensates. Beyond detection, our tools identified local components that mediate compartment-specific Ras signaling, and provide insight into the mechanisms of oncogenesis by revealing the upstream players contributing to pathogenic signaling, which are potential drug targets as their perturbation can broadly interfere with the multiple downstream pathways. We envision new co-treatment regimens to tackle and prevent drug resistance in EML4-Alk-driven lung cancer (Alk inhibitors in conjunction with SAM68 and/or MARCKS inhibitors). We also uncovered key mechanisms mediating resistance to Ras^{G12C} inhibitors through rewired endomembrane-localized signaling and metabolism due to MVP-mediated reshuffling of Ras signaling to the golgi and mitochondria. Though the mechanistic understanding of MVP and MAPK-mediated regulation at the mitochondria is not fully understood, previous evidence shows that Erk phosphorylation of VDAC regulates its function (Galli et al., 2009; Uozumi et al., 2015), possibly providing a mechanistic link. Moreover, as Erk and Akt regulate metabolism, the Erk/Akt signaling changes during AMG-510-resistance (**Figure S9K**) may provide another mechanistic link between MVP-MAPK crosstalk at the mitochondria to rewire metabolism. Many cases of

drug resistance are associated with increased MVP expression (including Ras^{G12C} inhibitors (Santana-Codina et al., 2020)). Our results reveal that Ras-driven cancers exploit MVP to adaptively bypass Ras^{G12C} inhibitors and this MVP-mediated mechanism may be generally involved in resistance to new inhibitors against other Ras mutants (Zhang et al., 2022b; Zhang et al., 2022c) and perhaps other cancer drugs.

Taken together, our work maps the landscape of Ras signaling at subcellular resolution using the *de novo* protein switch LOCKR as a general scaffold for probing Ras signaling. Application of these Ras-LOCKR tools reveals non-plasma membrane regions as critical in organizing Ras activity, disruption of which can contribute to cancer. By profiling the activities and components inside oncogenic Ras signalosomes, we discovered new therapeutic targets. These results also illustrate how spatiotemporal mapping using designed sensors can contribute to understanding of the functions of central, pleiotropic biomolecules such as Ras. As the development of new technologies goes hand-in-hand with biological discovery, designed tools to spatiotemporally map the intricate organization of biochemical activity networks during homeostatic and diseased states should continue to contribute to scientific advances.

STAR Methods:

KEY RESOURCES TABLE

REAGENT or RESOURCE	SOURCE	IDENTIFIER
Antibodies		
Ms anti-Erk	CST	9107
Rb anti-phospho-Erk	CST	9101
Ms anti-Akt	CST	2920
Rb anti-phospho-Akt (S473)	CST	9271
Ms anti-Stat3	CST	9139
Rb anti-phospho-Stat3	CST	9145
Ms anti-Alk	CST	3791
Rb anti-phospho-Alk	CST	3341
Rb anti-GAPDH	CST	5174
Ms anti-Vinculin	Sigma-Aldrich	V9131
Ms anti-Myc Tag	CST	2276
Ms anti-Flag Tag	Sigma-Aldrich	A8592

Rb anti-V5 Tag	CST	13202
Ms anti-V5 Tag	CST	80076
Rb anti-CD69	Abcam	ab233396
Ms anti-CD3ε	Ancell	144-020
Ms anti-CD28	Ancell	177-020
Rb anti-E cadherin	Abcam	ab40772
Rb anti-Sec61B	Abcam	ab15576
Ms anti-Giantin	Abcam	ab37266
Rb anti-Bcl-xl	CST	2764
Ms anti-Bcl-xl	Abcam	ab77571
Rb anti-pan Ras	CST	91054
Rb anti-HA Tag	CST	3724
Rb anti-GFP	CST	2555
Rb anti-Sos1	Thermo Fisher	PA5-117671
Rb anti-Sos1	Abcam	ab140621
Rb anti-Sos1	Novus	NBP2-94657
Rb anti-RhoGDI	CST	2564
Ms anti-SAM68	Santa Cruz Biotechnology	sc-514468
Rb anti-SAM68	CST	33210
Rb anti-YWHAG	Abcam	ab155050
Rb anti-MARCKS	CST	5607
Ms anti-Grb2	Abcam	ab281846
Rb anti-Grb2	Abcam	ab32037
Rb anti-PAPOLG	Thermo Fisher	PA5-41901
Rb anti-MVP	Novus	NBP1-33560
Ms anti-MVP	Fisher Scientific	MS664P1ABX
Rb anti-VDAC1	Abcam	ab15895
Rb anti-pan VDAC	Alomone Labs	AVC-001
Rb anti-Stat1	CST	9172S

Rb anti-phospho-Stat1 (Y701)	CST	9167S
Rb anti-Shp2	CST	3397S
Rb anti-Shp2 (Y542)	Abcam	ab62322
Ms anti-EGFR	Abcam	ab30
Rb anti-FGFR3	CST	4574S
Gt anti-Biotin	Vector Labs	SP-3000-1
Rb anti-Biotin	Abcam	ab53494
Ms anti-Biotin	Abcam	ab201341
Rb anti-KRas	Abcam	ab275876
Ms anti-HRas	Abcam	ab86696
Rb anti-NRas	Thermo Fisher	PA5-28861
Rb anti-Hsp60	CST	12165S
Ms anti-Hsp60	Abcam	ab59457
Duolink® In Situ PLA® Probe Anti-Goat PLUS	Millipore Sigma	DUO92003
Duolink® In Situ PLA® Probe Anti-Goat MINUS	Millipore Sigma	DUO92006
Duolink® In Situ PLA® Probe Anti-Rabbit PLUS	Millipore Sigma	DUO92002
Duolink® In Situ PLA® Probe Anti-Rabbit MINUS	Millipore Sigma	DUO92005
Duolink® In Situ PLA® Probe Anti-Mouse PLUS	Millipore Sigma	DUO92001
Duolink® In Situ PLA® Probe Anti-Mouse MINUS	Millipore Sigma	DUO92004
680 RD anti-Ms	LICOR	26-68071

680 RD anti-Rb	LICOR	926-68070
800 CW anti-Ms	LICOR	926-32210
800 CW anti-Rb	LICOR	926-32211
AF488 anti-Ms	Thermo Fisher	A11029
AF568 anti-Rb	Thermo Fisher	A11036
AF488 anti-Rb	Thermo Fisher	A11034
AF750 anti-Ms	Thermo Fisher	A21037
Bacterial and Virus Strains		
Lemo21(DE3)	NEB	C2528J
Chemicals, Peptides, and Recombinant Proteins		
Forskolin	Calbiochem	34427
A-1155463	Chemietek	CT-A115
AMG-510	Selleck Chem	S8830
Fugene HD Transfection Reagent	Fugene	E2311
Crystal Violet Stain	Sigma-Aldrich	C0775
Ceritinib	Selleck Chem	S7083
Crizotinib	Sigma-Aldrich	PZ0191
Gö6983	Tocris	2285
BIO-11006 Acetate	MedChem Express	HY-106377A
YB-0158	GLP Bio	GC63303
Poly-D-Lysine	MP Biomedical	0215017580
Neutravidin-DyLight 650	Thermo Fisher	84607
RIPA Buffer	Thermo Fisher	89901

Pierce™ High Capacity Streptavidin Agarose	Thermo Fisher	20359
Lipofectamine™ LTX Reagent with PLUS™ Reagent	Thermo Fisher	15338100
Turbofectin 8.0	Origene	TF81001
Electroporation Buffer	MaxCyte	EPB-5
16% PFA	Electron Microscopy Services	15710
Trans-Blot Turbo Transfer Pack	BioRad	1704159
Pierce Protease Inhibitor Tablets	Thermo Fisher	A32963
PHEM 0.2M	Electron Microscopy Services	11165
Biotin	Sigma-Aldrich	B4501
0.25% Trypsin-EDTA	Gibco	25200072
Pageruler Prestained Ladder	Thermo Fisher	PI26620
Spectra™ Multicolor High Range Protein Ladder	Thermo Fisher	26625
Protein A Agarose Beads	CST	9863S
Protein G Agarose Beads	CST	37478
Puromycin	Tocris	4089
Hygromycin	Tocris	4137
DPBS	Gibco	14190250
Doxycycline	Tocris	4090

PEI Max	PolyScience	24765
Studier Induction Media	Teknova	3S8000
Kanamycin	Millipore Sigma	PHR1487
Ni-NTA resin	Qiagen	30250
Ultra-15 Centrifugal Filter Units	Amicon	UFC9100
Superdex 75 Increase 10/300 GL	GE Healthcare	29148721
EGF	Thermo Fisher	PHG0311
Expi293 expression media	Gibco	A1435101
Polydiallyldimethylammonium	Sigma-Aldrich	409014
Talon cobalt affinity resin	Takara Bio	635653
Cytiva S200 Increase column	Sigma-Aldrich	GE28-9909-44
DAPI	ThermoFisher	62248
LysC	ThermoFisher	90051
Trypsin	Promega	V5111
DFHBI-1T	Sigma-Aldrich	SML2697
FluoroBrite DMEM Media	GIBCO	A1896701
FBS	Sigma-Aldrich	F2442
Pen-Strep	Sigma-Aldrich	P4333
RPMI 1640	GIBCO	11875093
EpiLife Media	GIBCO	MEPI500CA
Keratinocyte Growth Supplement	GIBCO	S0015

IMDM	GIBCO	31980097
SHP099	Selleck Chem	S8278
MitoTracker™ Red CMXRos	Thermo Fisher	M7512
Erastin	Selleck Chem	S7242
Duolink® In Situ Wash Buffers, Fluorescence	Sigma Aldrich	DUO82049
Lipofectamine™ RNAiMAX Transfection Reagent	Thermo Fisher	13778075
Critical Commercial Assays		
Electroporation Cartridge	MaxCyte	SOC-25
Any kD SDS-PAGE gels	BioRad	5671125
IL-2 ELISA Kit	Thermo Fisher	BMS221-2
Duolink® In Situ Detection Reagents Red	Millipore Sigma	DUO92008
Duolink® In Situ Detection Reagents FarRed	Millipore Sigma	DUO92013
Duolink® In Situ Detection Reagents Orange	Millipore Sigma	DUO92007
Ras ON G12C Inhibitor (RAS/ RAS-RAF-IN-1)	Med Chem Express	HY-138294
Experimental Models: Cell Lines		
HEK293T	ATCC	CRL-3216
HEK293F	ATCC	CRL-1573
HEK293-FlpIn TRex	Invitrogen	R78007
HeLa	ATCC	CCL-2
MIA PaCa-2	ATCC	CRL-1420
H358	ATCC	CRL-5807
A459 Sos1 KO	Abcam	ab286377

H6C7	Kerafast	ECA001-FP
SK-MEL-2	ATCC	HTB-68
HepG2	ATCC	HB-8065
WM3406	Rockland	WM3406-01-0001
Beas2B	ATCC	CRL-9609
Jurkat	ATCC	TIB-152
H3122	Gift from R. Bayliss lab	
H2228	Gift from R. Bayliss lab	
HEKn	ATCC	PCS-200-010
Capan-1	ATCC	HTB-79
Oligonucleotides		
ON-TARGETplus Non-targeting Control Pool	Horizon	D-001810-10-05
ON-TARGETplus Human MVP siRNA	Horizon	L-004984-01-0010
ON-TARGETplus Human PAPOLG siRNA	Horizon	L-009854-01-0005
ON-TARGETplus Human VDAC1 siRNA	Horizon	L-019764-00-0005
ON-TARGETplus Human Stat1 siRNA	Horizon	L-003543-00-0005
Recombinant DNA		
Rap1A FLARE	O'Shaughnessy et al J Cell Biol. 2019	Addgene plasmid #134926
Rap1B FLARE	O'Shaughnessy et	Addgene plasmid #134927

	al J Cell Biol. 2019	
pcDNA3 EKAR4	Keyes et al Elife. 2020	Addgene plasmid #174437
pMOS007 Cyto-PercevalHR	Werley et al Nat Commun. 2020	Addgene plasmid #163061
Remaining plasmids	This paper	See Tables 1 and 2
Software and Algorithms		
GraftSwitchMover	Baker lab	http://files.ipd.uw.edu/pub/de_novo_design_of_tunable_biosensors_2021/designcode_and_models.zip

RESOURCE AVAILABILITY

Lead contact

Further information and requests for resources and reagents should be directed to and will be fulfilled by the lead contact, Jason Zhang (Jason.zhang0428@gmail.com).

Materials Availability

Plasmids generated in this study will be made available through Addgene and can be shared upon request.

Data and code availability

The data that support the findings of this study are available from the corresponding author upon reasonable request. All accession codes have been provided for the paper. Source data are provided with this paper including mass spectrometry analysis. No additional code was generated for this study. Source data are provided with this paper.

Computational grafting of sensing domains onto latch domain

The first 7-11 amino acids from the RasBD of CRaf was grafted using Rosettascripts GraftSwitchMover into all α-helical registers between residues 325 and 359 of the latch domain within the Cage protein. The resulting Cages were energy-minimized using Rosetta fast relax, visually inspected and typically less than ten designs were selected for subsequent cellular characterization.

EXPERIMENTAL MODEL AND SUBJECT DETAILS

Cell culture and transfection

HEK293T, HEK293F, HEK293-FlpIn TRex, HeLa, MIA PaCa-2, H358, A549 Sos1 KO cells, H6C7, SK-MEL-2, HepG2, and WM3406 were cultured in Dulbecco's modified Eagle medium (DMEM) containing 1 g L^{-1} glucose and supplemented with 10% (v/v) fetal bovine serum (FBS) and 1% (v/v) penicillin–streptomycin (Pen-Strep). Beas2B, Jurkat, H3122, H2228 were cultured in Roswell Park Memorial Institute 1640 (RPMI 1640) with 10% (v/v) FBS and 1% Pen-Strep. HEKn cells were cultured in EpiLife media with 1% (v/v) Human Keratinocyte Growth Supplement (HKGS). Capan-1 cells were cultured in Isocove Modified Dulbecco's Media (IMDM) supplemented with 20% (v/v) FBS. All cells were grown in a humidified incubator at 5% CO_2 and at 37°C.

Before transfection, all cells were plated onto sterile poly-D-lysine coated plates or dishes and grown to 50%–70% confluence. HEK293T and Beas2B cells were transfected using Turbofectin 8, HEK293F cells were transfected with PEI-MAX, Jurkat cells were transfected with Lipofectamine LTX only for Ras-LOCKR-S experiments, siRNA transfection used Lipofectamine RNAiMAX, and all other cells/conditions were transfected with Fugene HD and grown for an additional 16-24 hr before imaging. All cells underwent serum starvation for 16 hr unless indicated. Transfecting CIAR in Jurkat cells involved electroporation using the MaxCyte system transfecting at a 1:1 ratio a pcDNA5 recombinase plasmid and an attb-containing plasmid that encodes for localized CIAR, puromycin resistance gene, and IRES-driven GFP. A negative control plate was also grown that was not transfected with the attb-containing plasmid. If electroporation led to ~25% of cells to be GFP+, cells were subjected to 1 μg mL^{-1} puromycin selection for at least 2 days until there was 95% cell death in the negative control plate. Then, Jurkat cells were regrown for 2 days and CIAR expression was induced with 500ng mL^{-1} doxycycline overnight.

Generation of stable cell lines

Generating localized RasS17N in H358 and MIA-PaCa2 cells and CIAR stable cell lines in HEK293T FlpIn TRex cells involved Turbofectin 8 transfection of a pcDNA5 recombinase plasmid and an attb-containing plasmid at a 1:1 ratio that encodes for localized CIAR and puromycin resistance gene. A negative control plate was also grown that was not transfected with the attb-containing plasmid. After cells were 10-25% confluent (usually 48 hr later), 100 ng mL^{-1} of hygromycin was added until 95% cell death in the negative control plate. Recover cells without hygromycin until cells are 80% confluent. Afterwards, recombined stable cell lines were maintained in 1 μg mL^{-1} puromycin.

METHOD DETAILS

Plasmid construction

All plasmids constructed here are using the pcDNA 3.1 backbone (unless otherwise indicated) and were produced by GenScript.

General procedures for bacterial protein production and purification.

Except for purification of RBD, the *E. coli* Lemo21(DE3) strain was transformed with a pET29b$^+$ plasmid encoding the synthesized gene of interest. Cells were grown for 24 hr in liquid broth medium supplemented with kanamycin. Cells were inoculated at a 1:50 ml ratio in the Studier TBM-5052 autoinduction medium supplemented with kanamycin, grown at 37°C for 2–4 hr and then grown at 18°C for an additional 18 hr. Cells were collected by centrifugation at 4,000 *g* at 4 °C for 15 min and resuspended in 30 ml lysis buffer (20 mM Tris-HCl, pH 8.0, 300 mM NaCl, 30 mM imidazole, 1 mM PMSF and 0.02 mg ml^{-1} DNase). Cell resuspensions were lysed by sonication for 2.5 min (5 s cycles). Lysates were clarified by centrifugation at 24,000 *g* at 4°C for 20 min and passed through 2-ml Ni-NTA nickel resin pre-equilibrated with wash buffer (20 mM Tris-HCl, pH 8.0, 300 mM NaCl and 30 mM imidazole). The resin was washed twice with 10 column volumes (Cversus) of wash buffer, and then eluted with 3 Cversus elution buffer (20 mM Tris-HCl, pH 8.0, 300 mM NaCl and 300 mM imidazole). The eluted proteins were concentrated using Ultra-15 Centrifugal Filter Units and further purified by using a Superdex 75 Increase 10/300 GL size exclusion column in TBS (25 mM Tris-HCl, pH 8.0, and 150 mM NaCl). Fractions containing monomeric protein were pooled, concentrated and snap-frozen in liquid nitrogen and stored at −80°C.

Procedure to purify RBD from mammalian cells.

RBD proteins were produced in Expi293F cells grown in suspension using Expi293F expression medium at 33 °C, 70% humidity, 8% CO_2 rotating at 150 rpm. The cultures were transfected using PEI-MAX with cells grown to a density of 3x10^6 cells mL^{-1} and cultivated for 3 days. Supernatants were clarified by centrifugation (5min at 4,000 *g*), addition of polydiallyldimethylammonium chloride solution to a final concentration of 0.0375% and a second spin (5min at 4,000g).

His-tagged RBD was purified from clarified supernatants via a batch bind method, where each clarified supernatant was supplemented with 1 M Tris-HCl, pH 8.0, to a final concentration of 45 mM and 5 M NaCl to a final concentration of 310 mM. Talon cobalt affinity resin was added to the treated supernatants and allowed to incubate for 15 min with gentle shaking. Resin was collected using vacuum filtration with a 0.2-mm filter and transferred to a gravity column. The resin was washed with 20 mM Tris, pH 8.0, 300 mM NaCl, and the protein was eluted with 3 Cversus of 20 mM Tris, pH 8.0, 300 mM NaCl and 300 mM imidazole. The batch bind process was then repeated and the first and second elutions combined. SDS-PAGE was used to assess purity. Following immobilized metal affinity chromatography purification, the elution was concentrated and applied to a Cytiva S200 Increase column equilibrated with 20 mM Tris 150 mM NaCl, pH 8.0, and the peak of interest was collected and quantified using A280.

Cell counting to measure cell proliferation

Jurkat, Beas2B, H3122, H2228, H358, and MIA PaCa-2 cell lines were seeded in 6-wells plates at 10,000 cells/well. Cell numbers were quantified using a hemacytometer each day for 7 days.

Colony formation assay

Beas2B, H3122, and H2228 cell lines were seeded in 24-well plates at 100 cells/well. All at room temperature, cells were washed once with PBS, fixed with 4% paraformaldehyde (PFA) in PBS for 10 min, stained with 2.5 mg/mL crystal violet stain dissolved in 20% methanol for 10 min, and then washed 6x with PBS. Images were captured using the ZOE Fluorescent Cell Imager (BioRad).

Immunostaining and flow cytometry

293T, CIAR-PM, HeLa, Jurkat, and Beas2B cell lines were seeded onto 24-well glass-bottom plates. After transfection and drug addition, cells were fixed with 4% PFA in 2x PHEM buffer (60 mM PIPES, 50 mM HEPES, 20 mM EGTA, 4 mM $MgCl_2$, 0.25 M sucrose, pH 7.3) for 10 min, permeabilized with 100% methanol for 10 min (except for surface expression of CD69 in Jurkat experiments), washed with PBS 3x, blocked in 1% BSA in PBS for 30 min, incubated with primary antibody overnight at 4°C, washed with PBS 3x, incubated with DAPI, neutravidin-DyLight 650, and secondary antibody for 1 hr at room temperature and aluminum foil cover. Cells were then washed with PBS 3x and mounted for epifluorescence imaging or underwent flow cytometry analysis (Attune NxT Acoustic Focusing Cytometer, ThermoFisher). All images were collected via and analyzed in ImageJ or FlowJo.

Proximity Ligation Assay

H358 and MIA PaCa-2 cells were seeded onto 24-well glass-bottom plates. After transfection and drug addition, cells were fixed with 4% PFA in 2x PHEM buffer for 10 min, permeabilized with 100% methanol for 10 min, washed with PBS 3x, blocked in 1% BSA in PBS for 30 min, incubated with primary antibody overnight at 4°C, washed with Wash Buffer A 2x, incubated with DAPI and secondary antibody with PLUS or MINUS DNA for 1 hr at 37°C, washed with Wash Buffer A 2x, incubated in ligation buffer for 30 min at 37°C, washed with Wash Buffer A 2x, incubated in amplification buffer for 100 min at 37°C, and finally washed with Wash Buffer B 3x. Cells were then mounted for epifluorescence imaging. All images were collected via and analyzed in ImageJ.

Immunoblotting and immunoprecipitation

Cells expressing indicated constructs and incubated with indicated drugs were plated, transfected, and labeled as described in figure legends. Cells were then transferred to ice and washed 2x with ice cold DPBS. Cells were then detached from the well by addition of 1x RIPA lysis buffer (50 mM Tris pH 8, 150 mM NaCl, 0.1% SDS, 0.5% sodium deoxycholate, 1% Triton X-100, 1x protease inhibitor cocktail, 1 mM PMSF, 1mM Na_3VO_4, 1% NP-40) and either scraping of cells or rotation on shaker for 30 min at 4°C. Cells were

then collected and vortexed for at least 5 s every 10 min for 20 min at 4°C. Cells were then collected and clarified by centrifugation at 20,000 rpm for 10 minutes at 4°C. The supernatant was collected and underwent Pierce BCA assay to quantify total protein amounts.

For immunoblotting, whole cell lysate protein amounts were normalized across samples in the same gel, mixed with 4x loading buffer prior to loading, incubated at 95°C for 5 min and then 4°C for 5 min, and separated on Any kDa SDS-PAGE gels. Proteins separated on SDS-page gels were transferred to nitrocellulose membranes via the TransBlot system (BioRad). The blots were then blocked in 5% milk (w/v) in TBST (Tris-buffered saline, 0.1% Tween 20) for 1 hr at room temperature. Blots were washed with TBST 3x then incubated with indicated primary antibodies in 1% BSA (w/v) in TBST overnight at 4°C. Blots were then washed with TBST 3x and incubated with LICOR dye-conjugated secondary antibodies (LICOR 680/800 or streptavidin-LICOR 800) in 1% BSA (w/v) in TBST for 1 hr at room temperature. The blots were washed with TBST 3x and imaged on an Odyssey IR imager (LICOR). Quantitation of Western blots was performed using ImageJ on raw images.

For immunoprecipitation, agarose beads were either preloaded with streptavidin (high capacity streptavidin beads) or loaded by 3x lysis buffer washes and then addition of 1mg ml^{-1} indicated antibodies at 4°C on orbital shaker for 3 hr. Beads were washed 2x in lysis buffer. Whole cell lysate protein amounts were normalized across samples and protein samples were added to beads (at least 100μg per sample) either at room temperature for 1 hr for streptavidin beads or at 4°C on orbital shaker overnight. Beads were then washed 2x in lysis buffer and 1x in TBS and then mixed with 4x loading buffer sometimes containing 2mM biotin and 20mM DTT (Xiong et al., 2021) for streptavidin pulldowns. The remaining portion of the protocol is the same as immunoblotting.

Enzyme-linked immunosorbent assay

Jurkat cells (some electroporated with CIAR) were stimulated with 250nM A115 or indicated amounts of α-CD3ε + α-CD28 overnight. The supernatant was collected and subjected to the IL-2 ELISA assay kit according to manufacturer's protocol.

Mass spectrometry analysis

Cells expressing indicated constructs and incubated with indicated drugs were plated, transfected, and labeled as described in figure legends. Cells were then transferred to ice and washed 2x with ice cold DPBS, detached from the well by addition of 1x RIPA lysis buffer (50 mM Tris pH 8, 150 mM NaCl, 0.1% SDS, 0.5% sodium deoxycholate, 1% Triton X-100, 1x protease inhibitor cocktail, 1 mM PMSF, 1mM Na_3VO_4, 1% NP-40) and scraping of cells, collected and vortexed for at least 5 s every 10 min for 20 min at 4°C, and collected and clarified by centrifugation at 20,000g for 10 minutes at 4°C. The supernatant was collected and underwent Pierce BCA assay to quantify total protein amounts.

50μL of high capacity streptavidin agarose beads were washed 2x in lysis buffer. Whole cell lysate protein amounts were normalized across samples and protein samples were added to beads (at least 100μg per sample) at room temperature for 1 hr. Beads were then washed 2x with lysis buffer, 1x with 1M KCl, 1x with 0.1M Na_2CO_3, 2x 2M urea, and 2x with TBS. Beads were re-suspended in 50μL of denaturing buffer (6M guanidinium chloride, 50mM Tris containing 5mM TCEP and 10mM CAM with TCEP and CAM added fresh every time), inverted a few times, and heated to 95°C for 5 min. The bead slurry was diluted with 50μL of 100mM TEAB and 0.8μg of LysC was added per sample with the pH adjusted to 8-9 using 1M NaOH. This mixture was agitated on a thermomixer at 37°C for 2 hr at 1400 rpm. Afterwards, samples were diluted 2x with 100μL of 100mM TEAB with 0.8μg of sequencing grade trypsin per sample with the pH adjusted to 8-9 using 1M NaOH. This mixture was agitated on a thermomixer at 37°C for 12-14 hr at 800 rpm. After overnight trypsinization, samples were diluted 2x with 200μL of Buffer A (5% acetonitrile with 0.1% TFA) containing 1% formic acid. These samples were inverted a few times and pH adjusted to 2-3 using 100% formic acid. StageTips for peptide desalting were prepared by extracting out plugs from C18 matrices, shoved down a 200L tip, and pressed with a plunger for flatness. Using these StageTips, 50L of Buffer B (80% acetonitrile with 0.1% TFA) was passed through at 4000g for 1 min followed by 50L of Buffer A for 4000g for 1 min. The supernatant of the samples were added to StageTips and spun down at 4000g for 5 min. Then, 50L of Buffer A was added and spun down at 4000g for 2.5 min. 50L of Buffer B was added to stage tips and a syringe pump was applied to elute samples.

Peptide samples were separated on an EASY-nLC 1200 System (Thermo Fisher Scientific) using 20 cm long fused silica capillary columns (100 µm ID, laser pulled in-house with Sutter P-2000, Novato CA) packed with 3 µm 120 Å reversed phase C18 beads (Dr. Maisch, Ammerbuch, DE). The LC gradient was 90 min long with 5−35% B at 300 nL/min. LC solvent A was 0.1% (v/v) aq. acetic acid and LC solvent B was 20% 0.1% (v/v) acetic acid, 80% acetonitrile. MS data was collected with a Thermo Fisher Scientific Orbitrap Fusion Lumos using a data-dependent data acquisition method with a Orbitrap MS1 survey scan (R=60K) and as many Orbitrap HCD MS2 scans (R=30K) possible within the 2 second cycle time.

MS data was analyzed in the MaxQuant software identifying biotinylated proteins. Protein groups identified were further analyzed in the Perseus software by filtering out of contaminants, normalization, and imputed for data for Figures S6A-B and S7E-P only. Hits were filtered using gene ontology analysis via Panther database.

In vitro fluorescence characterization

A Synergy Neo2 Microplate Reader (BioTek) was used for all in vitro fluorescence measurements. Assays were performed in 1x PBS. The purified protein components

(+50μM DFHBI-1T for mFAP2a experiments) were placed in 96-well black-well clear-bottom plates, centrifuged at 1,000g for 1 min, and incubated for 30 min at room temperature to enable pre-equilibration. Fluorescence measurements in the absence of target were taken every 1 min after injection (0.1 s integration and 10 s shaking during intervals) at the indicated wavelengths: For emission spectra, the wells were excited at wavelengths indicated in figure legends and the respective emission was recorded at 5 nm intervals.

Time-lapse epifluorescence imaging

Cells were washed twice with FluoroBrite DMEM imaging media and subsequently imaged in the same media in the dark at room temperature. Forskolin, EGF, A115, α-CD3ε + α-CD28 were added as indicated. Epifluorescence imaging was performed on a Yokogawa CSU-X1 spinning dish confocal microscope with either a Lumencor Celesta light engine with 7 laser lines (408, 445, 473, 518, 545, 635, 750 nm) or a Nikon LUN-F XL laser launch with 4 solid state lasers (405, 488, 561, 640 nm), 40x/0.95 NA objective and a Hamamatsu ORCA-Fusion scientific CMOS camera, both controlled by NIS Elements software (Nikon). The following excitation/emission filter combinations (center/bandwidth in nm) were used: CFP: EX445 EM483/32, CFP/YFP FRET: EX445 EM542/27, YFP: EX473 EM544/24, GFP: EX473 EM525/36, RFP: EX545 EM605/52, Far Red (e.g. AlexaFluor 647): EX635 EM705/72, 450: EX445 EM525/36, 500: EX488 EM525/36. Exposure times were 100 ms for acceptor direct channel and 500ms for all other channels, with no EM gain set and no ND filter added. Cells that were too bright (acceptor channel intensity is 3 standard deviations above mean intensity across experiments) or with significant photobleaching prior to drug addition were excluded from analysis. All epifluorescence experiments were subsequently analyzed using Image J. Brightfield images were acquired on the ZOE Fluorescent Cell Imager (BioRad).

QUANTIFICATION AND STATISTICAL ANALYSIS

FRET biosensor analysis

Raw fluorescence images were corrected by subtracting the background fluorescence intensity of a cell-free region from the emission intensities of biosensor-expressing cells. Cyan/yellow emission ratios were then calculated at each time point (*R)*. For some curves, the resulting time courses were normalized by dividing the emission ratio at each time point by the basal ratio value at time zero (R/R_0), which was defined as the emission ratio at the time point immediately preceding drug addition (R_0). Graphs were plotted using GraphPad Prism 8 (GraphPad).

Co-localization analysis

For co-localization analysis, cell images were individually thresholded and underwent Coloc 2 analysis on ImageJ.

Quantification of cellular puncta

For analysis of puncta number, cell images were individually thresholded and underwent particle analysis with circularity and size cutoffs in ImageJ.

Time-to-half maximum kinetic analysis

Time-to-half maximum ($t_{1/2}$) analysis was done similarly to a previous publication using MATLAB code (Zhang et al., 2020).

Statistics and reproducibility

No statistical methods were used to predetermine the sample size. No sample was excluded from data analysis, and no blinding was used. All data were assessed for normality. For normally distributed data, pairwise comparisons were performed using unpaired two-tailed Student's t tests, with Welch's correction for unequal variances used as indicated. Comparisons between three or more groups were performed using ordinary one-way or two-way analysis of variance (ANOVA) as indicated. For data that were not normally distributed, pairwise comparisons were performed using the Mann-Whitney U test, and comparisons between multiple groups were performed using the Kruskal-Wallis test. All data shown are reported as mean $\pm$ SEM and error bars in figures represent SEM of biological triplicates. All data were analyzed and plotted using GraphPad Prism 8 including non-linear regression fitting.

Acknowledgements:

We acknowledge funding from HHMI (J.Z.Z. and D.B.), Helen Hay Whitney Foundation (J.Z.Z.), the Audacious Project at the Institute for Protein Design (J.Z.Z, D.B.), NIH grants (R01GM129090 (S-E.O.), R01GM145011 (D.J.M.), and R01GM086858 (D.J.M.). We thank J.C. Klima, R.A. Langan, and S.E. Boyken for discussion on LOCKR sensor development, B. Fiala at the Institute for Protein Design for providing SARS-CoV-2 RBD and LCB1, A. Luis for help in processing mass spectrometry samples, I. C. Haydon for providing some schematics in the manuscript, A.Y. Ting for discussion on the split proximity labeler, R. Bayliss and J. Sampson for EML4-Alk constructs and cell lines, M. Ahlrichs for help with mammalian cells and cell culture, and M.R. Philips and T.G. Bivona for fruitful discussion of the Ras results.

Author contributions:

J.Z.Z. conceived and supervised the project. J.Z.Z., D.J.M., and D.B. designed the experiments. J.Z.Z. and W.H.N. performed all experiments. S.E.O. ran samples through mass spectrometry. J.Z.Z., D.J.M, and D.B. wrote the original draft. All authors reviewed and commented on the manuscript.

Competing interest:

J.Z.Z., D.J.M., and D.B. are co-inventors in a provisional patent application (application number 63/380,884 submitted by the University of Washington) covering the biosensors described in this manuscript.

Figure Legends:

Figure 1: *De novo* designed Ras-reporting LOCKR-based sensor (Ras-LOCKR-S) measures endogenous Ras activity.
(A) Schematic of optimized Ras-LOCKR-S consisting of fluorescent protein (FP)-tethered Cage (left) and Key (right) proteins where GTP-loaded Ras binds to Ras binding domain (RasBD), thus increasing FRET efficiency.
(B) Top: 293T cells transfected with either Ras-LOCKR-S wildtype (WT) or $RasBD^{R89L}$ negative control (NC) and their representative epifluorescence images (FRET, CFP channel, pseudocolored raw FRET ratio) shown over time after 100ng/mL EGF stimulation. Bottom: Normalized yellow/cyan (Y/C) emission ratio changes in either 293T (upper left) or CIAR-PM (used KRas4a CAAX for PM localization) cells (upper right) and stimulated with 100ng/mL EGF or 250nM A115, respectively (n=10 cells per condition).
(C) (left) Starting raw Y/C emission ratios and (right) average normalized Y/C emission ratio changes in Ras-LOCKR-S-expressing 293T cells co-expressing nothing else (endogenous Ras), Ras (+HRas), constitutively active Ras (+HRas G12V), or dominant negative Ras (+HRas S17N) (left: n=10 cells per condition, right: n=23 cells per condition). Solid lines indicate representative average time with error bars representing standard error mean (SEM). Bar graphs represent mean $\pm$ SEM. ****p < 0.0001, ***p < 0.001, ordinary one-way ANOVA. Scale bars = 10μm.

Figure 2: Ras-LOCKR-S reports cell-type specific differences in endomembrane Ras activity.
(A) Schematic of subcellularly targeted Ras-LOCKR-S and CIAR.
(B) Heat map of 293T cells stably expressing localized CIAR and localized Ras-LOCKR-S. Color represents average emission ratio response from localized Ras-LOCKR-S.
(C) Average normalized Y/C emission ratio responses of 293T cells expressing Ras-LOCKR-S localized to golgi via N-terminus of eNOS, ER via N-terminus of CYP450, PM lipid raft regions (PM LR) via N-terminus of Lyn, or PM non lipid raft regions (PM nonLR) via KRas 4b CAAX (n=at least 10 cells per condition). Cells were stimulated with 100ng/mL EGF.
(D) Heat map of Jurkat T-cells stably expressing localized CIAR and localized Ras-LOCKR-S. Color represents average emission ratio response from localized Ras-LOCKR-S.
(E) Average normalized Y/C emission ratio responses of 293T cells expressing Ras-LOCKR-S localized to golgi via N-terminus of eNOS, ER via N-terminus of CYP450, PM lipid raft regions (PM LR) via N-terminus of Lyn, or PM non lipid raft regions (PM nonLR) via KRas 4b CAAX (n=at least 10 cells per condition). Cells were stimulated with 5μg/mL of α-CD3ε + α-CD28.
(F) Jurkat cells either stimulated with 5μg/mL (high dose) or 1μg/mL (low dose) of α-CD3ε + α-CD28 or expressing localized CIAR and stimulated with 250nM A115 were measured for IL-2 secretion via ELISA (n=3 experimental repeats per condition).

Solid lines in C indicate a representative average time course with error bars representing standard error mean (SEM). Solid lines in E indicate average time courses of Y/C emission ratio changes from all cells combined from 3 experiments with error bars representing standard error mean (SEM). Bar graphs represent mean ± SEM. ****p < 0.0001, ***p < 0.001, **p < 0.01, *p < 0.05 ordinary one-way ANOVA.

Figure 3: *De novo* designed Ras-dependent LOCKR-based proximity labeler (Ras-LOCKR-PL) profiles components in specified Ras signaling microdomains.

(A) Schematic of optimized Ras-LOCKR-PL consisting of split TurboID tethered to Cage and Key proteins where active Ras binds to RasBD, allowing the reconstitution of functional TurboID and biotinylation of neighboring proteins.

(B) Representative immunoblots of CIAR-PM cells with 500μM biotin with or without 250nM A115 (labeled "A") for 16 hrs. Ras-LOCKR-PL without RasBD compared to WT Ras-LOCKR-PL (n=3 experimental repeats).

(C-D) Subcellularly localized Ras-LOCKR-PL or full-length TurboID expressed and underwent either immunoblotting (C) or immunostaining (D) (neutravidin for streptavidin). Bar graphs represent mean ± SEM. **p < 0.01 unpaired two-tailed Student's t-test. Scale bars = 10μm.

Figure 4: *In situ* activation of Ras at the golgi by golgi-resident Sos1.

(A) Volcano plot of mass spectrometry results of CIAR-PM cells expressing golgi-localized Ras-LOCKR-PL, stimulated for 3 hrs with 500μM biotin and with (right) or without 250nM A115 (left), and underwent streptavidin pulldown. Hits labeled are Ras pathway effectors.

(B) Representative epifluorescence images of 293T cells expressing Sos1-mCh and golgi-targeted (N-terminus of eNOS) EGFP stimulated with 100ng/mL EGF.

(C-D) Top: Schematic describing experiment. Bottom: Y/C emission ratio changes of 293T cells expressing either golgi-localized (C) or PM nonLR-localized Ras-LOCKR-S and co-expressing either PM-localized KRas4B^{S17N} or golgi-localized Ras^{S17N} (remove CAAX and add N-terminus of eNOS) (n=at least 13 cells per condition). These cells were stimulated with 100ng/mL EGF.

(E) Hypothesized mechanism for endogenous Ras signaling at golgi. Ras activated at the PM relays down to the golgi region and binds to the allosteric site of golgi-resident Sos1, thus accelerating GTP exchange for local Ras.

Solid lines indicate a representative average time course of Y/C emission ratio changes with error bars representing standard error mean (SEM). Scale bars = 10μm.

Figure 5: Identifying upstream drivers of oncogenic Ras activity inside EML4-Alk granules.

(A) Representative epifluorescence images of Beas2B (wildtype lung) transfected with YFP-fused EML4-Alk variant 1 (v1) and GFP nanobody (GFPnb)-fused V5-tagged TurboID or GFPnb-fused Myc-tagged Ras-LOCKR-PL.

(B) Representative epifluorescence images of Beas2B cells expressing GFP-tagged EML4-Alk v1 or v3, treated with 1μM YB-0158 for 1 hr and immunostained for SAM68. Arrows indicate co-localization of EML4-Alk with SAM68 puncta.

(C) Average raw emission ratios (Y/C) in the punctate regions of Beas2B cells expressing Ras-LOCKR-S WT or NC sensor fused to EML4-Alk v1. Cells were treated with either DMSO or 1μM YB-0158 for 1 hr (n=at least 15 cells per condition).
(D) Schematic of localizing Ras-LOCKR-PL to Ras-active EML4-Alk granules and how SAM68 inhibition by disrupting SAM68:Grb2 interactions decreases local Ras activity in EML4-Alk granules.
Bar graphs represent mean $\pm$ SEM. ****p < 0.0001 one-way ANOVA. Scale bars = 10μm.

Figure 6: Ras^{G12C} inhibitor induces MVP-mediated scaffolding of MAPK pathway components to promote oncogenic golgi-localized Ras signaling.
(A) Schematic describing the question at hand: how does Ras^{G12C} inhibition lead to adaptive signaling and resistant tumors?
(B) Representative immunoblot of H358 (lung $KRas^{G12C}$ heterozygous) and MIA PaCa-2 (pancreas $KRas^{G12C}$ homozygous) cells treated over time with 100nM AMG-510.
(C) Raw emission ratios (Y/C) of localized Ras-LOCKR-S in H358 cells treated over time with 100nM AMG-510 (n=17 cells per condition).
(D) Cell growth curves of H358 or MIA PaCa-2 cells expressing localized Ras^{S17N} and/or treatment of 100nM AMG-510 (n=3 experiments per condition). PM: KRas4B CAAX, gol: removed CAAX and add N-terminus of eNOS, ER: removed CAAX and add N-terminus of CYP450.
(E) Heat map colored either by student's t-test difference or the difference between 24 and 4 hr AMG-510 treatment (labeled "Difference") in H358 cells expressing golgi-localized Ras-LOCKR-PL, incubated with 500μM biotin and either with or without 100nM AMG-510, pulled down by streptavidin beads, and ran through mass spectrometry. With experimental comparisons listed on top, student's t-test difference indicates propensity of protein to be more enriched in the golgi Ras signaling microdomain when AMG-510 is added. Difference between 24 and 4 hr represents enrichment of proteins in the golgi Ras signaling compartment throughout time during AMG-510 treatment.
(F) Comparison of raw emission ratios of localized Ras-LOCKR-S between no KD versus MVP KD in H358 cells treated with 100nM AMG-510 over indicated times (n=17 cells per condition).
(G-H) H358 or MIA PaCa-2 cells expressed golgi-localized Ras-LOCKR-PL, were incubated with 500μM biotin and either with or without 100nM AMG-510 for 24 hrs, and stained for PLA with anti-biotin and anti-MVP antibodies. (G) quantification of Biotin:MVP PLA puncta per cell across conditions and (H) correlation between golgi-localized Ras-LOCKR-S raw emission ratio and Biotin:MVP PLA puncta per cell across conditions (n=16 cells per condition).
(I) H358 or MIA PaCa-2 cells transfected with golgi-Ras-LOCKR-S, treated with or without MVP siRNA for 2 days, incubated with 100nM AMG-510 for 24 hrs, and immunostained and probed for Shp2:POI interactions via PLA. Shown is quantification across conditions (n=12 cells per condition).
Solid lines indicate average time courses of relative growth (normalized to day 0) from all cells combined from 3 experiments with error bars representing standard error mean (SEM). Bar graphs represent mean $\pm$ SEM. For C and F, ****p < 0.0001, ***p < 0.001, **p < 0.01, ordinary two-way ANOVA comparing to 0 hr for Ras-LOCKR-S localized to

same subcellular region. For G and I, ****p < 0.0001, ***p < 0.001, **p < 0.01, ordinary one-way ANOVA.

Figure 7: MVP connects Ras with VDAC to promote mitochondria-localized Ras activity and pro-Warburg effect.

(A) H358 or MIA PaCa-2 cells transfected with either Cyto-PercevalHR, treated with or without 100nM AMG-510 for 24 hrs, and immunostained and probed for MVP:pan VDAC interactions via PLA. Shown is quantification across conditions (n=14 cells per condition).

(B) H358 or MIA PaCa-2 cells transfected with either Cyto-PercevalHR, transfected with or without MVP siRNA, treated with 100nM AMG-510 for 24 hrs, and immunostained and probed for pan Ras:pan VDAC interactions via PLA. Shown is quantification across conditions (n=14 cells per condition).

(C) Raw emission ratios (Y/C) of H358 or MIA PaCa-2 transfected with either mito-Ras-LOCKR-S WT, mito-Ras-LOCKR-S NC sensor, or mito-Ras-LOCKR-S WT and MVP siRNA, and treated over time with 100nM AMG-510 (n=14 cells per condition). Mitochondrial localization mediated by N-terminus of DAKAP (Ma et al., 2002).

(D) Raw emission ratios (500/450) of H358 or MIA PaCa-2 transfected with cyto-PercevalHR and either with or without MVP siRNA and treated over time with 100nM AMG-510 (n=14 cells per condition).

(E) Schematic of MVP scaffolding of MAPK pathway components as an adaptive method for resistance to Ras^{G12C} inhibitors.

Bar graphs represent mean ± SEM. For A-B, ****p < 0.0001, ***p < 0.001, *p < 0.05, student's T-test. For C-D, ****p < 0.0001, **p < 0.01, ordinary two-way ANOVA comparing to 0 hr within condition.

Figure S1: Design and characterization of Ras-LOCKR-S to track compartmentalized endogenous Ras activity dynamically and specifically, Related to Figure 1.

(A) The different aspects of Ras-LOCKR-S that were tuned.

(B-E) FRET-based LOCKR sensors modifying lucCageRBD, which senses RBD of SARS-CoV-2 spike protein via binding to the *de novo* protein binder LCB1 (Cao et al., 2020), (B) with CFP and YFP as FRET donor and acceptor, respectively. Two placements of the FPs were tested *in vitro* for yellow/cyan FRET fluorescence (C), CFP fluorescence (D), and normalized yellow/cyan (Y/C) emission ratio changes (normalized to no RBD) (E) with a range of RBD concentrations ([Cage]=[Key]=1mM).

(F) Emission spectra (excitation wavelength: ECFP+YPet, ECFP only, buffer only=450nm, YPet only=510nm) of the two Key-Cage pairs against a range of RBD concentrations ([Cage]=[Key]=1mM) (left and middle) and the Key or Cage proteins alone (right).

(G) Round 1: various FRET-based Ras-LOCKR-S candidates with different RasBD grafting positions on latch using Rosetta-based GraftSwitchMover (see Methods) were tested in 293T (100ng/mL EGF stimulation) and CIAR-PM (250nM A115 stimulation) cells with percent emission ratio (Y/C) changes reported (n=at least 21 cells per condition). Only YFP-tagged Cage and CFP-tagged Key were tested as YFP-tagged Key did not show fluorescence.

(H) Round 2: RasBD placements identified in Round 1 were used in unimolecular (only Cage, no Key) without linker (uni), with linker (uniL), and bimolecular (with P2A sequence) formats. One of the bimolecular designs showed consistent responses to EGF and A115 (left) (n=at least 18 cells per condition) with their emission ratio (Y/C) ratio changes plotted (right) (n=at least 8 cells per condition) showing expected Ras dynamics (EGF-stimulated Ras dynamics should be transient, A115-stimulated Ras dynamics should be sustained).
(I-J) Round 3, bimolecular: point mutations to weaken latch:cage or key:cage interactions (the N-terminal half of latch and key are similar) (J) are identified via structure predictions and implemented in the bimolecular Ras-LOCKR-S candidate identified in Round 2. Some Ras-LOCKR-S candidates that respond to EGF and A115 do not report the expected Ras dynamics and are boxed in red, while those with higher (compared to parent) emission ratio (Y/C) changes to EGF and A115 with expected Ras dynamics are boxed in green and negative controls (NC, $RasBD^{R89L}$) shows negligible emission ratio (Y/C) changes (bar: n=at least 19 cells per condition, time-course: n=at least 10 cells per condition).
(K) CIAR-PM cells expressing Ras-LOCKR-S_P2A2_L3K2 and co-expressing either HRas, constitutively active HRas ($HRas^{G12V}$), or dominant negative HRas ($HRas^{S17N}$) are stimulated with A115. Emission ratio (Y/C) changes (left, n=at least 11 cells per condition) and starting emission ratios (Y/C) (right, n=25 cells per condition) are reported.
(L) Ras-LOCKR-S_P2A2_L3K2 was tested for Ras but not Rap selectivity in 293T cells expressing RapGAP and stimulated with EGF (left, n=at least 25 cells per condition) and with expected Ras dynamics (right, n=13 cells per condition).
(M) Testing of RapGAP (Scrima et al., 2008) in 293T cells using Rap1A and Rap1B FLARE activity reporters(O'Shaughnessy et al., 2019). Emission ratio (Y/C) changes of 293T cells expressing either Rap1A FLARE or Rap1B FLARE with and without RapGAP co-expression are stimulated with either EGF (left) or 50μM Forskolin (Fsk) (n=at least 25 cells per condition).
See Table S1 for domain structures and sequences. For all graphs, solid lines indicate representative average time courses of Y/C emission ratio changes with error bars representing standard error mean (SEM). Bar graphs represent mean $\pm$ SEM. ****p < 0.0001, ordinary one-way ANOVA.

Figure S2: Characterization of localized Ras-LOCKR-S and CIAR in 293T cells, Related to Figure 2.
(A-F) Cells expressing Ras-LOCKR-S (final version) tagged with N-terminus of Lyn (PM LR) (A), KRas4b CAAX (PM nonLR) (B), N-terminus of CYP450 (ER) (C), N-terminus of eNOS (golgi) (D), or N-terminus of GalT (golgi) (E) were stimulated either with EGF or A115. Shown are respective representative epifluorescence images (left, CFP or YFP channel, FRET channel, and pseudocolored raw FRET ratio) and emission ratio (Y/C) changes (right, n=at least 15 cells per condition). (F) These cells were immunostained for respective localization markers. Localization sequences: Golgi: N-terminus of eNOS (Fulton et al., 2004) or N-terminus of GalT (Schaub et al., 2006), ER: N-terminus of CYP450 (Szczesna-Skorupa and Kemper, 2000), PM lipid raft regions (PM LR): N-terminus of Lyn (Gao and Zhang, 2008), PM non lipid raft regions (PM nonLR): KRas4B CAAX (Gao and Zhang, 2008).

(G) CIAR localized to PM (KRas4a CAAX), ER (CYB5A$^{100\text{-}134}$) (Fox et al., 2015), and golgi (Giantin$^{3131\text{-}3259}$) (Satoh et al., 2019) is stably expressed in 293-TRex cells, which were immunostained for CIAR via Bcl-xL (4a/PM) or Flag tag (ER and golgi) and their respective localization markers with representative epifluorescence images shown.
(H) Emission ratio (Y/C) changes after A115 addition onto cells stably expressing golgi-localized CIAR (CIAR-golgi) and transfected with subcellularly localized Ras-LOCKR-S.
(I-J) Localized CIAR stable cells or 293T cells were stimulated for different durations with 250nM A115 or 100ng/mL EGF, respectively, and then immunoblotted (I) or immunostained (J) for phospho-Erk.
(K) Top and middle: Y/C emission ratio changes in 293T cells stimulated with 100ng/mL EGF (red) or CIAR-PM cells stimulated with 250nM A115 (blue) expressing either Ras-LOCKR-S (Ras) or the FRET-based Erk kinase activity reporter (EKAR4) (Erk). With representative epifluorescence images of localized Ras-LOCKR-S (YFP shown for PM non lipid raft regions (PM nonLR), CFP shown for the rest) shown, these sensors are localized to PM lipid raft regions (PM LR) via N-terminus of Lyn, PM nonLR via KRas 4b CAAX, golgi via N-terminus of eNOS, or ER via N-terminus of CYP450 (n=10 cells per condition). Bottom: Time to half maximum ($t_{1/2}$) measurements of individual emission ratio curves (n=10 cells per condition).
(L) Characterizing the A115-dose response behavior of PM or golgi-localized sensors in CIAR-PM cells (n=18 cells per condition).
For L, solid lines in E indicate EC50 fit with points representing average normalized to maximum Y/C emission ratio responses from all cells combined from 3 experiments with error bars representing standard error mean (SEM). For rest, solid lines indicate representative average time courses of Y/C emission ratio changes with error bars representing standard error mean (SEM). Bar graphs represent mean $\pm$ SEM. ****p < 0.0001, ordinary one-way ANOVA. Scale bars = 10μm.

Figure S3: Characterization of localized Ras-LOCKR-S and CIAR in Jurkat T-cells, Related to Figure 2.
(A) Representative epifluorescence images of Jurkat T-cells and 293T cells immunostained for Ras and giantin (golgi marker).
(B) Representative epifluorescence images of Jurkat cells expressing either subcellularly localized Ras-LOCKR-S and immunostained with respective localization markers.
(C-D) Representative phospho-Erk immunoblot (C) and brightfield images (D) of Jurkat cells exposed to various concentrations of A115 for 2 days.
(E) Representative epifluorescence images of Jurkat cells expressing subcellularly localized CIAR (ER: CYB5A$^{100\text{-}134}$, golgi: Giantin$^{3131\text{-}3259}$) and immunostained with respective localization markers.
(F) Emission ratio (Y/C) changes of Jurkat cells expressing both localized Ras-LOCKR-S stimulated and CIAR localized to the same region and stimulated with 250nM A115 (n=at least 12 cells per condition).
(G) Emission ratio (Y/C) changes of Jurkat cells expressing localized Ras-LOCKR-S and stimulated with 1μg/mL α-CD3ε + α-CD28 (n=at least 12 cells per condition).
(H) Jurkat cells either stimulated with α-CD3ε + α-CD28 or expressing localized CIAR and stimulated with 250nM A115 were stained for CD69 surface expression. FACS histograms shown (n=3 experimental repeats).

(I) Normalized cell count of Jurkat cells stimulated with α-CD3ε + α-CD28 or A115 and some conditions expressing either PM-localized (CIAR-PM) or golgi-localized (CIAR-golgi) CIAR (n=3 experiments per condition).
Solid lines indicate average time courses of Y/C emission ratio changes from all cells combined from 3 experiments with error bars representing standard error mean (SEM). Scale bar = 10μm in A, B, and E, scale bar = 100μm in D.

Figure S4: Development and characterization of Ras-LOCKR-PL, Related to Figure 3.
(A-B) Split ContactID-based LOCKR proximity labelers were tested using similar architecture to lucCageRBD. Different grafting positions of the smaller bit of ContactID on the latch using Rosetta-based GraftSwitchMover (see Methods) and different linker lengths between larger bit of ContactID and Key were tested in 293T cells transfected with Flag-tagged Cage, Myc-tagged Key, full length ContactID (FL CID), and HA-tagged RBD (receptor binding domain of SARS-CoV-2 spike protein) with 5x nuclear exclusion sequence. After 16 hr 500μM biotin incubation, these cells were subsequently immunoblotted for the transfected proteins and biotinylation via streptavidin.
(C-D) Split TurboID (split site TurboID$^{73/74}$)-based LOCKR proximity labelers modifying lucCageRBD were tested in 293T cells transfected with Cage, Key, full length TurboID (FL TID), and RBD and immunoblotted for biotinylation. Different placements of the split TurboID and linker lengths between split TurboID and Cage/Key were tested with the Ras-LOCKR-PL candidate that induced highest increase in biotinylation upon RBD expression boxed in green and optimized further.
(E-I) Testing of Ras-LOCKR-PL candidates was done via western blotting of CIAR-PM cells incubated with 250nM A115 (labeled A) or 100ng/mL EGF (labeled E) and 500μM biotin for either 16 hr (E-H), 1 hr (I, left), or 3 hr (I, right). RasBD was grafted onto the latch using GraftSwitchMover and tested for increases in biotinylation after Ras activation by A115 (FL = full length TurboID). The highest dynamic range Ras-LOCKR-PL candidates are boxed in green (F) and further optimized by either weakening latch:cage interaction by mutating latch (G) or weakening key:cage interaction by mutating the Key (2 different Cages tested for left and right) (H). C-terminal Key truncations were also tested to weaken key:cage interaction (H). The highest dynamic range Ras-LOCKR-PL candidates boxed in green (H) were tested in shorter time regimes either with A115 or EGF (I).
(J-K) Representative immunoblots of CIAR-PM cells with 500M biotin with or without 250nM A115 (labeled “A”) for 16 hrs. (J) Negative controls (Myc-tagged Key or Flag-tagged Cage only), positive control (TurboID-CRaf), and Ras-LOCKR-PL tested designs (Key+Cage) were expressed with or without A115. Cells underwent streptavidin pulldown (PD) and probed for Ras with Ras PD over whole cell lysate (WCL) quantified (n=at least 4 experimental repeats). (K) Optimized Ras-LOCKR-PL co-expressed with various HA-tagged Ras mutants/effectors or Rap effector (CalDAG-GEFI).
(L) Schematic of subcellularly targeted Ras-LOCKR-PL.
(M) Representative epifluorescence images of 293T cells transfected with subcellularly localized Ras-LOCKR-PL and immunostained for respective localization markers.

See Table S2 for domain structures and sequences. Bar graphs represent mean ± SEM, n=at least 3 experiments per condition. **p < 0.01, *p < 0.05, unpaired two-tailed Student's t-test. Scale bar = 10μm.

Figure S5: Sos1 forms resident golgi-proximal puncta that is not influenced by EGFR signaling, Related to Figure 4.

(A-B) HeLa, 293T, and Beas2B cells were immunostained for different Sos1 antibodies (Abcam, Novus, Thermo is shown in Figure 4C) and the golgi marker giantin with statistics/quantification (colocalization metrics (n=3 experiments per condition) and number of Sos1 puncta per cell (n=at least 18 cells per condition)) (A) and representative epifluorescence images (B) shown.

(C) Representative epifluorescence images of CIAR-PM cells stimulated with 250nM A115 for different durations and immunostained for Sos1, giantin, and CIAR (via its Bcl-xL autoinhibitory domain (Rose et al., 2017a)).

(D) 293T cells expressing golgi-localized GFP (N-terminus of eNOS) and mCherry-tagged Sos1 truncations were stimulated with 100ng/mL EGF. Number of golgi-proximal Sos1 puncta quantified (top, n=at least 21 cells per condition) and representative epifluorescence images (bottom) shown. Arrows indicate co-localization of Sos1 mutant with golgi-localized GFP.

(E-F) 293T cells stimulated with EGF for different durations and immunostained for Sos1 (Thermo) and giantin with representative epifluorescence images (E) and quantification (colocalization metrics (n=3 experiments per condition), percentage Sos1 puncta proximal to golgi (n=at least 29 puncta per condition), number of Sos1 puncta per cell (n=at least 20 cells per condition)) (F) shown.

(G-J) Top: Schematic describing experiment. Bottom: Emission ratio (Y/C) changes of indicated Ras-LOCKR-S transfected in indicated cells co-expressing PM-localized or golgi-localized Ras^{S17N} (n=at least 13 cells per condition).

(K-L) Y/C emission ratio changes (n=at least 7 cells per condition) (top) or starting raw emission ratios (n=17 cells per condition) (bottom) of either golgi-localized (K) or PM-localized (L) Ras-LOCKR-S in A549 Sos1 KO cells stimulated with 100ng/mL EGF and co-expressing Sos1 or allosteric Ras-GTP site mutated (W729E eliminates allosteric binding site).

Solid lines indicate representative average time courses of Y/C emission ratio changes with error bars representing standard error mean (SEM). Bar graphs represent mean ± SEM. **p < 0.01, comparison to Sos1 FL (FL), ordinary one-way ANOVA. Scale bars = 10μm.

Figure S6: Ras-LOCKR tools identify the Ras activity and environment inside EML4-Alk granules, Related to Figure 5.

(A-B) Beas2B cells transfected with Ras-LOCKR-S or NC sensor tethered to EML4-Alk variant 1 (v1)/variant 3 (v3) full length or with trimerization domain deleted (ΔTD). (A) Representative epifluorescence images and (B) raw emission ratios (Y/C) are shown.

(C) Representative epifluorescence images of Beas2B cells transfected with V5-tagged TurboID or Myc-tagged Ras-LOCKR-PL tethered to EML4-Alk v1/v3 and immunostained for respective tags and biotinylation via streptavidin.

(D) Domain structures of constructs used.

(E) Representative epifluorescence images of Beas2B (wildtype lung) transfected with EML4-Alk variant 3 (v3), full length V5-tagged TurboID tethered to GFP nanobody (GFPnb), or Myc-tagged Ras-LOCKR-PL tethered to GFPnb.
(F-H) Volcano plot of mass spectrometry results of Beas2B cells expressing indicated constructs and stimulated for indicated durations with 500μM biotin. Plotted differences are comparing the first condition listed in the title (right) against the second condition listed (left). Experimental comparisons are grouped for proteins enriched in Ras-active EML4-Alk v1 granules (E), more abundant in EML4-Alk v1 versus v3 conditions (F), or enriched in Ras-active EML4-Alk v3 granules (G).
(I) Heat maps (colored by student's t-test difference) displaying the signaling-related proteins detected in Beas2B cells transfected with Ras-LOCKR-PL or TurboID constructs localizing to EML4-Alk v1/v3 granules and incubated with 500μM biotin for indicated times. Experimental comparisons are grouped for proteins enriched in Ras-active EML4-Alk v1 granules (left), more abundant in EML4-Alk v1 versus v3 conditions (middle), or enriched in Ras-active EML4-Alk v3 granules (right). With experimental comparisons listed on top, student's t-test difference indicates propensity of protein to be more enriched in the first listed experimental sample compared to second with 0 indicating no difference. Blue arrows are proteins identified previously to be enriched in EML4-Alk v1 granules, red arrows are proteins shown previously to be excluded from EML4-Alk v1 granules, and black arrows are new hits that were verified later on to be sequestered in EML4-Alk granules.
Bar graphs represent mean $\pm$ SEM. ****p < 0.0001, **p < 0.01, ordinary two-way ANOVA. Scale bars = 10μm.

Figure S7: Identification of upstream drivers of Ras signaling inside EML4-Alk condensates, Related to Figure 5.
(A) Representative epifluorescence images of Beas2B cells expressing GFP-tagged EML4-Alk v1 or v3, treated with indicated inhibitors for 1 hr (1M YB-0158, 10M BIO-11006), and immunostained for hits identified in the mass spectrometry analysis. Arrows indicate co-localization of EML4-Alk with probed protein.

(B) Representative immunoblot of Beas2B cells transfected with V5-tagged EML4-Alk v1/v3 full length or with trimerization domain deleted (ΔTD), subjected to V5 immunoprecipitation, and probed for hits identified in the mass spectrometry analysis.

(C) Student's t-test difference of the two hits (SAM68 and MARCKS) that were probed further for their signaling and oncogenic effects. Blue is high value, white is value of 0, and red is low value.
(D) List of inhibitors used, their abbreviations, and their target. MARCKS inhibition (either by dephosphorylating MARCKS through Protein Kinase C inhibitor (Gö6983) or a competitive peptide (BIO-11006) (Li et al., 2001)) or SAM68 inhibition (by blocking binding to SH3 domains) (Masibag et al., 2021).
(E) Representative immunoblot of Beas2B cells treated with 1M YB-0158, underwent Sam68 immunoprecipitation, and probed for Sam68 and Grb2. Top: Sam68 immunoprecipitation. Bottom: whole cell lysate.

(F) Average raw emission ratios (Y/C) in the punctate regions of Beas2B cells expressing EML4-Alk localized Ras-LOCKR-S WT or NC sensor with addition of DMSO, 1M YB-0158, or 10M BIO-11006 for 1 hr.
(G) Representative immunoblot of H3122 and H2228 cells treated for 1 hr with either constant concentration of YB-0158 (200nM) and a range of concentrations of Ceritinib (1nM-1mM) (left) or a constant concentration of Ceritinib (200nM) and a range of concentrations of YB-0158 (1nM-1mM) (right).
(H) Representative immunoblot of Beas2B (WT), H3122 (lung adenocarcinoma EML4-Alk v1), and H2228 (lung adenocarcinoma EML4-Alk v3) cell lines incubated for 1 hr with inhibitors to Alk (Ce: 1M Ceritinib), MARCKS (B: 10M BIO-11006), and SAM68 (Y: 1M YB-0158).
(I) Representative immunoblot of Beas2B, H3122, and H2228 cells treated for 1 hr with varying concentration of Ceritinib (1nM-1mM), YB-0158 (1nM-1mM), and BIO-11006 (10nM-10mM). Relative phosphorylated over total protein quantified (midpoint 10^3 relative concentration is taken from Figure 6B) (n=3 experiments per condition).
(J) Cell count of Beas2B, H3122, H2228 cell lines incubated for 1 week with varying concentrations of inhibitors to Alk (1pM-1.6M Crizotinib (Cz), 1pM-1.6M Ceritinib (Ce)), PKC (1pM-1.6M Gö6983), MARCKS (10nM-16mM BIO-11006), SAM68 (1nM-1.6mM YB-0158) (n=3 experiments per condition), or DMSO.
(K) Representative images of crystal violet staining of Beas2B, H3122, and H2228 incubated for 1 week with inhibitors to Alk (Cz: 1M Crizotinib, Ce: 1M Ceritinib), PKC (G: 1M Gö6983), MARCKS (B: 10mM BIO-11006), SAM68 (Y: 1mM YB-0158), and DMSO.
Solid lines indicate IC50 fit with points representing average phospho/total protein ratios for C combined from 3 experiments or average normalized cell count for G. Bar graphs represent mean SEM. ****$p < 0.0001$, *$p < 0.05$ ordinary two-way ANOVA comparing to cells treated with DMSO. Scale bars = 10m.

Figure S8: MVP fuels aberrant golgi-localized Ras signaling during Ras^{G12C} inhibitor treatment, Related to Figure 6.
(A) Raw emission ratios (Y/C) of localized Ras-LOCKR-S in MIA PaCa-2 cells treated over time with 100nM AMG-510 (n=17 cells per condition).
(B) Representative immunoblot of MIA PaCa-2 or H358 cells transfected with Flag-tagged golgi-localized Ras^{S17N}, treated with 100nM AMG-510 over indicated times, and probed for pErk.
(C) Heat maps of H358 or MIA PaCa-2 cells transfected with localized Ras^{S17N} and localized Ras-LOCKR-S incubated with 100nM AMG-510 for indicated times. Colors represent localized ratio between with or without expression of localized Ras^{S17N} (n=15 cells per condition).
(D) Cell growth curves of MIA PaCa-2 cells expressing localized Ras^{S17N} and/or treatment of 100nM AMG-510 (n=3 experiments per condition). PM: KRas4B CAAX, gol: removed CAAX and add N-terminus of eNOS, ER: removed CAAX and add N-terminus of CYP450.
(E-F) Volcano plots of mass spectrometry results of H358 (E) or MIA PaCa-2 (F) cells expressing localized Ras-LOCKR-PL and stimulated for 24 hrs with 500μM biotin and either with or without 100nM AMG-510. Plotted differences are comparing with AMG-510 (right) or without AMG-510 (left).

(G) Heat maps (colored by student's t-test difference) displaying the signaling-related proteins detected in either MIA PaCa-2 or H358 cells transfected with localized Ras-LOCKR-PL and incubated with 500μM biotin and either with or without 100nM AMG-510 for indicated times. With experimental comparisons listed on top, student's t-test difference indicates propensity of protein to be more enriched in the local Ras signaling microdomain when 100nM AMG-510 is added.
(H) Top: Representative fluorescence images of Biotin:POI PLA puncta in either MIA PaCa-2 or H358 cells treated with 500μM biotin and either with or without 100nM AMG-510 for 24 hrs. Bottom: Quantification across conditions (n=22 cells per condition).
(I) Quantification of H358 cells transfected with golgi-Ras-LOCKR-S, transfected with or without POI siRNA for 2 days, and treated with or without 100nM AMG-510 for 24 hrs (n=22 cells per condition).
(J) Top: Representative immunoblot of MIA PaCa-2 or H358 cells transfected with MVP or Scrambled siRNA for 2 days. Bottom: Quantification across conditions (n=3 experiments per condition).
(K) Raw emission ratios of localized Ras-LOCKR-S in MIA PaCa-2 cells treated with MVP siRNA for 2 days and 100nM AMG-510 over indicated times (n=17 cells per condition).
(L) H358 or MIA PaCa-2 cells expressed golgi-localized Ras-LOCKR-PL, were incubated with 500M biotin and either with or without 100nM AMG-510 for 24 hrs, and stained for PLA with anti-biotin and anti-MVP antibodies. Shown are representative fluorescence and pseudocolored images.
(M) Representative epifluorescence images of H358 and MIA PaCa-2 cells treated without (0 hr) or with 100nM AMG-510 (24 hr) and immunostained for MVP and a localization marker for the golgi (Giantin). Colocalization analysis is shown as well (n=3 experiments per condition).
(N) Cell growth curves of H358 or MIA PaCa-2 cells treated either with MVP siRNA, 100nM AMG-510, or 10M SHP099 (n=3 experiments per condition).
Solid lines indicate average time courses of relative growth (normalized to day 0) from all cells combined from 3 experiments with error bars representing standard error mean (SEM). Bar graphs represent mean $\pm$ SEM. For A and K, ****p < 0.0001, ***p < 0.001, **p < 0.01, *p < 0.05, two-way ANOVA comparing to 0hr time point for Ras-LOCKR-S localized at same area. For H-I, ****p < 0.0001, ***p < 0.001, **p < 0.01, *p < 0.05, ordinary one-way ANOVA. Scale bars = 10μm.

Figure S9: MVP is a scaffold for MAPK pathway components to drive golgi-localized Ras signaling during Ras^{G12C} inhibition, Related to Figure 6.
(A-C) H358 or MIA PaCa-2 cells treated with 100nM AMG-510 for 24 hrs were immunostained and probed for MVP:POI interactions via PLA. (A) representative fluorescence images, (B) quantification across conditions, and (C) correlation between pErk levels estimated from immunostaining and MVP:POI PLA puncta per cell (n=14 cells per condition).
(D-E) H358 or MIA PaCa-2 cells transfected with golgi-Ras-LOCKR-S, treated with or without MVP siRNA for 2 days, incubated with 100nM AMG-510 for 24 hrs, and immunostained and probed for Shp2:POI interactions via PLA. (D) Representative fluorescence and pseudocolored images and (E) correlation between golgi-Ras-LOCKR-S emission ratios and Shp2:POI PLA puncta per cell (n=12 cells per condition).

(F-I) H358 or MIA PaCa-2 cells transfected with golgi-Ras-LOCKR-S, treated with or without 100nM AMG-510 for 24 hrs, and immunostained and probed for MVP:Ras isoform interactions via PLA. (F) Representative fluorescence and pseudocolored images, (G-H) quantification across conditions, (I) and correlation between golgi-Ras-LOCKR-S emission ratios and MVP:Ras isoform PLA puncta per cell (n=14 cells per condition).
(J) Raw emission ratios of H358 cells transfected with localized Ras-LOCKR-S and treated with 100nM AMG-510 over time and then subsequent 2 hr treatment with 100M RasON (n=14 cells per condition).
(K) Left: Representative immunoblot of H358 and MIA PaCa-2 with or without MVP siRNA transfection and treated over time with 100nM AMG-510. Right: Densitometry quantification of immunoblots either not normalized (pAkt/Akt) or normalized to 0 hr (the rest).
Bar graphs represent mean SEM. For G-H, ****p < 0.0001, ***p < 0.001, **p < 0.01, *p < 0.05, ordinary one-way ANOVA. For J, ****p < 0.0001, *p < 0.05, ordinary two-way ANOVA comparing against 0 hr time point, ^{xx}p < 0.01, ordinary two-way ANOVA comparing against 72 hr AMG-510 time point. For K, ****p < 0.0001, ***p < 0.001, **p < 0.01, *p < 0.05, ordinary one-way ANOVA comparing against 0 hr time point or to a particular data set (only for pAkt/Akt data). Scale bars = 10μm.

Figure S10: MVP interaction with VDAC induces mitochondrial Ras activity and rewired metabolism during Ras^{G12C} inhibition, Related to Figure 7.
(A-B) Representative epifluorescence images of H358 and MIA PaCa-2 cells treated without (0 hr) or with 100nM AMG-510 (24 hr) and immunostained for either localization markers for golgi (Giantin) and mitochondria (Hsp60) (A) or stained for MVP and Hsp60 (B). Colocalization analysis is shown as well (n=3 experiments per condition).(N) Raw emission ratios (Y/C) of localized Ras-LOCKR-S in MIA PaCa-2 transfected with MVP siRNA and treated over time with 100nM AMG-510 (n=16 cells per condition).
(C) H358 or MIA PaCa-2 cells transfected with either Cyto-PercevalHR, treated with or without 100nM AMG-510 for 24 hrs, and immunostained and probed for MVP:pan VDAC interactions via PLA. Top: Representative fluorescence and pseudocolored images, bottom: correlation between MVP:pan VDAC PLA puncta per cell and cyto-PercevalHR emission ratios (n=14 cells per condition).
(D) H358 or MIA PaCa-2 cells transfected with either Cyto-PercevalHR, transfected with or without MVP siRNA, treated with 100nM AMG-510 for 24 hrs, and immunostained and probed for pan Ras:pan VDAC interactions via PLA. Top: Representative fluorescence and pseudocolored images, bottom: and correlation between pan Ras:VDAC PLA puncta per cell and cyto-PercevalHR emission ratios (n=14 cells per condition).
(E) Representative epifluorescence image of 293T or H358 cells transfected with Mito-Ras-LOCKR-S and probed with MitoTracker Red.
(F) Raw emission ratios (Y/C) of localized Ras-LOCKR-S in H358 and MIA PaCa-2 cells transfected with Mito-Ras-LOCKR-S and either transfected with nothing else, GFP-tagged HRas G12V, or GFP-tagged HRas S17N (n=20 cells per condition).
(G) Raw emission ratios (Y/C) of MIA PaCa-2 cells transfected with either mito-Ras-LOCKR-S WT, mito-Ras-LOCKR-S NC sensor, or mito-Ras-LOCKR-S WT and MVP siRNA, and treated over time with 100nM AMG-510 (n=14 cells per condition). Mitochondrial localization mediated by N-terminus of DAKAP (Ma et al., 2002).

(H) Raw emission ratios (500/450) of MIA PaCa-2 cells transfected with cyto-PercevalHR and either with or without MVP siRNA and treated over time with 100nM AMG-510 (n=14 cells per condition).
(I) Cell growth curves of H358 or MIA PaCa-2 cells treated with some combination of 100nM AMG-510 and 10 μM erastin with MVP KD growth curves transparent (n=3 experiments per condition).
(J-K) Raw emission ratios of H358 cells transfected with either mito-Ras-LOCKR-S or Cyto-PercevalHR and treated with 100nM AMG-510 over time and then subsequent 2 hr treatment with 100M RasON (n=14 cells per condition).
Solid lines indicate average time courses of relative growth (normalized to day 0) from all cells combined from 3 experiments with error bars representing standard error mean (SEM). Bar graphs represent mean ± SEM. For F, ****p < 0.0001, ***p < 0.001, **p < 0.01, *p < 0.05, ordinary one-way ANOVA. For G-H, ****p < 0.0001, ***p < 0.001, **p < 0.01, *p < 0.05, ordinary two-way ANOVA comparing against 0 hr time point. For J-K, ****p < 0.0001, *p < 0.05, ordinary two-way ANOVA comparing against 0 hr time point, ^{x}p < 0.05, ^{xx}p < 0.01, ordinary two-way ANOVA comparing against 72 hr AMG-510 time point. Scale bars = 10μm.

References

Amendola, C.R., Mahaffey, J.P., Parker, S.J., Ahearn, I.M., Chen, W.C., Zhou, M., Court, H., Shi, J., Mendoza, S.L., Morten, M.J., Rothenberg, E., et al. (2019). KRAS4A directly regulates hexokinase 1. Nature. *576*, 482-486.
Augsten, M., Pusch, R., Biskup, C., Rennert, K., Wittig, U., Beyer, K., Blume, A., Wetzker, R., Friedrich, K., and Rubio, I. (2006). Live-cell imaging of endogenous Ras-GTP illustrates predominant Ras activation at the plasma membrane. EMBO Rep *7*, 46–51.
Awad, M.M., Liu, S., Rybkin, I.I., Arbour, K.C., Dilly, J., Zhu, V.W., Johnson, M.L., Heist, R.S., Patil, T., Riely, G.J., et al. (2021). Acquired Resistance to KRASG12C Inhibition in Cancer. New England Journal of Medicine *384*, 2382–2393. https://doi.org/10.1056/NEJMoa2105281.
Berger, W., Steiner, E., Grusch, M., Elbling, L., and Micksche, M. (2009) Vaults and the major vault protein: novel roles in signal pathway regulation and immunity. Cell Mol Life Sci. *66*, 43-61.
Bielli, P., Busà, R., Paronetto, M.P., and Sette, C. (2011). The RNA-binding protein Sam68 is a multifunctional player in human cancer. Endocrine-Related Cancer *18*, R91–R102. https://doi.org/10.1530/ERC-11-0041.
Biskup, C., and Rubio, I. (2014). Real-time visualization and quantification of native Ras activation in single living cells. Methods Mol Biol *1120*, 285–305. https://doi.org/10.1007/978-1-62703-791-4_19.
Bivona, T.G., de Castro, I.P., Ahearn, I.M., Grana, T.M., Chiu, V.K., Lockyer, P.J., Cullen, P.J., Pellicer, A., Cox, A.D., and Philips, M.R. (2003). Phospholipase Cγ activates Ras on the Golgi apparatus by means of RasGRP1. Nature *424*, 694–698.
Bivona, T.G., Quatela, S.E., Bodemann, B.O., Ahearn, I.M., Soskis, M.J., Mor, A., Miura, J., Wiener, H.H., Wright, L., and Saba, S.G. (2006). PKC regulates a farnesyl-electrostatic switch on K-Ras that promotes its association with Bcl-XL on mitochondria and induces apoptosis. Mol Cell *21*, 481–493.

Buettner, R., Papoutsoglou, G., Scemes, E., Spray, D.C. and Dermietzel, R. (2000). Evidence for secretory pathway localization of a voltage-dependent anion channel isoform. Proceedings of the National Academy of Sciences, *97*, 3201-3206.

Cao, L., Goreshnik, I., Coventry, B., Case, J.B., Miller, L., Kozodoy, L., Chen, R.E., Carter, L., Walls, A.C., Park, Y.-J., et al. (2020). De novo design of picomolar SARS-CoV-2 miniprotein inhibitors. Science (1979) *370*, 426 LP – 431. https://doi.org/10.1126/science.abd9909.

Casar, B., Badrock, A.P., Jiménez, I., Arozarena, I., Colón-Bolea, P., Lorenzo-Martín, L.F., Barinaga-Rementería, I., Barriuso, J., Cappitelli, V., and Donoghue, D.J. (2018). RAS at the Golgi antagonizes malignant transformation through PTPRκ-mediated inhibition of ERK activation. Nat Commun *9*, 1–17.

Camara, A.K.S, Zhou, Y., Wen, P.C., Tajkhorshid, E., Kwok, W.M.. (2017). Mitochondrial VDAC1: A Key Gatekeeper as Potential Therapeutic Target. Front Physiol. *8*, 460.

Chiu, V.K., Bivona, T., Hach, A., Sajous, J.B., Silletti, J., Wiener, H., Johnson, R.L., Cox, A.D., and Philips, M.R. (2002). Ras signaling on the endoplasmic reticulum and the Golgi. Nat Cell Biol *4*, 343–350.

Cho, K.F., Branon, T.C., Rajeev, S., Svinkina, T., Udeshi, N.D., Thoudam, T., Kwak, C., Rhee, H.-W., Lee, I.-K., Carr, S.A., et al. (2020). Split-TurboID enables contact-dependent proximity labeling in cells. Proceedings of the National Academy of Sciences *117*, 12143 LP – 12154. https://doi.org/10.1073/pnas.1919528117.

Choi, Y.L., Soda, M., Yamashita, Y., Ueno, T., Takashima, J., Nakajima, T., Yatabe, Y., Takeuchi, K., Hamada, T., Haruta, H., et al. (2010) ALK Lung Cancer Study Group. EML4-ALK mutations in lung cancer that confer resistance to ALK inhibitors. N Engl J Med. *363*, 1734-9. doi: 10.1056/NEJMoa1007478.

Christensen, S.M., Tu, H.-L., Jun, J.E., Alvarez, S., Triplet, M.G., Iwig, J.S., Yadav, K.K., Bar-Sagi, D., Roose, J.P., and Groves, J.T. (2016). One-way membrane trafficking of SOS in receptor-triggered Ras activation. Nat Struct Mol Biol *23*, 838–846. https://doi.org/10.1038/nsmb.3275.

Cox, A.D., and Der, C.J. (2010). Ras history. Small GTPases *1*, 2–27. https://doi.org/10.4161/sgtp.1.1.12178.

Fernandez-Medarde, A., and Santos, E. (2011). Ras in cancer and developmental diseases. Genes Cancer *2*, 344–358. https://doi.org/10.1177/1947601911411084.

Fox, P.D., Haberkorn, C.J., Akin, E.J., Seel, P.J., Krapf, D., and Tamkun, M.M. (2015). Induction of stable ER–plasma-membrane junctions by Kv2.1 potassium channels. Journal of Cell Science *128*, 2096–2105. https://doi.org/10.1242/jcs.166009.

Fulton, D., Babbitt, R., Zoellner, S., Fontana, J., Acevedo, L., McCabe, T.J., Iwakiri, Y., and Sessa, W.C. (2004). Targeting of endothelial nitric-oxide synthase to the cytoplasmic face of the Golgi complex or plasma membrane regulates Akt- versus calcium-dependent mechanisms for nitric oxide release. J Biol Chem *279*, 30349–30357. https://doi.org/10.1074/jbc.M402155200.

Galli, S., Jahn, O., Hitt, R., Hesse, D., Opitz, L., Plessmann, U., Urlaub, H., Poderoso, J.J., Jares-Erijman, E.A., Jovin, T.M. (2009). A new paradigm for MAPK: structural interactions of hERK1 with mitochondria in HeLa cells. PLoS One. *4*, e7541.

Gao, X., and Zhang, J. (2008). Spatiotemporal analysis of differential Akt regulation in plasma membrane microdomains. Mol Biol Cell *19*, 4366–4373. https://doi.org/10.1091/mbc.e08-05-0449.
Gormand, A. (2010). The crosstalk between the ERK and the cAMP signalling pathways in PC12 Cells. Molecular Biology *12*, 258–266.
Greenwald, E.C., Mehta, S., and Zhang, J. (2018). Chemical Reviews *24*, 11707-11794. DOI: 10.1021/acs.chemrev.8b00333
Herrero, A., Casar, B., Colón-Bolea, P., Agudo-Ibáñez, L., and Crespo, P. (2016). Defined spatiotemporal features of RAS-ERK signals dictate cell fate in MCF-7 mammary epithelial cells. Mol Biol Cell *27*, 1958–1968.
Heslop, K.A., Milesi, V., and Maldonado E.N. (2021). VDAC Modulation of Cancer Metabolism: Advances and Therapeutic Challenges. Front. Physiol. *12*, 742839. doi: 10.3389/fphys.2021.742839
Huang, W.Y.C., Alvarez, S., Kondo, Y., Lee, Y.K., Chung, J.K., Lam, H.Y.M., Biswas, K.H., Kuriyan, J., and Groves, J.T. (2019). A molecular assembly phase transition and kinetic proofreading modulate Ras activation by SOS. Science *363*, 1098 LP – 1103. https://doi.org/10.1126/science.aau5721.
Hood, F.E., Sahraoui, Y.M., Jenkins, R.E., Prior, I.A. (2021). Ras protein abundance correlates with Ras isoform mutation patterns in cancer bioRxiv 2021.11.04.467300; doi: https://doi.org/10.1101/2021.11.04.467300
Iyer, D.N., Faruq, O., Zhang, L., Rastgoo, N., Liu, A., and Chang, H. (2021). Pathophysiological roles of myristoylated alanine-rich C-kinase substrate (MARCKS) in hematological malignancies. Biomarker Research *9*, 34. https://doi.org/10.1186/s40364-021-00286-9.
J, S.M., G, N.B., and Mitsuhiko, I. (2013). NMR-based functional profiling of RASopathies and oncogenic RAS mutations. Proceedings of the National Academy of Sciences *110*, 4574–4579. https://doi.org/10.1073/pnas.1218173110.
Keyes, J., Ganesan, A., Molinar-Inglis, O., Hamidzadeh, A., Zhang, J., Ling, M., Trejo, J., Levchenko, A., and Zhang, J. (2020). Signaling diversity enabled by Rap1-regulated plasma membrane ERK with distinct temporal dynamics. Elife *9*. https://doi.org/10.7554/eLife.57410.
Komatsu, N., Aoki, K., Yamada, M., Yukinaga, H., Fujita, Y., Kamioka, Y., and Matsuda, M. (2011). Development of an optimized backbone of FRET biosensors for kinases and GTPases. Mol Biol Cell *22*, 4647–4656. https://doi.org/10.1091/mbc.E11-01-0072.
Kwak, C., Shin, S., Park, J.-S., Jung, M., Nhung, T.T.M., Kang, M.-G., Lee, C., Kwon, T.-H., Park, S.K., and Mun, J.Y. (2020). Contact-ID, a tool for profiling organelle contact sites, reveals regulatory proteins of mitochondrial-associated membrane formation. Proceedings of the National Academy of Sciences *117*, 12109–12120.
Langan, R.A., Boyken, S.E., Ng, A.H., Samson, J.A., Dods, G., Westbrook, A.M., Nguyen, T.H., Lajoie, M.J., Chen, Z., and Berger, S. (2019). De novo design of bioactive protein switches. Nature *572*, 205–210.
Lanman, B.A., Allen, J.R., Allen, J.G., Amegadzie, A.K., Ashton, K.S., Booker, S.K., Chen, J.J., Chen, N., Frohn, M.J., Goodman, G., et al. (2019). J Med Chem *63*, 52-65.
Li, Y., Martin, L.D., Spizz, G., and Adler, K.B. (2001). MARCKS Protein Is a Key Molecule Regulating Mucin Secretion by Human Airway Epithelial Cells in Vitro*.

Journal of Biological Chemistry *276*, 40982–40990. https://doi.org/https://doi.org/10.1074/jbc.M105614200.

Li, Y.C., Lytle, N.K., Gammon, S.T., Wang, L., Hayes, T.K., Sutton, M.N., Bast Jr, R.C., Der, C.J., Piwnica-Worms, D., McCormick, F. and Wahl, G.M. (2020). Analysis of RAS protein interactions in living cells reveals a mechanism for pan-RAS depletion by membrane-targeted RAS binders. *Proceedings of the National Academy of Sciences*, *117*, 12121-12130.

Lynch, S.J., Snitkin, H., Gumper, I., Philips, M.R., Sabatini, D., and Pellicer, A. (2015). The differential palmitoylation states of N-Ras and H-Ras determine their distinct Golgi subcompartment localizations. J Cell Physiol *230*, 610–619.

Ma, Y., Taylor, S. (2002). A 15-residue bifunctional element in D-AKAP1 is required for both endoplasmic reticulum and mitochondrial targeting. J Biol Chem. *277*, 27328–27336. doi:10.1074/jbc.M201421200

Masibag, A.N., Bergin, C.J., Haebe, J.R., Zouggar, A., Shah, M.S., Sandouka, T., Mendes da Silva, A., Desrochers, F.M., Fournier-Morin, A., and Benoit, Y.D. (2021). Pharmacological targeting of Sam68 functions in colorectal cancer stem cells. IScience *24*, 103442. https://doi.org/https://doi.org/10.1016/j.isci.2021.103442.

Matallanas, D., Sanz-Moreno, V., Arozarena, I., Calvo, F., Agudo-Ibánez, L., Santos, E., Berciano, M.T., and Crespo, P. (2006). Distinct utilization of effectors and biological outcomes resulting from site-specific Ras activation: Ras functions in lipid rafts and Golgi complex are dispensable for proliferation and transformation. Mol Cell Biol *26*, 100–116.

Mochizuki, N., Yamashita, S., Kurokawa, K., Ohba, Y., Nagai, T., Miyawaki, A., and Matsuda, M. (2001). Spatio-temporal images of growth-factor-induced activation of Ras and Rap1. Nature *411*, 1065–1068. https://doi.org/10.1038/35082594.

Mohan, K., Ueda, G., Kim, A.R., Jude, K.M., Fallas, J.A., Guo, Y., Hafer, M., Miao, Y., Saxton, R.A., Piehler, J., et al. (2019). Topological control of cytokine receptor signaling induces differential effects in hematopoiesis. Science (1979) *364*, eaav7532. https://doi.org/10.1126/science.aav7532.

Muñoz-Maldonado, C., Zimmer, Y., and Medová, M. (2019). A Comparative Analysis of Individual RAS Mutations in Cancer Biology. Frontiers in Oncology *9*, 1088.

Najib, S., Martin-Romero, C., Gonzalez-Yanes, C., and Sanchez-Margalet, V. (2005). Role of Sam68 as an adaptor protein in signal transduction. Cellular and Molecular Life Sciences CMLS *62*, 36–43.

Nelson, B.H. (2004). IL-2, Regulatory T Cells, and Tolerance. The Journal of Immunology *172*, 3983. https://doi.org/10.4049/jimmunol.172.7.3983.

Ng, A.H., Nguyen, T.H., Gomez-Schiavon, M., Dods, G., Langan, R.A., Boyken, S.E., Samson, J.A., Waldburger, L.M., Dueber, J.E., and Baker, D. (2019). Modular and tunable biological feedback control using a de novo protein switch. Nature *572*, 265–269.

O'Shaughnessy, E.C., Stone, O.J., LaFosse, P.K., Azoitei, M.L., Tsygankov, D., Heddleston, J.M., Legant, W.R., Wittchen, E.S., Burridge, K., Elston, T.C., et al. (2019). Software for lattice light-sheet imaging of FRET biosensors, illustrated with a new Rap1 biosensor. Journal of Cell Biology *218*, 3153–3160. https://doi.org/10.1083/jcb.201903019.

Ostrem, J.M., Peters, U., Sos, M.L., Wells, J.A., and Shokat, K.M. (2013). K-Ras(G12C) inhibitors allosterically control GTP affinity and effector interactions. Nature *503*, 548–551. https://doi.org/10.1038/nature12796.

Posch, C., Sanlorenzo, M., Vujic, I., Oses-Prieto, J.A., Cholewa, B.D., Kim, S.T., Ma, J., Lai, K., Zekhtser, M., and Esteve-Puig, R. (2016). Phosphoproteomic analyses of NRAS (G12) and NRAS (Q61) mutant melanocytes reveal increased CK2α kinase levels in NRAS (Q61) mutant cells. Journal of Investigative Dermatology *136*, 2041–2048. .

Quatela, S.E., and Philips, M.R. (2006). Ras signaling on the Golgi. Curr Opin Cell Biol *18*, 162–167. https://doi.org/10.1016/j.ceb.2006.02.004.

Quijano-Rubio, A., Yeh, H.-W., Park, J., Lee, H., Langan, R.A., Boyken, S.E., Lajoie, M.J., Cao, L., Chow, C.M., Miranda, M.C., et al. (2021). De novo design of modular and tunable protein biosensors. Nature https://doi.org/10.1038/s41586-021-03258-z.

Rocks, O., Peyker, A., Kahms, M., Verveer, P.J., Koerner, C., Lumbierres, M., Kuhlmann, J., Waldmann, H., Wittinghofer, A., and Bastiaens, P.I.H. (2005). An acylation cycle regulates localization and activity of palmitoylated Ras isoforms. Science (1979) *307*, 1746–1752.

Rose, J.C., Huang, P.-S., Camp, N.D., Ye, J., Leidal, A.M., Goreshnik, I., Trevillian, B.M., Dickinson, M.S., Cunningham-Bryant, D., Debnath, J., et al. (2017a). A computationally engineered RAS rheostat reveals RAS-ERK signaling dynamics. Nat Chem Biol *13*, 119–126. https://doi.org/10.1038/nchembio.2244.

Rose, J.C., Huang, P.-S., Camp, N.D., Ye, J., Leidal, A.M., Goreshnik, I., Trevillian, B.M., Dickinson, M.S., Cunningham-Bryant, D., Debnath, J., et al. (2017b). A computationally engineered RAS rheostat reveals RAS-ERK signaling dynamics. Nat Chem Biol *13*, 119–126. https://doi.org/10.1038/nchembio.2244.

Rose, J.C., Dieter, E.M., Cunningham-Bryant, D., and Maly, D.J. (2020). "Examining RAS pathway rewiring with a chemically inducible activator of RAS". Small GTPases *11*, 413–420. https://doi.org/10.1080/21541248.2018.1446697.

Roux, K.J., Kim, D.I., Burke, B., and May, D.G. (2018). BioID: A Screen for Protein-Protein Interactions. Curr Protoc Protein Sci *91*, 19.23.1-19.23.15. https://doi.org/10.1002/cpps.51.

Ryan, M.B., Fece de la Cruz, F., Phat, S., Myers, D.T., Wong, E., Shahzade, H.A., Hong, C.B., and Corcoran, R.B. (2020). Vertical Pathway Inhibition Overcomes Adaptive Feedback Resistance to KRAS(G12C) Inhibition. Clin Cancer Res *26*, 1633–1643. https://doi.org/10.1158/1078-0432.CCR-19-3523.

Sabir, S.R., Yeoh, S., Jackson, G., and Bayliss, R. (2017). EML4-ALK Variants: Biological and Molecular Properties, and the Implications for Patients. Cancers (Basel) *9*. https://doi.org/10.3390/cancers9090118.

Sampson, J., Richards, M.W., Choi, J., Fry, A.M., and Bayliss, R. (2021). Phase-separated foci of EML4-ALK facilitate signaling and depend upon an active kinase conformation. EMBO Rep *22*, e53693.

Santana-Codina, N., Chandhoke, A.S., Yu, Q., Małachowska, B., Kuljanin, M., Gikandi, A., Stańczak, M., Gableske, S., Jedrychowski, M.P., Scott, D.A., et al. (2020). Defining and Targeting Adaptations to Oncogenic KRASG12C Inhibition Using Quantitative Temporal Proteomics. Cell Rep. *30*, 4584-4599.e4.

Santra, T., Herrero, A., Rodriguez, J., Von Kriegsheim, A., Iglesias-Martinez, L.F., Schwarzl, T., Higgins, D., Aye, T.-T., Heck, A.J.R., and Calvo, F. (2019). An integrated global analysis of compartmentalized HRAS signaling. Cell Rep *26*, 3100–3115. .

Satoh, A., Hayashi-Nishino, M., Shakuno, T., Masuda, J., Koreishi, M., Murakami, R., Nakamura, Y., Nakamura, T., Abe-Kanoh, N., Honjo, Y., et al. (2019). The Golgin Protein Giantin Regulates Interconnections Between Golgi Stacks. Frontiers in Cell and Developmental Biology *7*.

Schaub, B.E., Berger, B., Berger, E.G., and Rohrer, J. (2006). Transition of galactosyltransferase 1 from trans-Golgi cisterna to the trans-Golgi network is signal mediated. Mol Biol Cell *17*, 5153–5162. https://doi.org/10.1091/mbc.e06-08-0665.

Schmick, M., Kraemer, A., and Bastiaens, P.I.H. (2015). Ras moves to stay in place. Trends Cell Biol *25*, 190–197.

Scrima, A., Thomas, C., Deaconescu, D., and Wittinghofer, A. (2008). The Rap-RapGAP complex: GTP hydrolysis without catalytic glutamine and arginine residues. EMBO J *27*, 1145–1153. https://doi.org/10.1038/emboj.2008.30.

Shoshan-Barmatz, V., Zalk, R., Gincel, D. and Vardi, N. (2004). Subcellular localization of VDAC in mitochondria and ER in the cerebellum. Biochimica et Biophysica Acta (BBA)-Bioenergetics *1657*, 105-114.

Silva, D.-A., Yu, S., Ulge, U.Y., Spangler, J.B., Jude, K.M., Labão-Almeida, C., Ali, L.R., Quijano-Rubio, A., Ruterbusch, M., Leung, I., et al. (2019). De novo design of potent and selective mimics of IL-2 and IL-15. Nature *565*, 186–191. https://doi.org/10.1038/s41586-018-0830-7.

Su, X., Ditlev, J.A., Hui, E., Xing, W., Banjade, S., Okrut, J., King, D.S., Taunton, J., Rosen, M.K., and Vale, R.D. (2016). Phase separation of signaling molecules promotes T cell receptor signal transduction. Science *352*, 595–599. https://doi.org/10.1126/science.aad9964.

Szczesna-Skorupa, E., and Kemper, B. (2000). Endoplasmic reticulum retention determinants in the transmembrane and linker domains of cytochrome P450 2C1. J Biol Chem *275*, 19409–19415. https://doi.org/10.1074/jbc.M002394200.

Tantama, M., Martínez-François, J.R., Mongeon, R., Yellen, G. (2013). Imaging energy status in live cells with a fluorescent biosensor of the intracellular ATP-to-ADP ratio. Nat Commun. *4*, 2550.

Tenner, B., Zhang, J.Z., Huang, B., Mehta, S., and Zhang, J. (2021). FluoSTEPs: Fluorescent biosensors for monitoring compartmentalized signaling within endogenous microdomains. Sci Adv *7*, eabe4091.

Tran, T.H., Chan, A.H., Young, L.C., Bindu, L., Neale, C., Messing, S., Dharmaiah, S., Taylor, T., Denson, J.-P., Esposito, D., et al. (2021). KRAS interaction with RAF1 RAS-binding domain and cysteine-rich domain provides insights into RAS-mediated RAF activation. Nature Communications *12*, 1176. https://doi.org/10.1038/s41467-021-21422-x.

Tulpule, A., Guan, J., Neel, D.S., Allegakoen, H.R., Lin, Y.P., Brown, D., Chou, Y.-T., Heslin, A., Chatterjee, N., Perati, S., et al. (2021). Kinase-mediated RAS signaling via membraneless cytoplasmic protein granules. Cell *184*, 2649-2664.e18.

Uozumi, T., Hamakawa, M., Deno, Y.K., Nakajo, N., Hirotsu, T. (2015), Voltage-dependent anion channel (VDAC-1) is required for olfactory sensing in *Caenorhabditis elegans*. Genes Cells. *20*, 802-816.

Werley, C.A., Boccardo, S., Rigamonti, A., Hansson, E.M., Cohen, A.E. (2020). Multiplexed Optical Sensors in Arrayed Islands of Cells for multimodal recordings of cellular physiology. Nat Commun. *11*, 3881.

Xiong, Z., Lo, H.P., McMahon, K.-A., Martel, N., Jones, A., Hill, M.M., Parton, R.G., and Hall, T.E. (2021). In vivo proteomic mapping through GFP-directed proximity-dependent biotin labelling in zebrafish. Elife *10*, e64631. https://doi.org/10.7554/eLife.64631.

Xue, J.Y., Zhao, Y., Aronowitz, J., Mai, T.T., Vides, A., Qeriqi, B., Kim, D., Li, C., de Stanchina, E., Mazutis, L., et al. (2020). Rapid non-uniform adaptation to conformation-specific KRAS(G12C) inhibition. Nature *577*, 421–425. https://doi.org/10.1038/s41586-019-1884-x.

Zhang, J.Z., Lu, T.-W., Stolerman, L.M., Tenner, B., Yang, J., Zhang, J.-F., Falcke, M., Rangamani, P., Taylor, S.S., Mehta, S., et al. (2020a). Phase separation of a PKA regulatory subunit controls cAMP compartmentation and oncogenic signaling. Cell *182*, 1531-1544.e15.

Zhang, J.Z., Nguyen, A.H., Miyamoto, S., Brown, J.H., McCulloch, A.D., and Zhang, J. (2020b). Histamine-induced biphasic activation of RhoA allows for persistent RhoA signaling. PLOS Biology *18*, e3000866.

Zhang, J.Z., Mehta, S., and Zhang, J. (2021). Liquid–liquid phase separation: a principal organizer of the cell's biochemical activity architecture. Trends in Pharmacological Sciences *42*, 845–856. https://doi.org/https://doi.org/10.1016/j.tips.2021.07.003.

Zhang, J.Z., Yeh, H.-W., Walls, A.C., Wicky, B.I.M., Sprouse, K.R., VanBlargan, L.A., Treger, R., Quijano-Rubio, A., Pham, M.N., Kraft, J.C., et al. (2022). Thermodynamically coupled biosensors for detecting neutralizing antibodies against SARS-CoV-2 variants. Nature Biotechnology *40*, 1336-1340. https://doi.org/10.1038/s41587-022-01280-8.

Zhang, Z., Morstein, J., Ecker, A.K., Guiley, K.Z., and Shokat, K.M. (2022). Chemoselective Covalent Modification of K-Ras(G12R) with a Small Molecule Electrophile. JACS *144*, 15916-15921.

Zhang, Z., Guiley, K.Z., and Shokat, K.M. (2022) Chemical acylation of an acquired serine suppresses oncogenic signaling of K-Ras(G12S). Nat Chem Biol (2022). https://doi.org/10.1038/s41589-022-01065-9

Fig 1

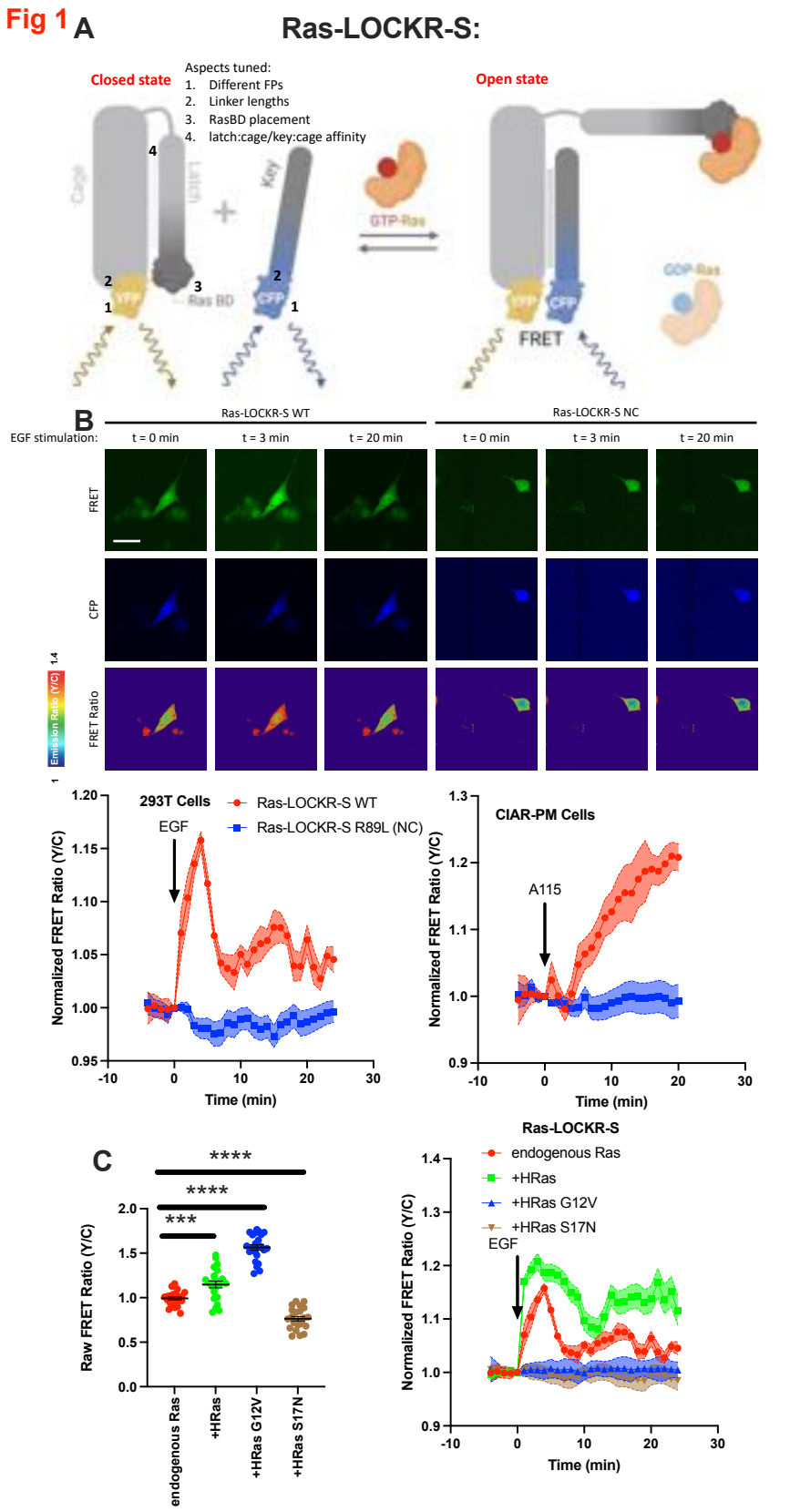
A
Ras-LOCKR-S:
Closed state
Aspects tuned:
1. Different FPs
2. Linker lengths
3. RasBD placement
4. latch:cage/key:cage affinity
Open state
Cage
Linker
Key
GTP-Ras
GDP-Ras
Ras BD
YFP
CFP
FRET
B
Ras-LOCKR-S WT
Ras-LOCKR-S NC
EGF stimulation:
t = 0 min
t = 3 min
t = 20 min
FRET
CFP
FRET Ratio
Emission Ratio (Y/C)
293T Cells
Ras-LOCKR-S WT
Ras-LOCKR-S R89L (NC)
EGF
Normalized FRET Ratio (Y/C)
Time (min)
CIAR-PM Cells
A115
C
Raw FRET Ratio (Y/C)
endogenous Ras
+HRas
+HRas G12V
+HRas S17N
Ras-LOCKR-S
EGF

A

Localized Ras sensor (Ras-LOCKR-S) and Ras activator (CIAR):

Fig 2

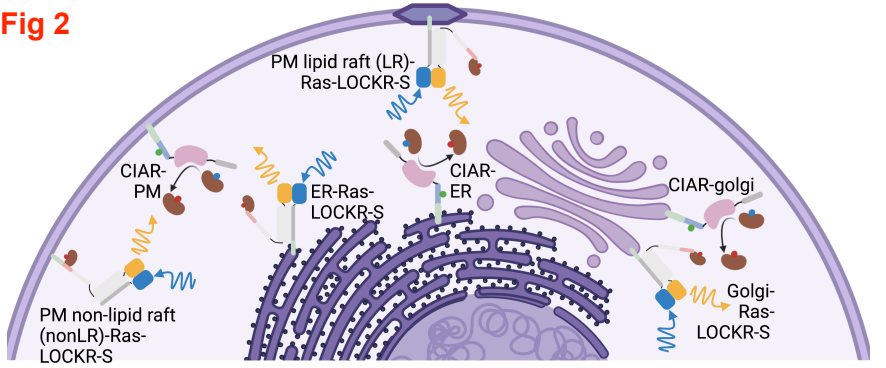

293T Cells

B

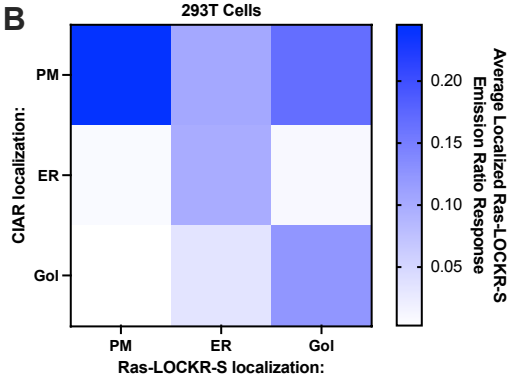

C

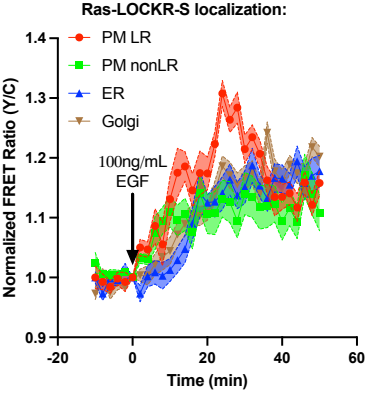

Jurkat T-Cells

D

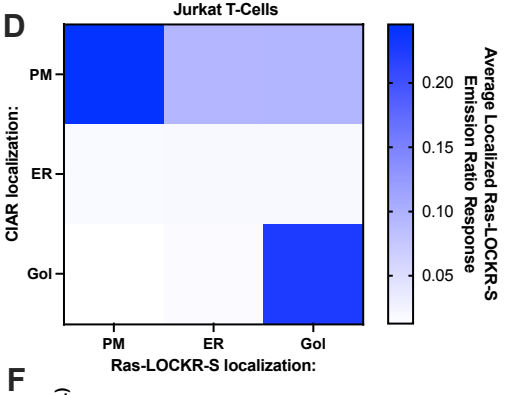

E

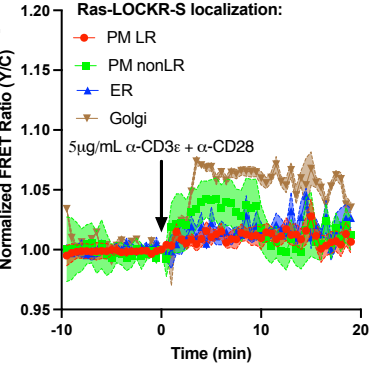

F

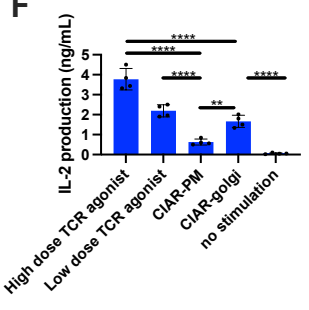

Fig 3

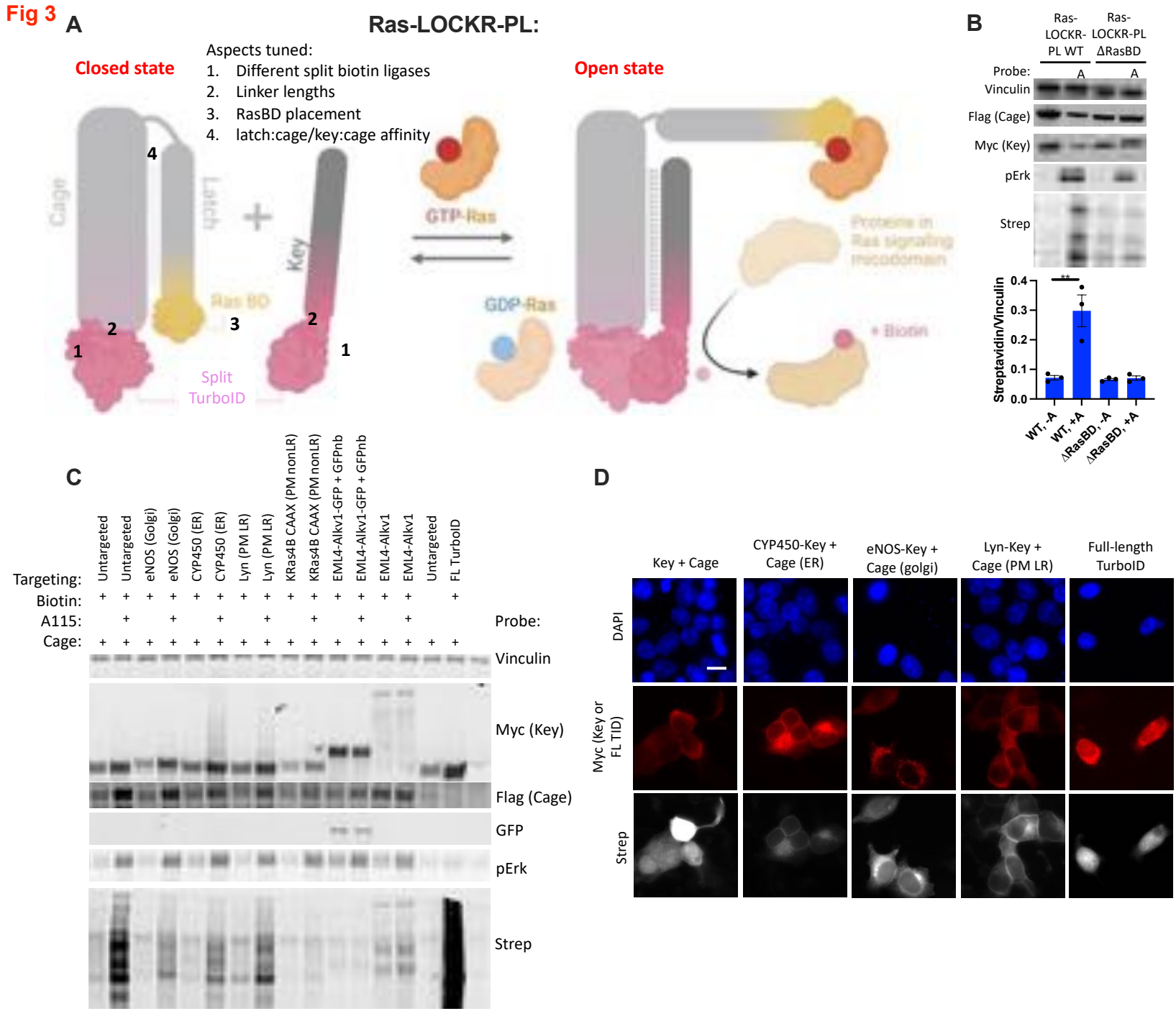
A
Ras-LOCKR-PL:
Aspects tuned:
1. Different split biotin ligases
2. Linker lengths
3. RasBD placement
4. latch:cage/key:cage affinity
Closed state
Open state
Cage
Linker
Key
Ras BD
Split TurboID
GTP-Ras
GDP-Ras
+ Biotin
B
Ras-LOCKR-PL WT
Ras-LOCKR-PL ΔRasBD
Probe:
A
Vinculin
Flag (Cage)
Myc (Key)
pErk
Strep
Streptavidin/Vinculin
WT, -A
WT, +A
ΔRasBD, -A
ΔRasBD, +A
C
Targeting:
Biotin:
A115:
Cage:
Untargeted
eNOS (Golgi)
CYP450 (ER)
Lyn (PM LR)
KRas4B CAAX (PM nonLR)
EML4-Alkv1-GFP + GFPnb
EML4-Alkv1
FL TurboID
Probe:
Vinculin
Myc (Key)
Flag (Cage)
GFP
pErk
Strep
D
Key + Cage
CYP450-Key + Cage (ER)
eNOS-Key + Cage (golgi)
Lyn-Key + Cage (PM LR)
Full-length TurboID
DAPI
Myc (Key or FL TID)
Strep

Fig 4

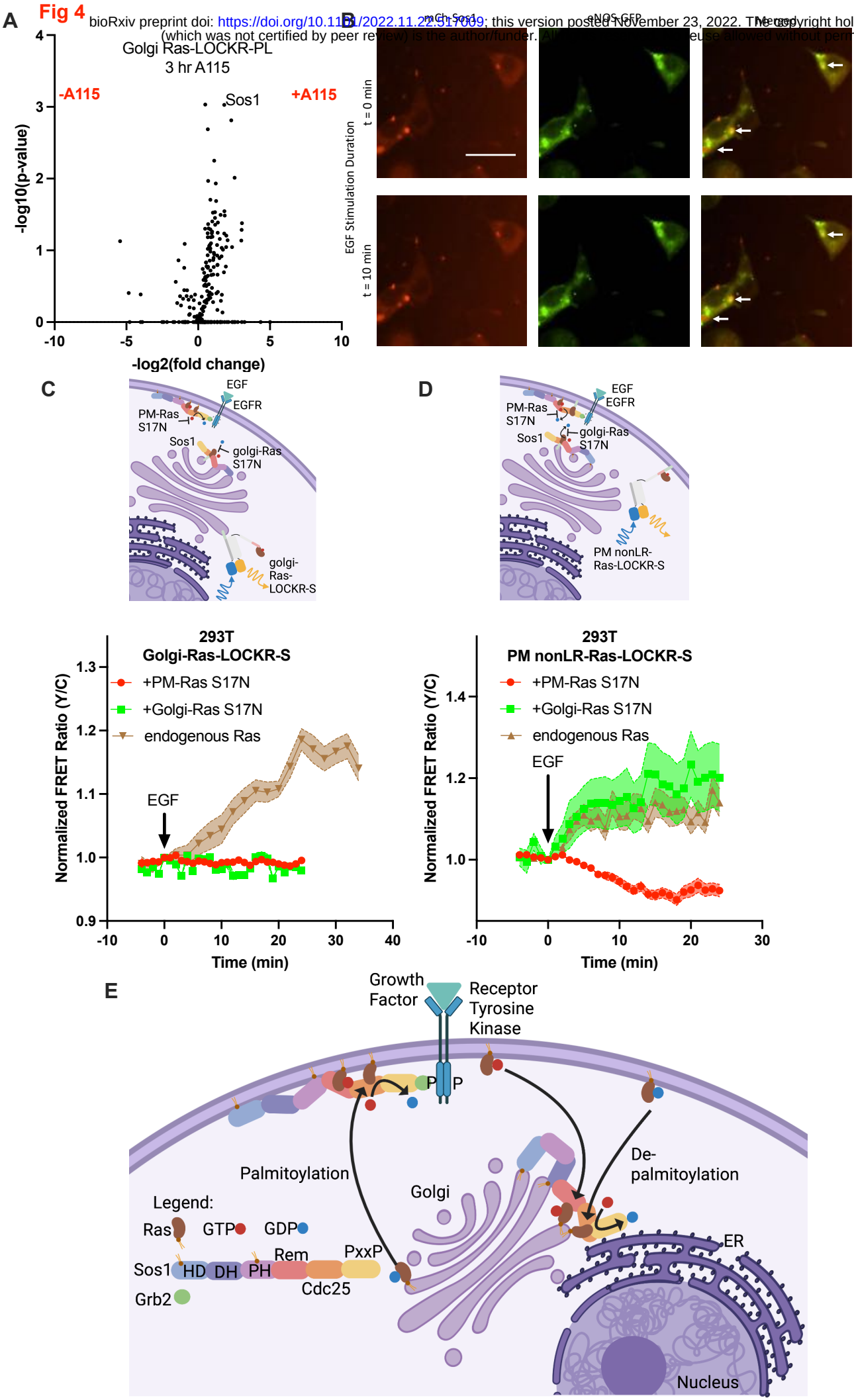

Fig 5

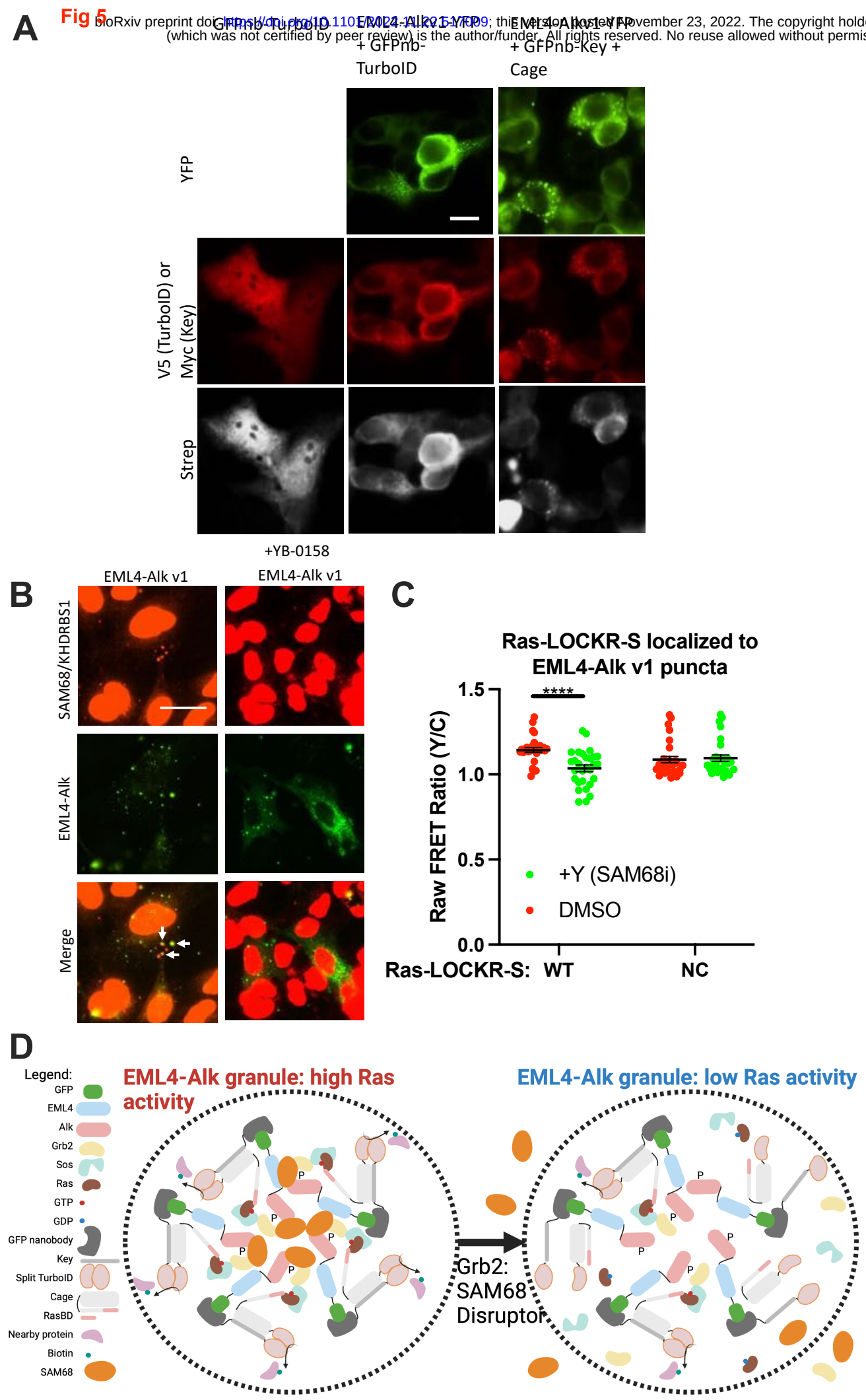

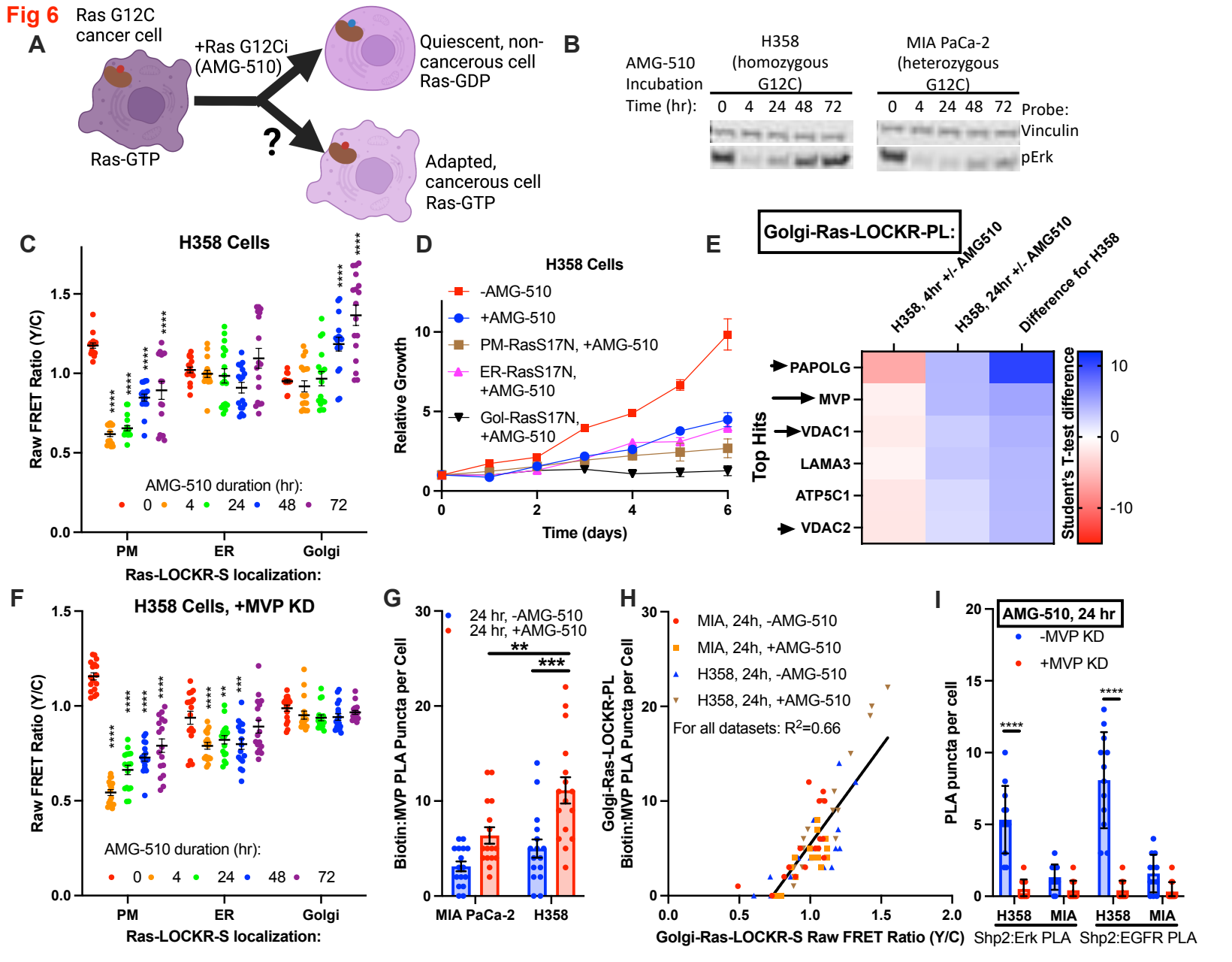
Fig 6
A
Ras G12C cancer cell
+Ras G12Ci (AMG-510)
Quiescent, non-cancerous cell Ras-GDP
Ras-GTP
?
Adapted, cancerous cell Ras-GTP
B
AMG-510 Incubation Time (hr):
H358 (homozygous G12C)
MIA PaCa-2 (heterozygous G12C)
0 4 24 48 72
Probe:
Vinculin
pErk
C
H358 Cells
Raw FRET Ratio (Y/C)
AMG-510 duration (hr):
0 4 24 48 72
PM ER Golgi
Ras-LOCKR-S localization:
D
H358 Cells
-AMG-510
+AMG-510
PM-RasS17N, +AMG-510
ER-RasS17N, +AMG-510
Gol-RasS17N, +AMG-510
Relative Growth
Time (days)
E
Golgi-Ras-LOCKR-PL:
H358, 4hr +/- AMG510
H358, 24hr +/- AMG510
Difference for H358
Top Hits
PAPOLG
MVP
VDAC1
LAMA3
ATP5C1
VDAC2
Student's T-test difference
F
H358 Cells, +MVP KD
Raw FRET Ratio (Y/C)
AMG-510 duration (hr):
0 4 24 48 72
PM ER Golgi
Ras-LOCKR-S localization:
G
24 hr, -AMG-510
24 hr, +AMG-510
Biotin:MVP PLA Puncta per Cell
MIA PaCa-2 H358
H
MIA, 24h, -AMG-510
MIA, 24h, +AMG-510
H358, 24h, -AMG-510
H358, 24h, +AMG-510
For all datasets: R^2=0.66
Golgi-Ras-LOCKR-PL Biotin:MVP PLA Puncta per Cell
Golgi-Ras-LOCKR-S Raw FRET Ratio (Y/C)
I
AMG-510, 24 hr
-MVP KD
+MVP KD
PLA puncta per cell
H358 MIA H358 MIA
Shp2:Erk PLA Shp2:EGFR PLA

Fig 7

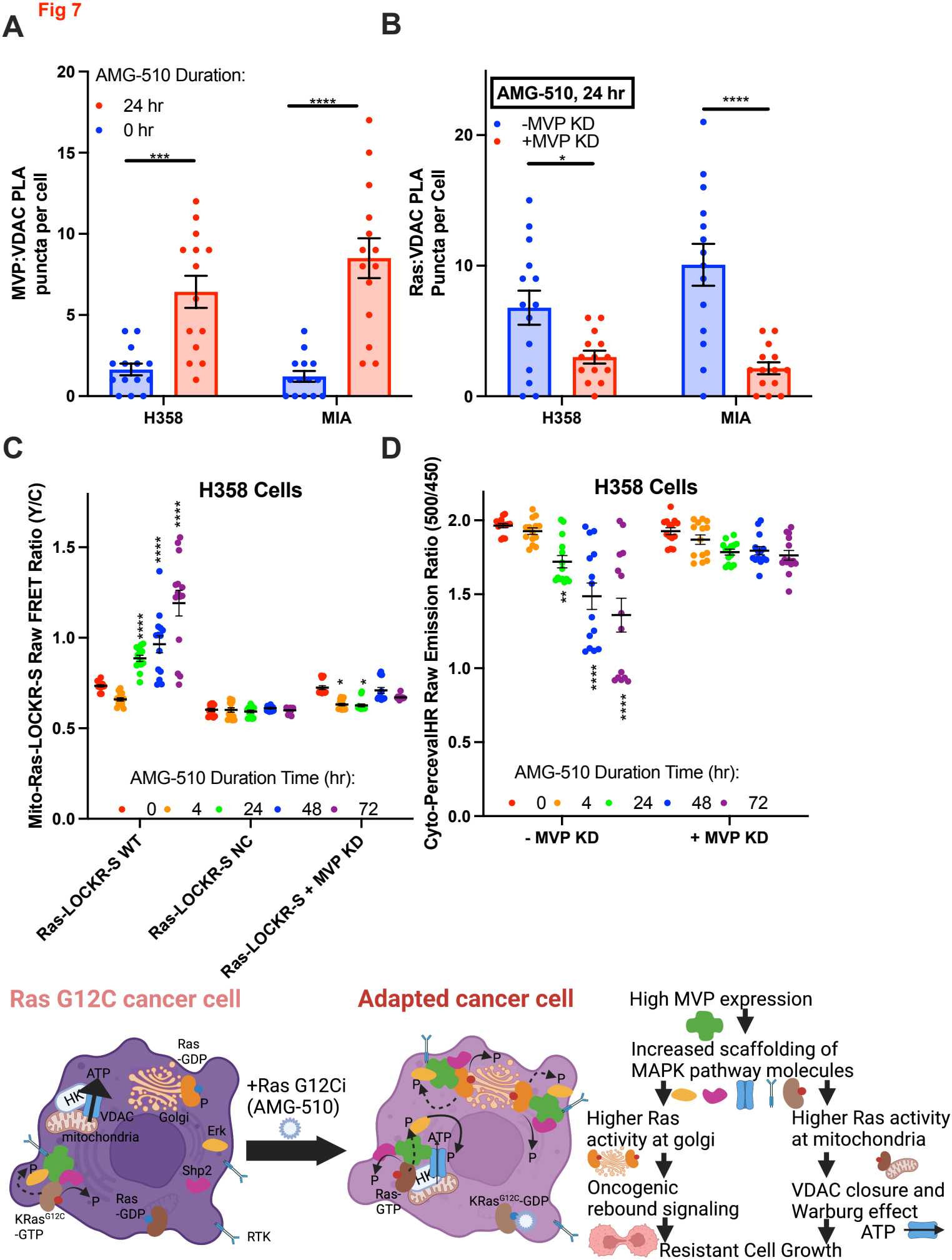
A
AMG-510 Duration:
24 hr
0 hr
MVP:VDAC PLA puncta per cell
H358
MIA
B
AMG-510, 24 hr
-MVP KD
+MVP KD
Ras:VDAC PLA Puncta per Cell
C
H358 Cells
Mito-Ras-LOCKR-S Raw FRET Ratio (Y/C)
AMG-510 Duration Time (hr):
Ras-LOCKR-S WT
Ras-LOCKR-S NC
Ras-LOCKR-S + MVP KD
D
H358 Cells
Cyto-PercevalHR Raw Emission Ratio (500/450)
- MVP KD
+ MVP KD
E
Ras G12C cancer cell
Adapted cancer cell
+Ras G12Ci (AMG-510)
High MVP expression
Increased scaffolding of MAPK pathway molecules
Higher Ras activity at golgi
Higher Ras activity at mitochondria
Oncogenic rebound signaling
VDAC closure and Warburg effect
ATP
Resistant Cell Growth
RTK

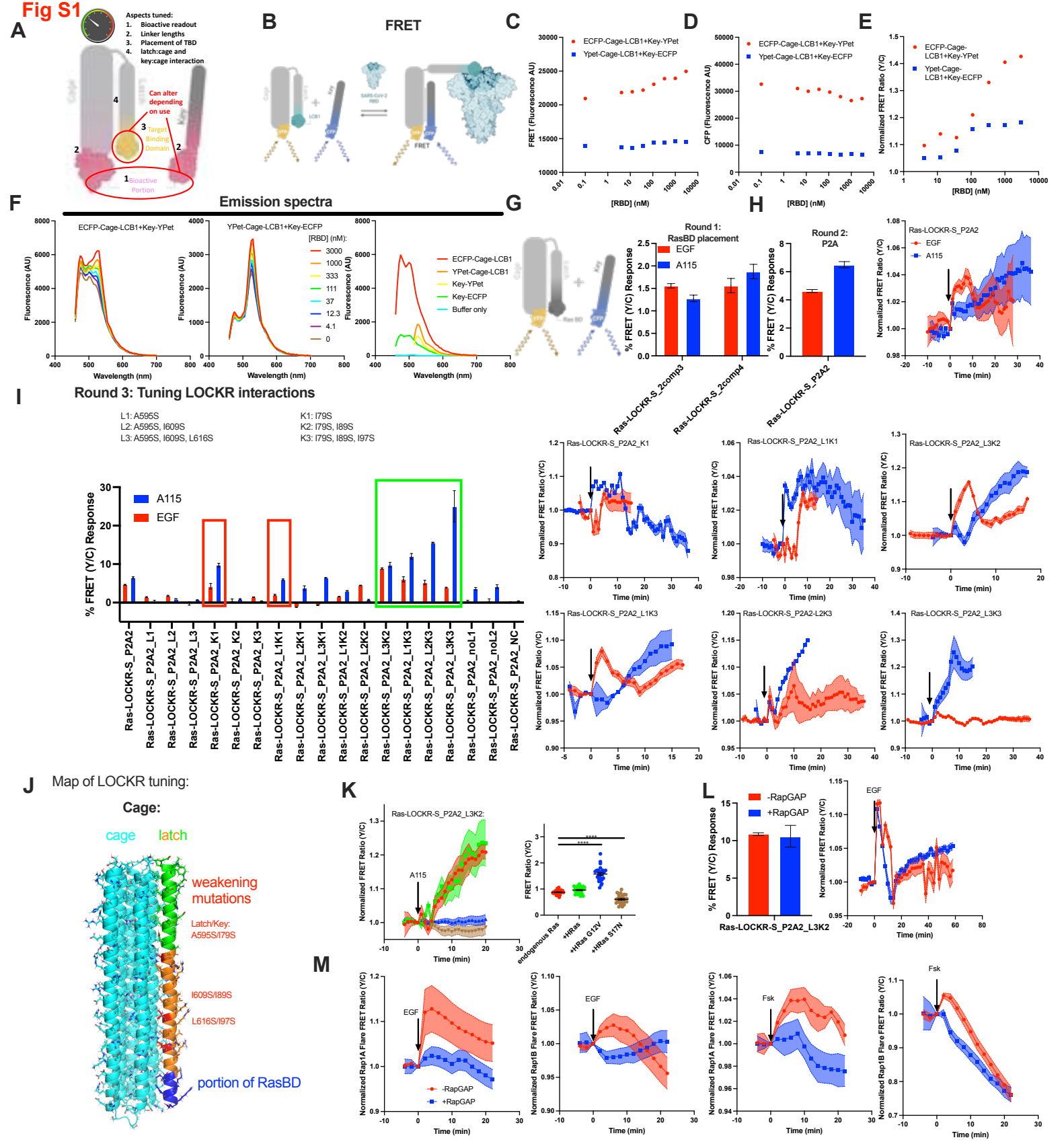
Fig S1
A
Aspects tuned:
1. Bioactive readout
2. Linker lengths
3. Placement of TBD
4. latch:cage and key:cage interaction
Can alter depending on use
Target Binding Domain
Bioactive Portion
B
FRET
C
ECFP-Cage-LCB1+Key-YPet
Ypet-Cage-LCB1+Key-ECFP
FRET (Fluorescence AU)
[RBD] (nM)
D
CFP (Fluorescence AU)
E
Normalized FRET Ratio (Y/C)
F
Emission spectra
Fluorescence (AU)
Wavelength (nm)
[RBD] (nM):
3000
1000
333
111
37
12.3
4.1
0
ECFP-Cage-LCB1
YPet-Cage-LCB1
Key-YPet
Key-ECFP
Buffer only
G
H
Round 1:
RasBD placement
EGF
A115
% FRET (Y/C) Response
Round 2:
P2A
Ras-LOCKR-S_2comp3
Ras-LOCKR-S_2comp4
Ras-LOCKR-S_P2A2
Time (min)
I
Round 3: Tuning LOCKR interactions
L1: A595S
L2: A595S, I609S
L3: A595S, I609S, L616S
K1: I79S
K2: I79S, I89S
K3: I79S, I89S, I97S
Ras-LOCKR-S_P2A2
Ras-LOCKR-S_P2A2_L1
Ras-LOCKR-S_P2A2_L2
Ras-LOCKR-S_P2A2_L3
Ras-LOCKR-S_P2A2_K1
Ras-LOCKR-S_P2A2_K2
Ras-LOCKR-S_P2A2_K3
Ras-LOCKR-S_P2A2_L1K1
Ras-LOCKR-S_P2A2_L2K1
Ras-LOCKR-S_P2A2_L3K1
Ras-LOCKR-S_P2A2_L1K2
Ras-LOCKR-S_P2A2_L2K2
Ras-LOCKR-S_P2A2_L3K2
Ras-LOCKR-S_P2A2_L1K3
Ras-LOCKR-S_P2A2_L2K3
Ras-LOCKR-S_P2A2_L3K3
Ras-LOCKR-S_P2A2_noL1
Ras-LOCKR-S_P2A2_noL2
Ras-LOCKR-S_P2A2_NC
J
Map of LOCKR tuning:
Cage:
cage
latch
weakening mutations
Latch/Key: A595S/I79S
I609S/I89S
L616S/I97S
portion of RasBD
K
Ras-LOCKR-S_P2A2_L3K2:
A115
FRET Ratio (Y/C)
endogenous Ras
+HRas
+HRas G12V
+HRas S17N
L
-RapGAP
+RapGAP
Ras-LOCKR-S_P2A2_L3K2
M
Normalized Rap1A Flare FRET Ratio (Y/C)
Normalized Rap1B Flare FRET Ratio (Y/C)
EGF
Fsk

Fig S2

293T cells

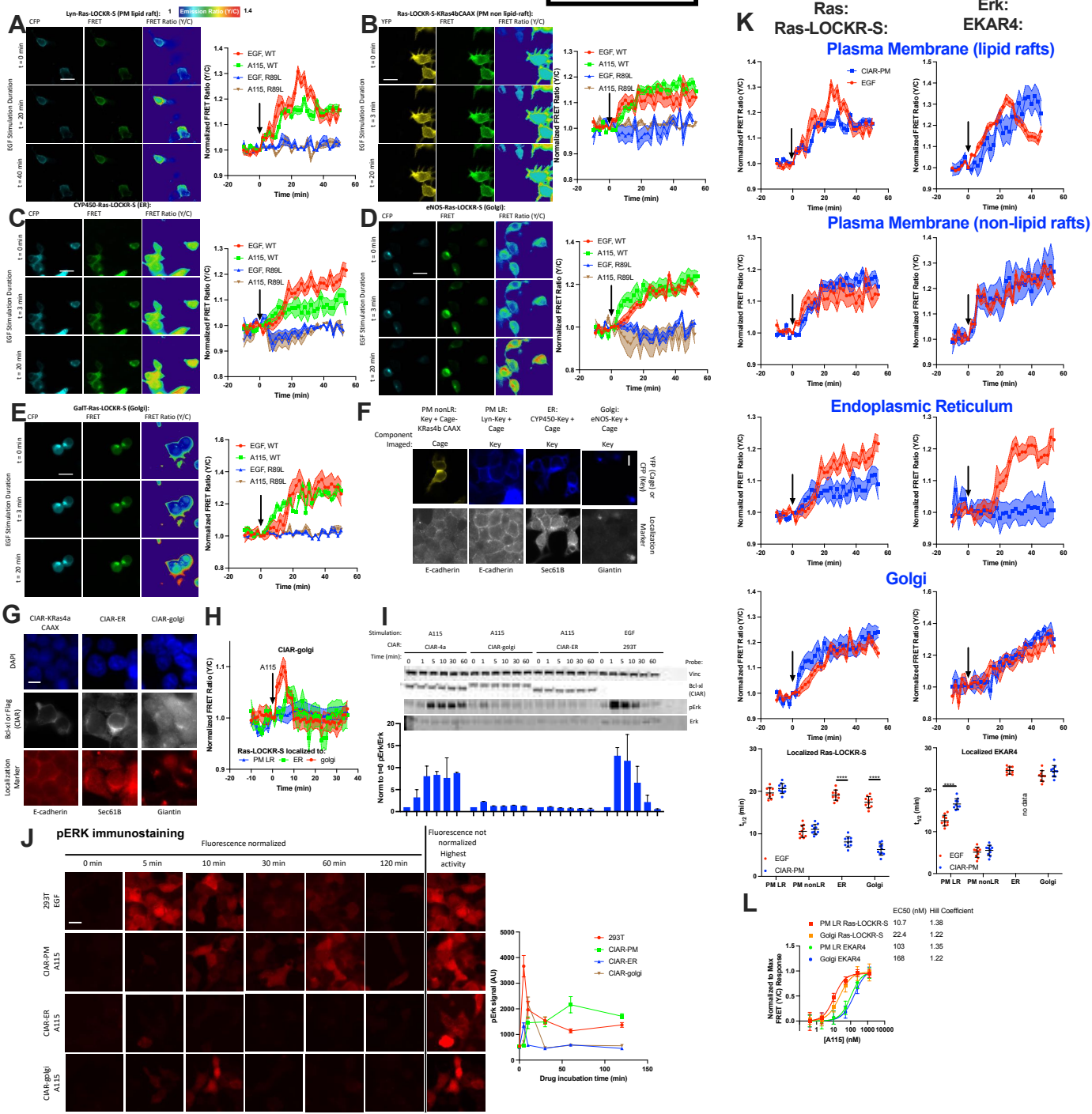

Fig S3

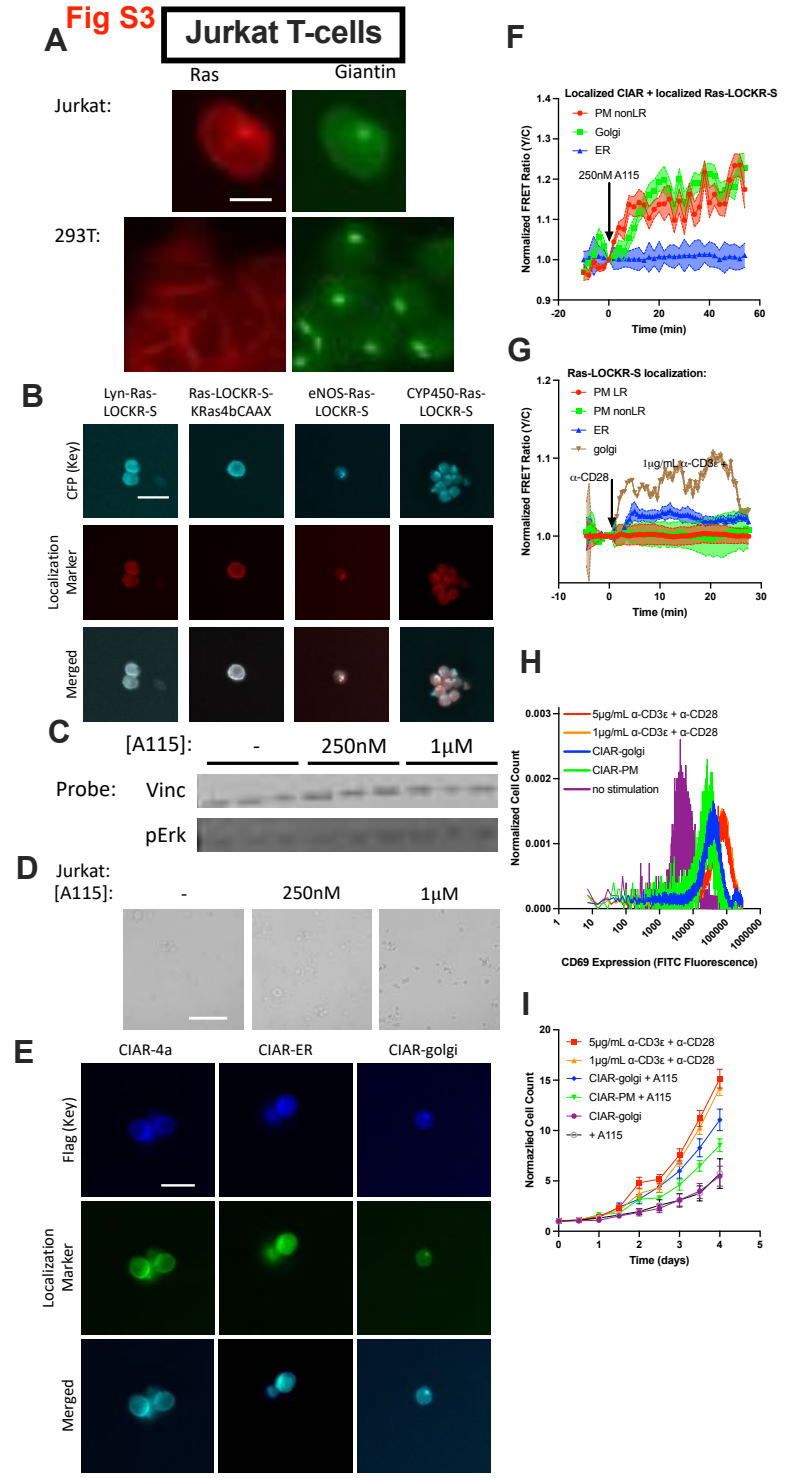
A
Jurkat T-cells
Ras
Giantin
Jurkat:
293T:
B
Lyn-Ras-LOCKR-S
Ras-LOCKR-S-KRas4bCAAX
eNOS-Ras-LOCKR-S
CYP450-Ras-LOCKR-S
CFP (Key)
Localization Marker
Merged
C
[A115]:
-
250nM
1μM
Probe:
Vinc
pErk
D
Jurkat:
[A115]:
-
250nM
1μM
E
CIAR-4a
CIAR-ER
CIAR-golgi
Flag (Key)
Localization Marker
Merged
F
Localized CIAR + localized Ras-LOCKR-S
PM nonLR
Golgi
ER
250nM A115
Normalized FRET Ratio (Y/C)
Time (min)
G
Ras-LOCKR-S localization:
PM LR
PM nonLR
ER
golgi
α-CD28
1μg/mL α-CD3ε +
Normalized FRET Ratio (Y/C)
Time (min)
H
5μg/mL α-CD3ε + α-CD28
1μg/mL α-CD3ε + α-CD28
CIAR-golgi
CIAR-PM
no stimulation
Normalized Cell Count
CD69 Expression (FITC Fluorescence)
I
5μg/mL α-CD3ε + α-CD28
1μg/mL α-CD3ε + α-CD28
CIAR-golgi + A115
CIAR-PM + A115
CIAR-golgi
+ A115
Normalized Cell Count
Time (days)

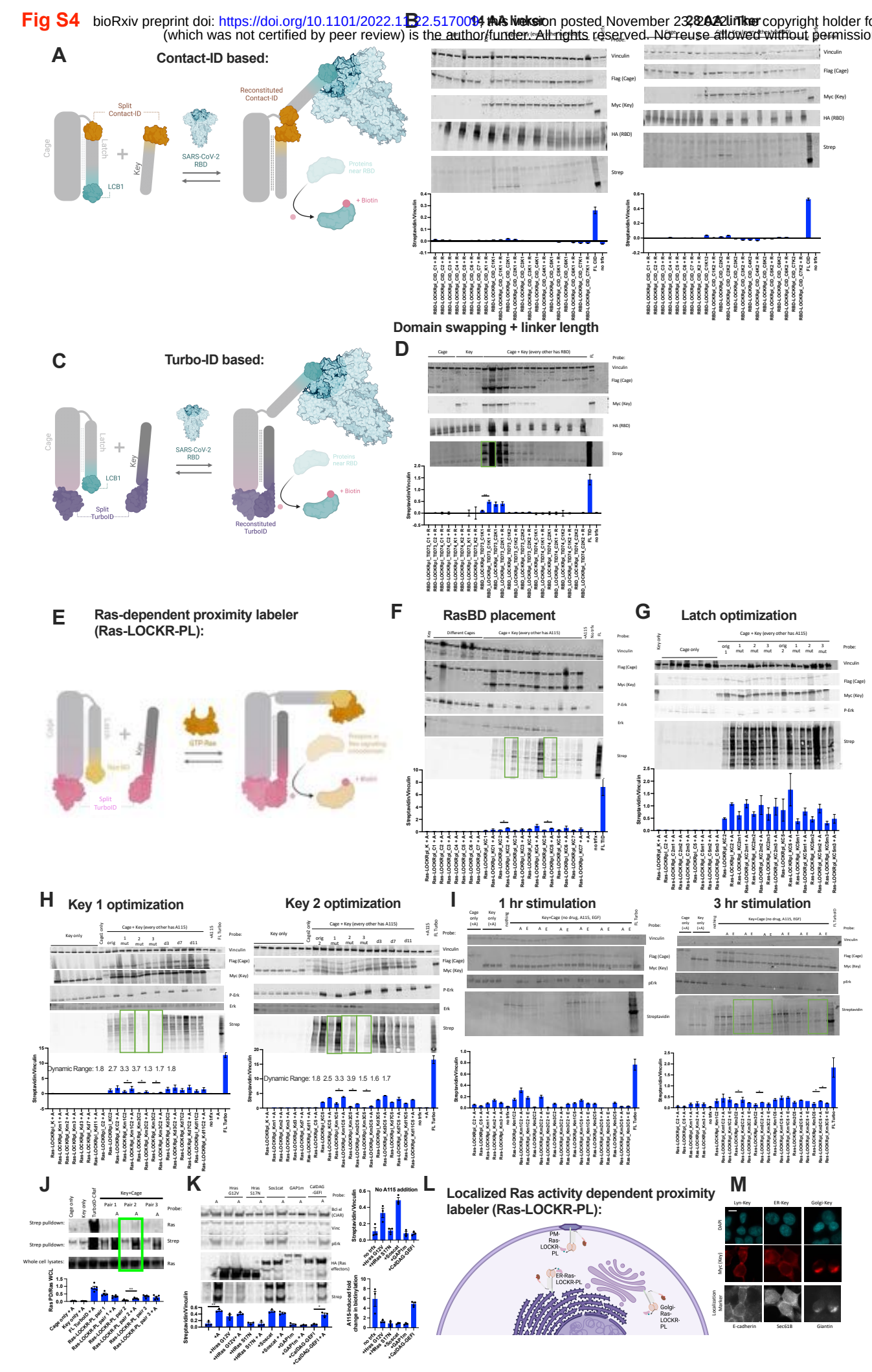

Fig S5

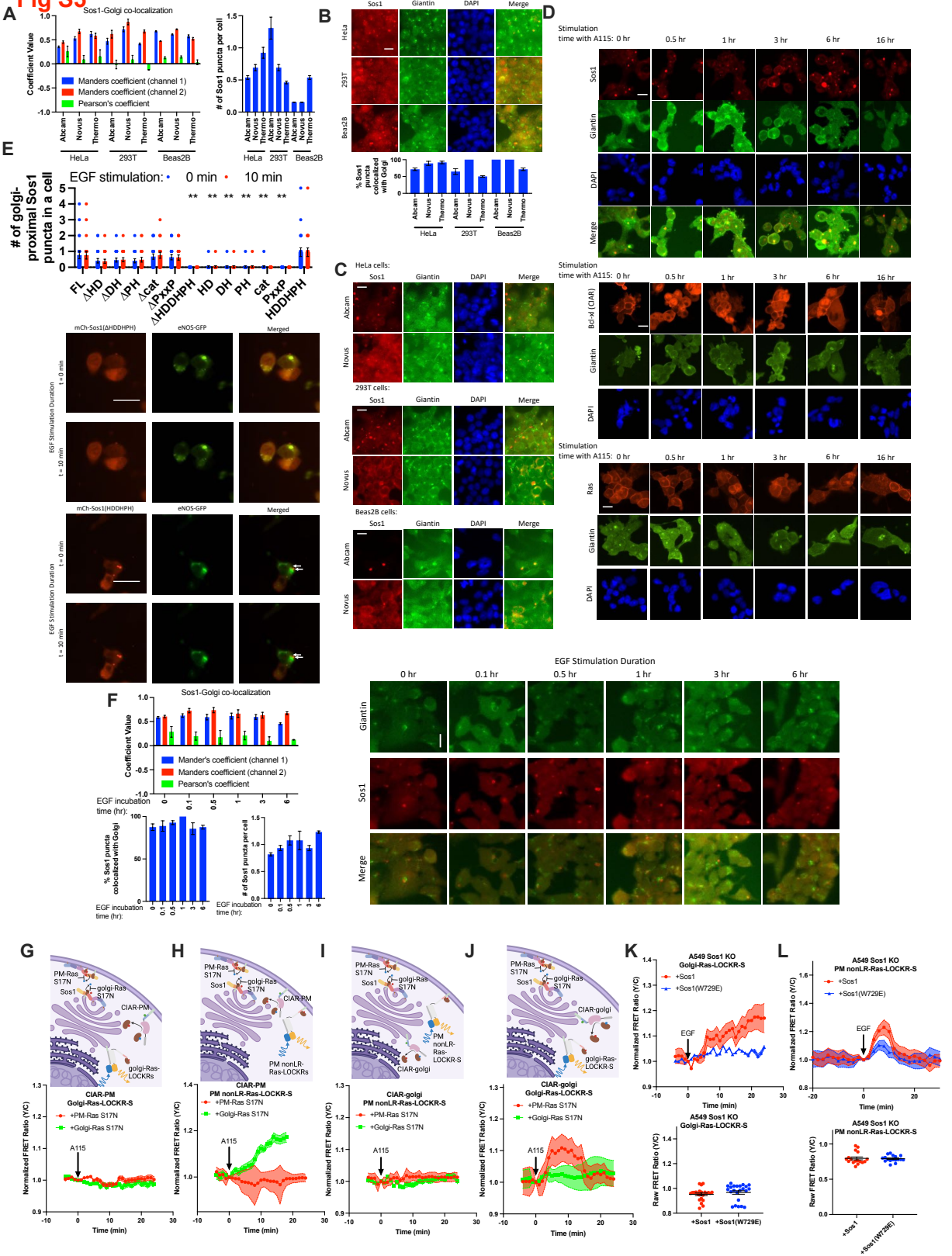
A
Sos1-Golgi co-localization
Coefficient Value
Manders coefficient (channel 1)
Manders coefficient (channel 2)
Pearson's coefficient
# of Sos1 puncta per cell
Abcam
Novus
Thermo
HeLa
293T
Beas2B
B
Sos1
Giantin
DAPI
Merge
% Sos1 puncta colocalized with Golgi
C
HeLa cells:
293T cells:
Beas2B cells:
D
Stimulation time with A115: 0 hr
0.5 hr
1 hr
3 hr
6 hr
16 hr
Bcl-xl (CIAR)
Ras
E
EGF stimulation: 0 min 10 min
# of golgi-proximal Sos1 puncta in a cell
FL
ΔHD
ΔDH
ΔPH
Δcat
ΔPxxP ΔHDDHPH
HD
DH
PH
cat
PxxP HDDHPH
mCh-Sos1(ΔHDDHPH)
eNOS-GFP
Merged
EGF Stimulation Duration
t = 0 min
t = 10 min
mCh-Sos1(HDDHPH)
F
Sos1-Golgi co-localization
EGF incubation time (hr):
% Sos1 puncta colocalized with Golgi
# of Sos1 puncta per cell
EGF Stimulation Duration
0 hr
0.1 hr
0.5 hr
1 hr
3 hr
6 hr
G
PM-Ras S17N
Sos1
golgi-Ras S17N
CIAR-PM
golgi-Ras-LOCKRs
CIAR-PM Golgi-Ras-LOCKR-S
+PM-Ras S17N
+Golgi-Ras S17N
A115
Normalized FRET Ratio (Y/C)
Time (min)
H
PM nonLR-Ras-LOCKRs
CIAR-PM PM nonLR-Ras-LOCKR-S
I
CIAR-golgi
PM nonLR-Ras-LOCKR-S
CIAR-golgi PM nonLR-Ras-LOCKR-S
J
golgi-Ras-LOCKR-S
CIAR-golgi Golgi-Ras-LOCKR-S
K
A549 Sos1 KO
Golgi-Ras-LOCKR-S
+Sos1
+Sos1(W729E)
EGF
Raw FRET Ratio (Y/C)
L
PM nonLR-Ras-LOCKR-S

Fig S6

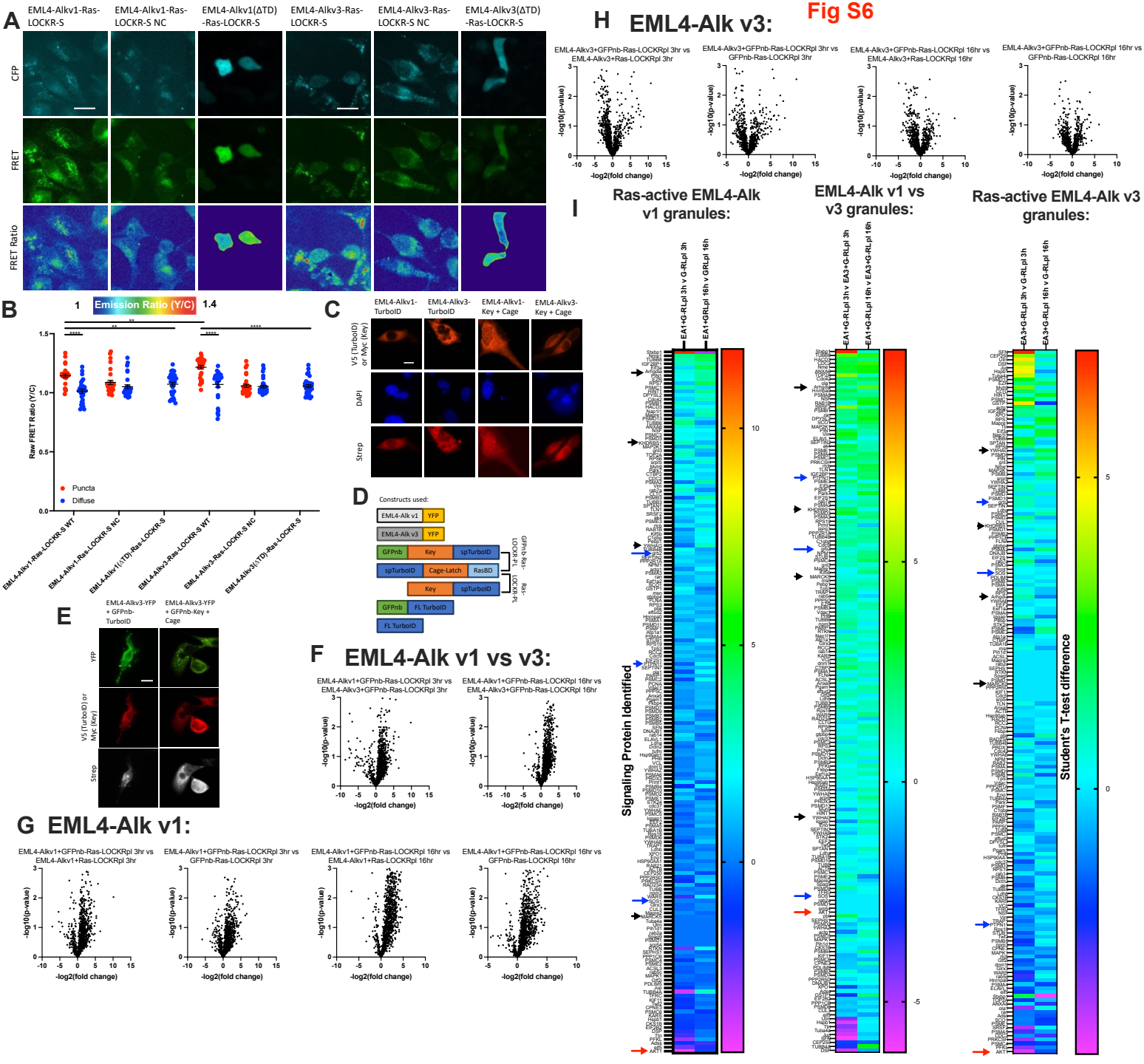
A
EML4-Alkv1-Ras-LOCKR-S
EML4-Alkv1-Ras-LOCKR-S NC
EML4-Alkv1(ΔTD)-Ras-LOCKR-S
EML4-Alkv3-Ras-LOCKR-S
EML4-Alkv3-Ras-LOCKR-S NC
EML4-Alkv3(ΔTD)-Ras-LOCKR-S
CFP
FRET
FRET Ratio
B
Emission Ratio (Y/C)
Raw FRET Ratio (Y/C)
Puncta
Diffuse
EML4-Alkv1-Ras-LOCKR-S WT
EML4-Alkv1-Ras-LOCKR-S NC
EML4-Alkv1(ΔTD)-Ras-LOCKR-S
EML4-Alkv3-Ras-LOCKR-S WT
EML4-Alkv3-Ras-LOCKR-S NC
EML4-Alkv3(ΔTD)-Ras-LOCKR-S
C
EML4-Alkv1-TurboID
EML4-Alkv3-TurboID
EML4-Alkv1-Key + Cage
EML4-Alkv3-Key + Cage
V5 (TurboID) or Myc (Key)
DAPI
Strep
D
Constructs used:
EML4-Alk v1
EML4-Alk v3
YFP
GFPnb
Key
spTurboID
Cage-Latch
RasBD
FL TurboID
GFPnb-Ras-LOCKR-PL
Ras-LOCKR-PL
E
EML4-Alkv3-YFP + GFPnb-TurboID
EML4-Alkv3-YFP + GFPnb-Key + Cage
YFP
V5 (TurboID) or Myc (Key)
Strep
F
EML4-Alk v1 vs v3:
EML4-Alkv1+GFPnb-Ras-LOCKRpl 3hr vs EML4-Alkv3+GFPnb-Ras-LOCKRpl 3hr
EML4-Alkv1+GFPnb-Ras-LOCKRpl 16hr vs EML4-Alkv3+GFPnb-Ras-LOCKRpl 16hr
-log10(p-value)
-log2(fold change)
G
EML4-Alk v1:
EML4-Alkv1+GFPnb-Ras-LOCKRpl 3hr vs EML4-Alkv1+Ras-LOCKRpl 3hr
EML4-Alkv1+GFPnb-Ras-LOCKRpl 3hr vs GFPnb-Ras-LOCKRpl 3hr
EML4-Alkv1+GFPnb-Ras-LOCKRpl 16hr vs EML4-Alkv1+Ras-LOCKRpl 16hr
EML4-Alkv1+GFPnb-Ras-LOCKRpl 16hr vs GFPnb-Ras-LOCKRpl 16hr
H
EML4-Alk v3:
EML4-Alkv3+GFPnb-Ras-LOCKRpl 3hr vs EML4-Alkv3+Ras-LOCKRpl 3hr
EML4-Alkv3+GFPnb-Ras-LOCKRpl 3hr vs GFPnb-Ras-LOCKRpl 3hr
EML4-Alkv3+GFPnb-Ras-LOCKRpl 16hr vs EML4-Alkv3+Ras-LOCKRpl 16hr
EML4-Alkv3+GFPnb-Ras-LOCKRpl 16hr vs GFPnb-Ras-LOCKRpl 16hr
-log10(p-value)
-log2(fold change)
I
Ras-active EML4-Alk v1 granules:
EML4-Alk v1 vs v3 granules:
Ras-active EML4-Alk v3 granules:
EA1+G-RLpl 3h v G-RLpl 3h
EA1+G-RLpl 16h v G-RLpl 16h
EA1+G-RLpl 3h v EA3+G-RLpl 3h
EA1+G-RLpl 16h v EA3+G-RLpl 16h
EA3+G-RLpl 3h v G-RLpl 3h
EA3+G-RLpl 16h v G-RLpl 16h
Signaling Protein Identified
Student's T-test difference

Fig S7

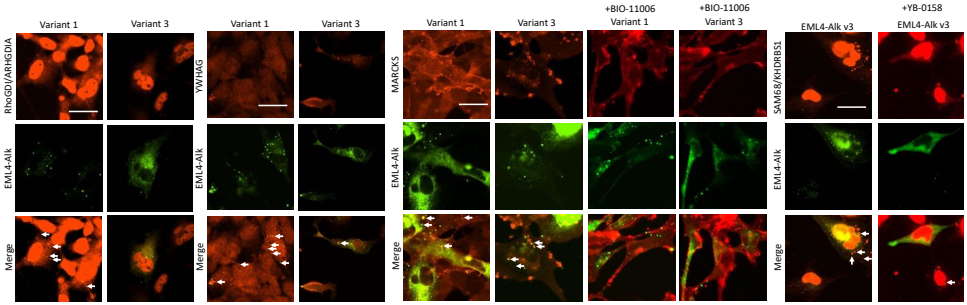

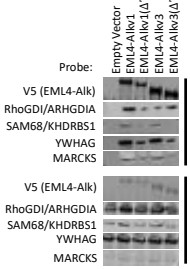

C

Experiment	Interpretation	KHDRBS1/SAM68 v1	KHDRBS1/SAM68 v3	MARCKS v1	MARCKS v3
EA+G-RLpl 3h vs G-RL-PL 3h	inside vs outside	2.99	0.39	-0.01	0.00
EA+GRLpl 16h v GRL-PL 16h	inside vs outside	1.06	0.35	0.08	0.00
EA+G-TID 1h v G-TID 1h	inside vs outside	1.15	1.14	1.48	0.27
EA+G-RLpl 3h v EA+RL-PL 3h	inside vs outside	2.98	1.31	-0.37	0.00
EA+G-RLpl 16h v EA+RL-PL 16h	inside vs outside	3.17	0.01	0.37	0.00
EA+G-TID 1h v EA+TID 1h	inside vs outside	4.91	2.42	1.42	0.71
EA+GRL-PL 3h v EA+G-TID 1h	Ras activity dependent vs independent	0.56	-2.02	-1.73	-1.12
EA+G-RL-PL 16h v EA+G-TID 1h	Ras activity dependent vs independent	-0.32	-1.02	-1.25	-0.61

Student's t-test difference

D

Inhibitor	Symbol	Target
Crizotinib	Cz	Alk
Ceritinib	Ce	Alk
Gö6983	G	PKC
BIO-11006	B	MARCKS
YB-0158	Y	SAM68

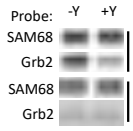

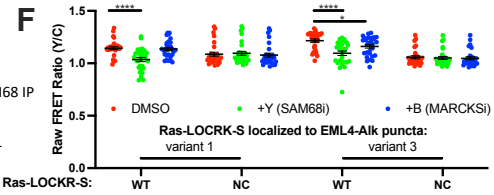

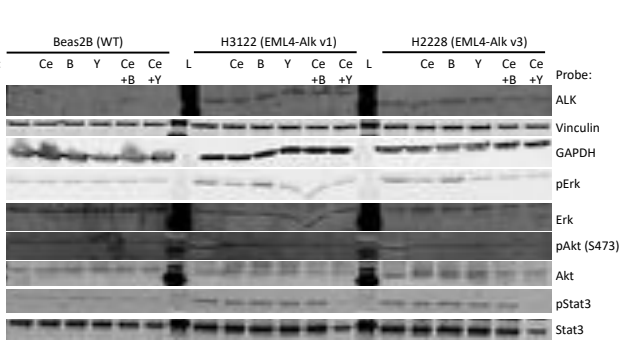

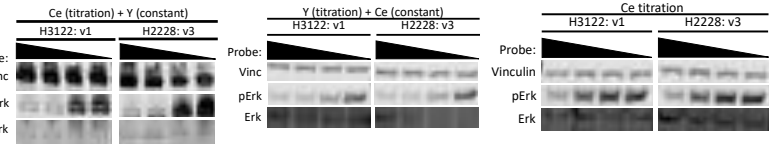

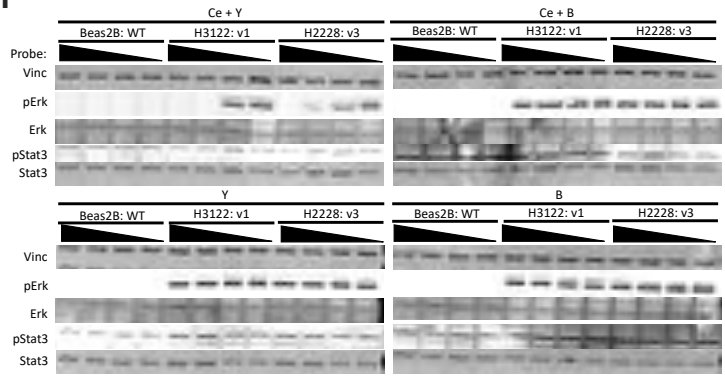

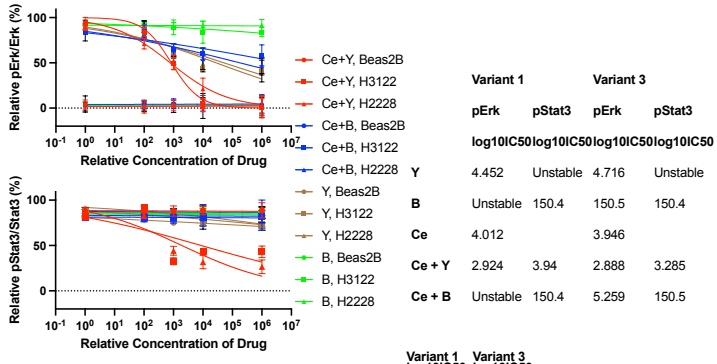

	Variant 1 pErk log10IC50	Variant 1 pStat3 log10IC50	Variant 3 pErk log10IC50	Variant 3 pStat3 log10IC50
Y	4.452	Unstable	4.716	Unstable
B	Unstable	150.4	150.5	150.4
Ce	4.012		3.946	
Ce + Y	2.924	3.94	2.888	3.285
Ce + B	Unstable	150.4	5.259	150.5

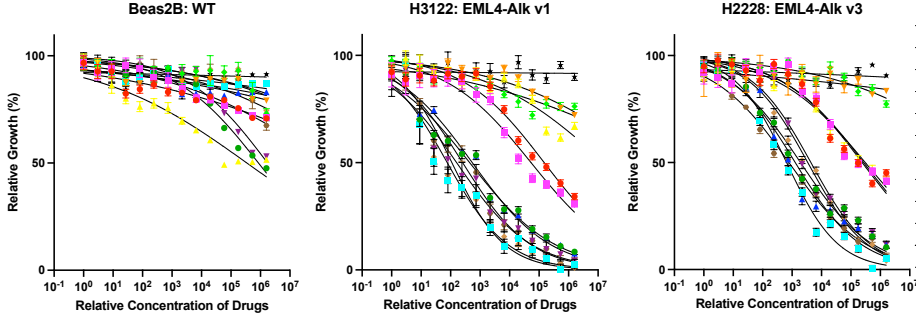

	Variant 1 log10IC50	Variant 3 log10IC50
Cz (Alki)	5.176	5.383
Ce (Alki)	4.729	5.433
G (PKCi)	Unstable	5.488
B (MARCKSi)	Unstable	Unstable
Y (SAM68i)	Unstable	Unstable
Cz+G	2.647	3.127
Cz+B	1.887	2.752
Cz+Y	2.736	2.926
Ce+G	2.205	3.484
Ce+B	2.044	3.483
Ce+Y	2.408	2.85
DMSO	151.8	7.108

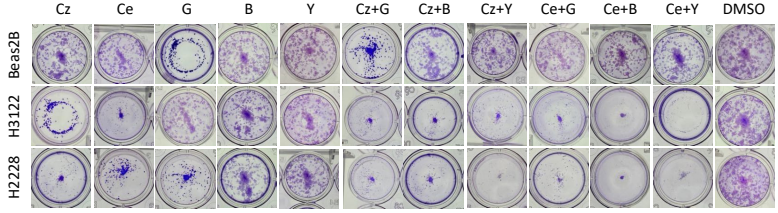

Fig S8

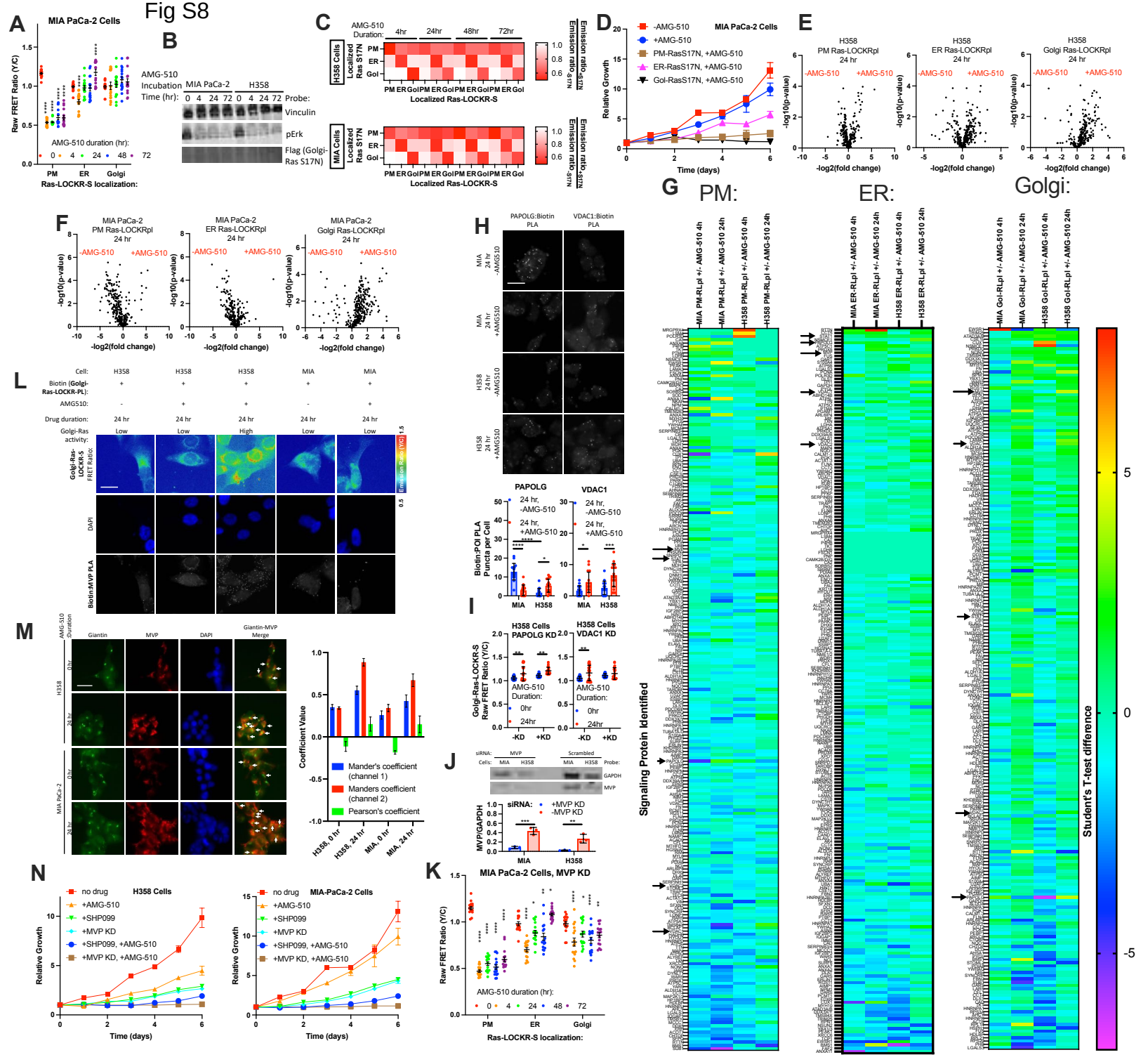
A
MIA PaCa-2 Cells
Raw FRET Ratio (Y/C)
AMG-510 duration (hr):
0 4 24 48 72
PM ER Golgi
Ras-LOCKR-S localization:
B
AMG-510 Incubation Time (hr):
MIA PaCa-2
H358
0 4 24 72 0 4 24 72
Probe:
Vinculin
pErk
Flag (Golgi-Ras S17N)
C
AMG-510 Duration:
4hr 24hr 48hr 72hr
H358 Cells
MIA Cells
Localized Ras S17N
PM ER Golgi
Localized Ras-LOCKR-S
Emission ratio G-S17N/Y-S17N
D
MIA PaCa-2 Cells
-AMG-510
+AMG-510
PM-RasS17N, +AMG-510
ER-RasS17N, +AMG-510
Gol-RasS17N, +AMG-510
Relative Growth
Time (days)
E
H358
PM Ras-LOCKRpl 24 hr
ER Ras-LOCKRpl 24 hr
Golgi Ras-LOCKRpl 24 hr
-AMG-510
+AMG-510
-log10(p-value)
-log2(fold change)
F
MIA PaCa-2
PM Ras-LOCKRpl 24 hr
ER Ras-LOCKRpl 24 hr
Golgi Ras-LOCKRpl 24 hr
-AMG-510
+AMG-510
-log10(p-value)
-log2(fold change)
G
PM:
ER:
Golgi:
MIA PM-RLpl +/- AMG-510 4h
MIA PM-RLpl +/- AMG-510 24h
H358 PM-RLpl +/- AMG-510 4h
H358 PM-RLpl +/- AMG-510 24h
MIA ER-RLpl +/- AMG-510 4h
MIA ER-RLpl +/- AMG-510 24h
H358 ER-RLpl +/- AMG-510 4h
H358 ER-RLpl +/- AMG-510 24h
MIA Golgi-RLpl +/- AMG-510 4h
MIA Golgi-RLpl +/- AMG-510 24h
H358 Golgi-RLpl +/- AMG-510 4h
H358 Golgi-RLpl +/- AMG-510 24h
Signaling Protein Identified
Student's T-test difference
5
0
-5
H
PAPOLG:Biotin PLA
VDAC1:Biotin PLA
MIA 24 hr -AMG510
MIA 24 hr +AMG510
H358 24 hr -AMG510
H358 24 hr +AMG510
PAPOLG
VDAC1
24 hr, -AMG-510
24 hr, +AMG-510
Biotin:POI PLA Puncta per Cell
MIA
H358
I
H358 Cells
PAPOLG KD
VDAC1 KD
Golgi-Ras-LOCKR-S Raw FRET Ratio (Y/C)
AMG-510 Duration:
0hr
24hr
-KD
+KD
J
siRNA:
MVP
Scrambled
Cells:
MIA
H358
Probe:
GAPDH
MVP
MVP/GAPDH
+MVP KD
-MVP KD
K
MIA PaCa-2 Cells, MVP KD
Raw FRET Ratio (Y/C)
AMG-510 duration (hr):
0 4 24 48 72
PM ER Golgi
Ras-LOCKR-S localization:
L
Cell:
Biotin (Golgi-Ras-LOCKR-PL):
AMG510:
Drug duration:
Golgi-Ras activity:
Low Low High Low Low
Golgi-Ras-LOCKR-S FRET Ratio:
Emission Ratio (YC)
DAPI
Biotin:MVP PLA
M
Giantin
MVP
DAPI
Giantin-MVP Merge
AMG-510 Duration
H358
MIA PaCa-2
0hr
24hr
Coefficient Value
Mander's coefficient (channel 1)
Manders coefficient (channel 2)
Pearson's coefficient
H358, 0 hr
H358, 24 hr
MIA, 0 hr
MIA, 24 hr
N
H358 Cells
MIA-PaCa-2 Cells
no drug
+AMG-510
+SHP099
+MVP KD
+SHP099, +AMG-510
+MVP KD, +AMG-510
Relative Growth
Time (days)

Fig 3

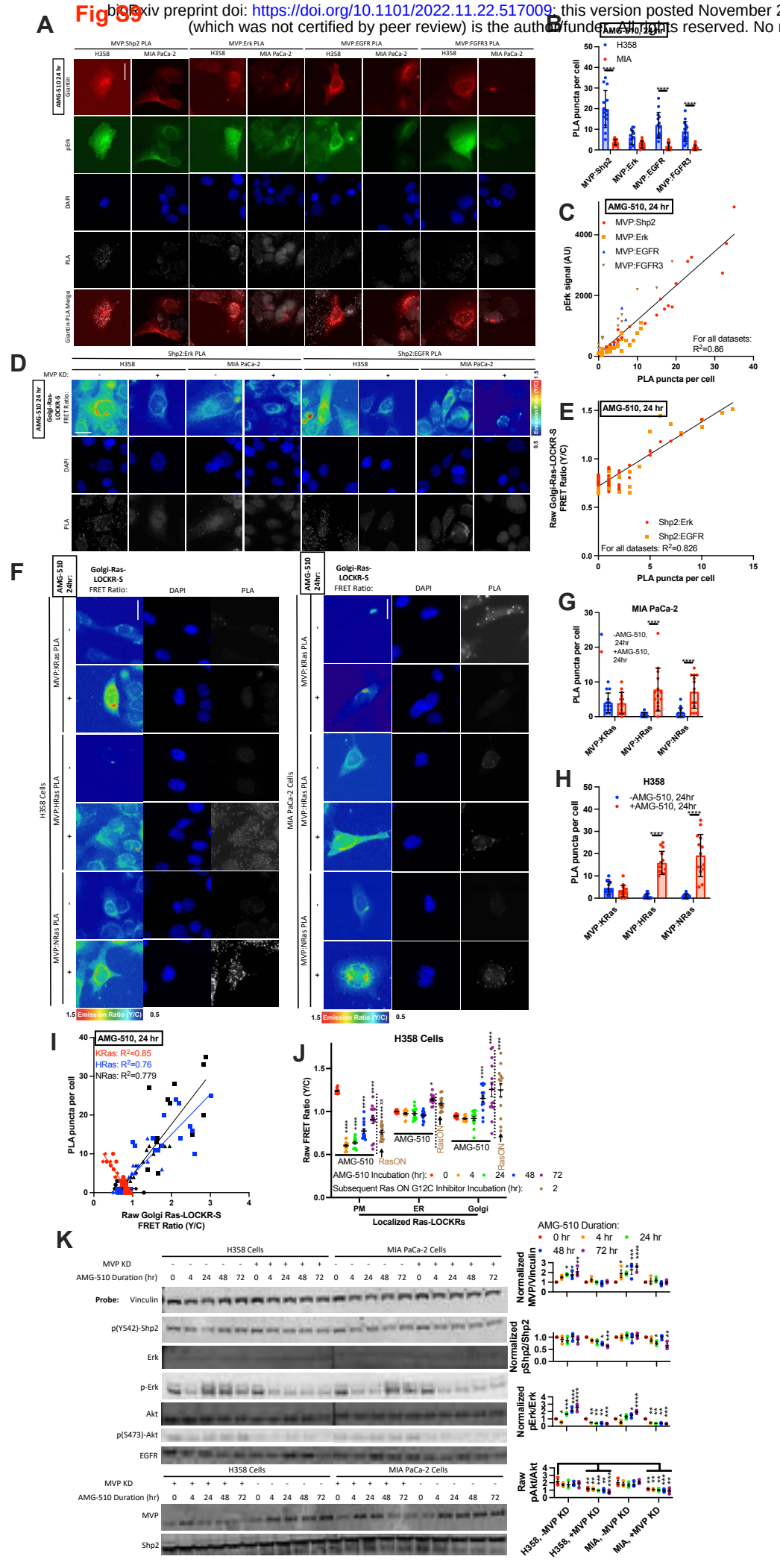

Fig S10

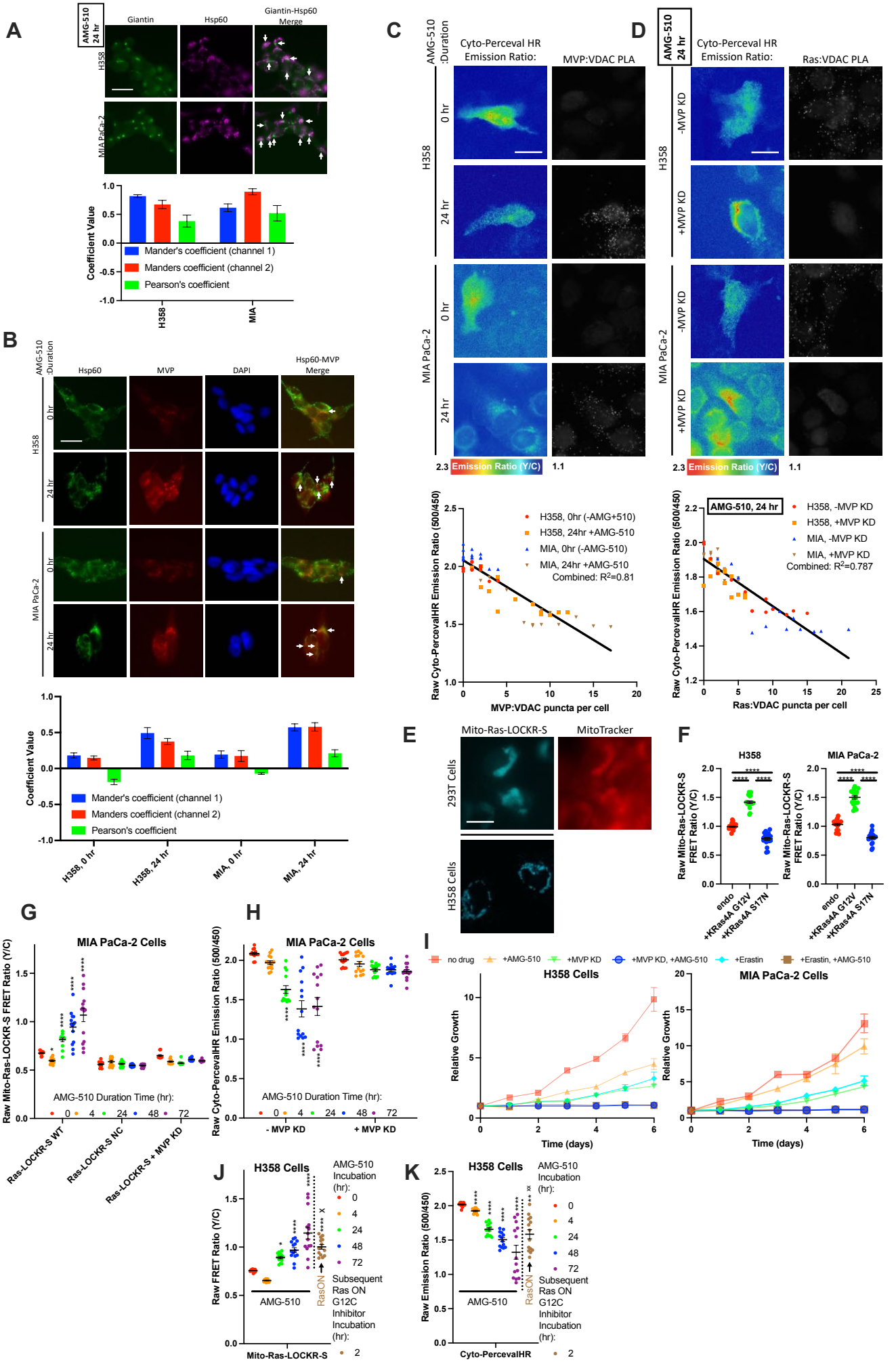
A
AMG-510 24 hr
Giantin
Hsp60
Giantin-Hsp60 Merge
H358
MIA PaCa-2
Coefficient Value
Mander's coefficient (channel 1)
Manders coefficient (channel 2)
Pearson's coefficient
H358
MIA
B
AMG-510 :Duration
Hsp60
MVP
DAPI
Hsp60-MVP Merge
H358
MIA PaCa-2
0 hr
24 hr
Coefficient Value
Mander's coefficient (channel 1)
Manders coefficient (channel 2)
Pearson's coefficient
H358, 0 hr
H358, 24 hr
MIA, 0 hr
MIA, 24 hr
C
AMG-510 :Duration
Cyto-Perceval HR Emission Ratio:
MVP:VDAC PLA
H358
MIA PaCa-2
0 hr
24 hr
2.3
Emission Ratio (Y/C)
1.1
D
AMG-510 24 hr
Cyto-Perceval HR Emission Ratio:
Ras:VDAC PLA
H358
MIA PaCa-2
-MVP KD
+MVP KD
2.3
Emission Ratio (Y/C)
1.1
Raw Cyto-PercevalHR Emission Ratio (500/450)
MVP:VDAC puncta per cell
H358, 0hr (-AMG+510)
H358, 24hr +AMG-510
MIA, 0hr (-AMG-510)
MIA, 24hr +AMG-510
Combined: R²=0.81
Raw Cyto-PercevalHR Emission Ratio (500/450)
Ras:VDAC puncta per cell
AMG-510, 24 hr
H358, -MVP KD
H358, +MVP KD
MIA, -MVP KD
MIA, +MVP KD
Combined: R²=0.787
E
Mito-Ras-LOCKR-S
MitoTracker
293T Cells
H358 Cells
F
H358
MIA PaCa-2
Raw Mito-Ras-LOCKR-S FRET Ratio (Y/C)
endo
+KRas4A G12V
+KRas4A S17N
G
MIA PaCa-2 Cells
Raw Mito-Ras-LOCKR-S FRET Ratio (Y/C)
AMG-510 Duration Time (hr):
0
4
24
48
72
Ras-LOCKR-S WT
Ras-LOCKR-S NC
Ras-LOCKR-S + MVP KD
H
MIA PaCa-2 Cells
Raw Cyto-PercevalHR Emission Ratio (500/450)
AMG-510 Duration Time (hr):
- MVP KD
+ MVP KD
I
no drug
+AMG-510
+MVP KD
+MVP KD, +AMG-510
+Erastin
+Erastin, +AMG-510
H358 Cells
MIA PaCa-2 Cells
Relative Growth
Time (days)
J
H358 Cells
Raw FRET Ratio (Y/C)
AMG-510
RasON
AMG-510 Incubation (hr):
Subsequent Ras ON G12C Inhibitor Incubation (hr):
Mito-Ras-LOCKR-S
K
H358 Cells
Raw Emission Ratio (500/450)
AMG-510
RasON
AMG-510 Incubation (hr):
Subsequent Ras ON G12C Inhibitor Incubation (hr):
Cyto-PercevalHR